A Study of Extreme Ultraviolet Capillary Discharge Lasers and the Ablation of Solid Targets

Sarah Arabella Wilson

Doctor of Philosophy

University of York

Physics

September 2018

Abstract

his thesis discusses the use of capillary discharge laser output in the Extreme Ultraviolet (EUV) as a means of ablating solid targets. The EUV capillary discharge laser uses a neon-like argon plasma as the lasing medium contained within a ceramic capillary. The laser produces a pulse of duration 1.2ns, at a wavelength of 46.9nm, with a repetition rate of up to 10Hz. A review of EUV production and the optical properties of EUV radiation at 46.9nm is given. From this a review of potential focusing methods for the laser is presented. An on-axis spherical mirror has been experimentally tested to give focal spot diameters of 3μm. The characterisation and optimisation of the capillary discharge laser is discussed. Optical spectra have been shown to enable a new method of measuring the average electron temperature of the plasma medium of the laser by modelling it as a black body. Plasma temperatures of approximately 3eV are measured. The capillary discharge laser has been used to ablate solid targets of aluminium, gold, copper and Poly-methyl methacrylate (PMMA). The ablation craters for each target material were measured using an atomic force microscope. Single shot depths of ablation of 1.3μm (Al), 0.9μm (Au), 0.6μm (Cu) and 0.3μm (PMMA) using fluences of approximately 200J/cm^2 were obtained. Ablation depths for aluminium are well modelled assuming ablation only occurs over the EUV attenuation length in the solid. For targets with short attenuation lengths another model based on a propagating ablation wave fits the experimental ablation depths. Both models allow an estimate of the ablated plasma temperature which is typically in the range of 2eV to 50eV, meaning the ablating plasma can be classed as a warm dense plasma.

Contents

List of Tables

List of Figures

Acknowledgments

I would like to thank everyone at the York Plasma Institute for the support throughout my PhD. Special thanks to my supervisor, Professor Greg Tallents for the constant guidance and advice. I am very grateful to Richard and Kari for all the help in the lab and to Andy for help with setting up the laser. Massive thank you to James and Edurado for helping with the experiments and measurements. Good luck to both of you in your PhD's, I hope the laser behaves itself. To everyone in the office, thank you for entertaining me and for eating all my experimental baking.

To everyone at Colorado State University, in particular to Professors Jorge Rocca and Carmen Menoni, for allowing me to visit multiple times, for teaching me everything there is to know about the capillary discharge laser and for all the early morning skype calls. Special thanks to Chad, Herman, Ramon and Jeremy for your help with building the laser, carrying out the experiments and for making my trips to Colorado so enjoyable.

Thanks to everyone at University of York Archery Club, it's been wonderful to de-stress and shoot with you. It's been a pleasure coaching you all and I hope you keep on winning! Special thanks to Alex, Jared, Flo and David, between all the archery, board games and pub trips, it has been wonderful de-stressing with you.

Thanks to the extended Wilson and Shaw families for being a wonderful support network and for all the skiing and sailing holidays, which are always great fun. Special thanks to Richard and Gill for taking me in during the great flood of 2017 and always having a glass of wine ready for me.

Thank you to David for putting up with me over the past four years. I don't think I would have made it this far without your encouragement and belief in my ability in both my PhD and archery. Thank you for always being able to make me laugh and being a constant source of joy in my life.

Finally, thank you to mum and dad. You have helped fuel my curiosity for physics and encouraged me to keep going with it, be that by putting my a-level physics teacher in his place or helping me move back to Queens for my last minute decisions to change my degree.

You have made me believe that I can do anything that I put my mind to. Thank you for always being just a phone call away, for constantly supporting me and giving me the encouragement to keep going.

Declaration

This thesis has not previously been accepted for any degree and is not being concurrently submitted in candidature for any degree other than Doctor of Philosophy of the University of York. This thesis is the result of my own investigations, except where otherwise stated. All other sources are acknowledged by explicit references.

Chapter 1

Introduction

The Extreme Ultraviolet (EUV) spectral range extends from approximately 25eV to 250eV in photon energy or wavelengths of approximately 5nm to 50nm [1]. As direct photo-ionisation of electrons from neutral atoms is possible with such photon energies, the absorption of EUV wavelengths in all materials is high. Experiments in the EUV need to be carried out in vacuum and transmission optics cannot be used. Associated with the high level of absorption of EUV light, non-grazing incidence reflections at surface do not occur with high reflection coefficients. For example: gold at 46.9nm reflects normally with a 10% reflection coefficient if the surface roughness is low. Low transmission through materials and modest reflectivity makes the EUV a difficult regime to investigate experimentally [2].

However, EUV lasers enable a new regime of laser-plasma experiments. Optical lasers of wavelength 0.25-10μm have critical densities less than the electron density produced in solids, so the laser absorption is collective in the plasma produced for solid target irradiation. EUV lasers interact directly with solid targets via photo-ionisation (and inverse bremsstrahulung, once free-electrons have been created). We show in this thesis that it is possible to create solid density plasmas which have temperatures of only a few electron volts. Such plasmas are often referred to as warm dense matter (see Section 2.2).

The creation of EUV lasers has been a difficult physics and engineering problem because of pumping inefficiencies inherent in creating short wavelength lasers. Inefficient pumping means that the power supplied to produce modest laser output needs to be large. This thesis discusses an electrical discharge pumping method based on creating a Z-pinch plasma enclosed by a solid capillary.

The short wavelength of an EUV laser enables, in principle, the focusing of the laser to dimensions close to the wavelength. A narrow focus means that a modest laser power can produce a high irradiation well above the threshold required to ablate solid material. The narrow focus also enables small-scale features to be ablated in a solid and opens up the prospect of creating micron scale features on a solid using a EUV laser.

This thesis discusses the commissioning of a capillary discharge EUV laser and its use to ablate solid targets. Various options for focusing the laser are investigated with the aim to implement in the future a procedure enabling diffraction limited focal spots for the ablation of solids. Two models are shown to describe the ablation of solid targets with the EUV laser. A model usually used to determine the ablation depth of femtosecond optical laser pulses is shown to describe the ablation of targets such as aluminium which have long attenuation lengths for the EUV radiation. For targets with short attenuations lengths, it is shown that a model of an ionisation wave propagating into the target as used in x-ray free electron laser ablation studies describes the EUV ablation depths.

1.1 Thesis Summary

This thesis is set out in the following manner:

Chapter 2 gives an introduction to plasma physics and production of warm dense matter from EUV radiation. This is followed by an introduction to laser physics and different methods of creating coherent and incoherent EUV radiation.

Chapter 3 summarises the optical interactions of EUV radiation. The difficulties involved in focusing radiation in the EUV wavelength range and different focusing methods are discussed.

Chapter 4 gives a review of different focusing techniques. The advantages and disadvantages of using them to achieve diffraction limited focusing with EUV radiation are discussed.

Chapter 5 provides a detailed description of EUV capillary discharge lasers and the physical processes producing the EUV radiation. There is discussion about some of the laser parameters and the diagnostics used to measure the laser output.

Chapter 6 discusses the characterisation and set-up processes of the capillary discharge laser at the University of York. Some of the problems encountered during set-up are presented with a discussion of how and why these problems occurred and how to prevent them from arising again in the future.

Chapter 7 gives the results for ablation experiments carried out using the capillary discharge laser. Results are shown for similar experiments performed using different optics and target materials and the outcomes of these experiments are discussed.

Chapter 8 summarises the thesis and gives the key conclusions from results presented.

Chapter 2

Background to Extreme Ultraviolet Radiation

This chapter discusses the fundamentals of EUV and plasma physics in order to understand the production of the plasma required to create an EUV capillary discharge laser and to understand some of the physics of warm dense matter. Methods of creating EUV coherent and incoherent radiation are briefly reviewed.

2.1 Plasmas

Plasmas are commonly considered to be the fourth state of matter. The matter in a plasma consists of ions and electrons which are no longer in their lowest possible energy state. Molecular bonds are broken, electrons can be excited into higher energy states and atoms can be ionised. Ions and free electrons can be accelerated by electric and magnetic fields so the plasma reacts to light in different ways to solids, liquids and gases [3].

A plasma is formally defined by Chen [4] as,

"A quasineutral gas of charged and neutral particles which exhibits collective behaviour."

Collective behaviour occurs when the movement of one particle effects the movement of others. In a plasma this occurs due to collisions of particles, and due to electromagnetic forces. Collective behaviour forms groups of positively or negatively charged particles together in the plasma.

To define quasineutrality the Debye shielding of a plasma must first be understthood. Debye shielding is the ability of the plasma to shield electric potentials. The Debye length (λ_D) is the measure of shielding distance or the thickness of the sheath and is given by,

$$\lambda_D \equiv \left(\frac{\epsilon_0 k_B T_e}{n_e e^2}\right)^{1/2} \tag{2.1}$$

where ϵ_0 is the permittivity of free space, k_B is the Boltzmann constant, T_e is the electron temperature, n_e is the plasma density and e is the electronic charge.

Quasineutrality occurs when the dimension of a system, L, is larger than the Debye length. Local charge within the system is then shielded on a smaller scale than the entire system. If external charges are induced in a system of size L, they are shielded over distance λ_D. On a macroscopic scale the system will appear to be neutral, but on a microscopic scale there are areas of concentrated electrostatic charge.

For the concepts of collective behaviour and quasineutrality to be valid there must be enough particles in the plasma to be statistically significant. The number of electrons in the Debye sphere is given by

$$N_D = n_e \frac{4}{3}\pi\lambda_D^3 = 1.38 \times 10^6 T^{3/2}/n_e^{1/2}, \tag{2.2}$$

for collective behaviour to be valid the plasma parameter N_D must satisfy the inequality,

$$N_D >>> 1. \tag{2.3}$$

To be formally defined as a plasma the collisions of the particles with neutrals must be considered. If the charged particles are colliding with neutral particles too frequently the motion of the particles is controlled by hydrodynamic forces rather than by electromagnetic forces. If the frequency of a typical plasma collision is ω and the time between collision is τ, the electromagnetic forces dominate if, $\omega\tau > 1$ [4].

If the electrons in a plasma are displaced, an electric field will develop in the opposite direction, opposing the displacement of the electrons in order to return the electrons to their equilibrium position. Due to the effects of inertia the electrons overshoot their original position and the process repeats in the opposite direction at a resonant frequency. This is the plasma frequency, ω_p,

$$\omega_p = \left(\frac{n_e e^2}{\epsilon_0 m}\right)^{1/2}. \tag{2.4}$$

If there are no damping effects in the plasma the oscillation will continue indefinitely. An oscillating electron is so fast that the much heavier ions do not have time to respond and they can be considered fixed. The plasma frequency restricts how quickly the plasma can respond to external electromagnetic fields [5].

2.2 Warm Dense Matter

Warm Dense Matter (WDM) may be described as an intermediate state of matter as it presents qualities of basic plasma physics and condensed matter physics with temperatures comparable to the Fermi energy and densities high enough that the Coulomb and thermal energies are comparable. In condensed matter the Coulomb potential between atoms is much greater than the thermal energy, while in classical plasmas, thermal energies are much greater than the interaction energy associated with Coulomb forces between atoms [6, 7]. Typical conditions for WDM are densities between 0.1g/cm^3 to 10g/cm^3 along with relatively low temperatures, which range from 0.1eV to 100eV (Figure 2.1).

The defining features of WDM is the strong ion coupling, due to their Coulomb interaction, where the Coulomb coupling parameter, Γ, is given by,

$$\Gamma = \frac{Z^{*2} e^2}{r_i k_B T_i} \frac{1}{4\pi\epsilon_0}. \tag{2.5}$$

Here Z^* is the average ionisation, e is the elementary charge, k_B is the Boltzmann constant and T_i is the ion temperature. This defines the coupling parameter as the ratio of the average potential energy of two ions that are an average distance r_i from each other and an average kinetic energy which is proportional to T_i. If $\Gamma << 1$ then the Coulomb forces can be neglected and the plasma treated as an ideal classical plasma. If $\Gamma >> 1$, then the system starts to be governed by the rules of condensed matter and can be referenced to as a

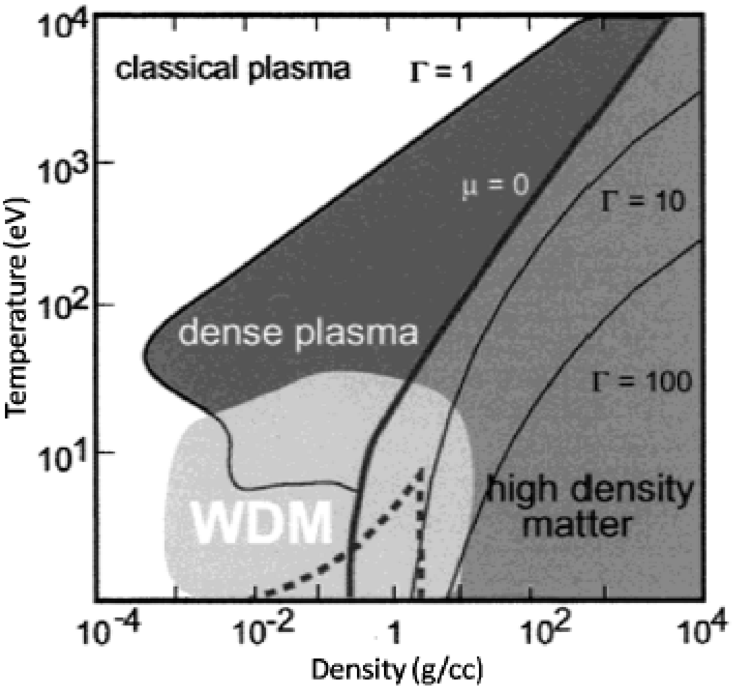

Figure 2.1: Phase-diagram for aluminium showing the temperature and density plane and the regions of warm dense matter, high density matter and classical plasma. The value of the ion-ion coupling parameter (Γ) and the parameter where the chemical potential $\mu = 0$ are also shown [8].

high density plasma. In WDM the Coulomb coupling parameter is near unity (Figure 2.1) [9].

2.3 Electron Degeneracy

A fully degenerate system is one where all possible lower energy states are populated according to the quantum mechanical Pauli exclusion principle. The Pauli exclusion principle states that two identical fermions cannot occupy the same quantum state. With increasing density electrons are forced into higher quantum states.

WDM is a partially degenerate state where there are fewer lower energy states available for particles to occupy. The electrons in a plasma cannot lose energy to ions as easily and thus degeneracy affects the inter ionic potential, hence the structure of the plasma.

When degeneracy effects become important the expressions for various plasmas parameters must be modified. For a system of charged particles obeying classical statistics, the kinetic energy per particle may be estimated from the temperature and Boltzmann's constant. For a degenerate electron system with electron number density n_e, the Fermi energy is used instead [10],

$$E_F = \frac{\hbar^2}{2m_e}(3\pi^2 n_e)^{2/3} \tag{2.6}$$

where m_e is the mass of an electron and $\hbar = \frac{h}{2\pi}$ where h is Planks constant.

The degree of degeneracy can be quantified through the ratio of the thermal De Broglie wavelength of electrons to the average inter-electron spacing (a_{ee}). The thermal De Broglie wavelength is given by [11],

$$\lambda_{DB} = \Big(\frac{\hbar}{2\pi n_e k_B T}\Big)^{1/2}. \tag{2.7}$$

If the ratio of $\frac{a_{ee}}{\lambda_{DB}} < 1$ the electrons are considered to be degenerate. If this ratio is equal to one, the system is considered partially degenerate as is the case for WDM.

Another plasma parameter which is modified for degenerate systems is the Debye length. In classical plasmas the electrons are Maxwell-Boltzmann distributed, where the distance over which significant charge separation can occur is given by the Debye length (Equation (2.1)). However, in a degenerate system the electrons are distributed by Fermi-Dirac statistics and so the charge separation is given by the Thomas-Fermi screening length [12],

$$\lambda_{TF} = \big(\frac{\pi}{12}\big)^{1/3} Z^{*-1/6} \big(\frac{a_{ee}}{a_b}\big)^{-1/2} \tag{2.8}$$

where a_b is the classical Bohr radius and a_{ii} is the average inter-particle separation and Z^* is the average ionisation.

A partially degenerate system such as a warm dense plasma, will exhibit the properties of both a classical and degenerate system. For example the effective temperature (T_{eff}) can be calculated using the Fermi temperature and the particle temperature, where [13]

$$T_{eff} = \sqrt{T_q^2 + T_e^2}, \tag{2.9}$$

or

$$T_q = \frac{T_F}{(1.3251 - 0.1779\sqrt{a_{ii}/a_b})}. \tag{2.10}$$

Such plasmas exist at solar interiors with temperatures ranging from 1eV to 100eV and electron densities of 10^{18}e/cm^2 to 10^{22}e/cm^2. Other examples include pinch plasmas with temperatures ranging from 10eV to 100eV and Electron densities of 10^{16}e/cm^2 to 10^{20}e/cm^2 and discharge plasmas with temperatures ranging from 1eV to 10eV and Electron densities of 10^{10}e/cm^2 to 10^{14}e/cm^2.

2.4 Short Wavelength Coherent Sources

2.4.1 Lasers

The word laser is an acronym for Light Amplification by Stimulated Emission of Radiation. Laser systems create photons usually of a small energy range by stimulated transitions between two atomic energy states. Stimulated emission occurs when an incident photon causes an excited electron to relax into a lower energy state emitting a photon corresponding to the transition energy in addition to the stimulating photon. In order to increase the photon flux there must be more electrons in the upper energy state than the lower energy state, otherwise absorption of photons will dominate stimulated emission. The condition where this occurs is called population inversion. A population inversion allows stimulated emission to become the dominant process so that lasing can occur [14].

Most lasers produce radiation ranging from infra-red to ultraviolet wavelengths. This thesis concentrates on a short wavelength laser in the EUV regime. The pumping power necessary to produce a short wavelength laser scales as typically $1/\lambda^5$ which makes it more difficult to achieve lasing at short wavelengths ([15] and see section 5.1.1 where this scaling is explored further).

2.4.2 High Harmonics

A popular method of producing EUV radiation is to generate high harmonics using intense femtosecond lasers focused in noble gasses [16]. High harmonics result from a non-linear interaction between the electric field of the incident laser pulse and the individual atoms. The intensity of the laser light is chosen such that its electric field amplitude is comparable to the electric field in the atoms. Electrons are removed from the atoms potential by the laser electric field and accelerated away from the atom. When the lasers electric field changes direction due to its oscillation in time, the electrons accelerate back towards the atom. Due to the non-linear acceleration, harmonics at multiple frequencies are produced. The incident laser can drive the non-linear generation of harmonics in a large number of atoms which are all phase coherent with the incident laser. Resultant harmonics add in phase in the direction of the driving pulse, leading to intense high harmonics in a narrow radiation cone [1]. Gases are used as the lasing medium as they are a highly non-linear material and can be exposed to higher intensities than solids or liquids without being damaged. Noble gasses are favoured for producing high harmonics as having closed shells means they do not have a steady state dipole moment but a dipole can be induced when an electric field is applied. The harmonic emissions and the number of harmonics depends on the material used, for example, xenon has a larger polarisability and therefore has a strong harmonic emissions, but helium is more resistant to depletion through ionisation so it can produce higher harmonics [17].

In order to achieve high harmonic generation, ultra short laser pulses, usually in the femtosecond region are used. The release and return of the electron are well localized in time compared to the laser period, so that the time profile of the emitted radiation corresponds to a series of short pulses separated by half a laser period. The fast oscillations in the electric field produced from the interference of the re-colliding electron wavepacket with the remaining atom are produced every half cycle. A Fourier transform yields a series of attosecond pulses with harmonics separated by the energy of two fundamental photons. Since the electric dipole operator has odd parity and the electron starts and finishes in the same state, only odd harmonics are produced to conserve parity. To study ultrafast phenomena it is highly desirable to generate single, isolated attosecond pulses. This can be achieved if the emission of the high harmonics is limited to a single laser half-cycle. Such attosecond pulses are now used for various fundamental studies including real-time observation of tunnel ionization, ultrafast surface science, ultrafast molecular imaging, ultrafast material modification and direct observation and control of electron wavepackets [18].

Only a fraction of the incident laser power can be converted into higher harmonics, so using high harmonics is not the optimum process for producing the radiation desired for the experiments presented in this thesis. The power in a harmonic is restricted to typically $< 10^{-6}$ of the femtosecond laser power. With femtosecond pulses the energy per pulse in a harmonic is typically $< 1nJ$.

high harmonic generation does not fulfil our research requirements as well as being an expensive method of producing EUV radiation.

2.4.3 Synchrotron and X-ray Free Electron Laser Sources

Synchrotron radiation is the name given to the radiation which occurs when charged particles are accelerated in a curved path or orbit [19]. It can be produced by accelerating relativistic electrons in a magnetic field. This can be done on three ways, bending magnets, undulators and wigglers. Bending magnets cause a single curved trajectory resulting in a fan of radiation around the bend in the magnet. Undulators are periodic lattices of alternating magnetic dipolar fields with a relatively weak magnetic field. Undulators cause electrons to periodically experience oscillations and produce radiation with a small angular divergence and small spectral range. Wigglers are similar to undulations but with a strong magnetic field making the radiated power larger, with a larger radiation cone. The radiation spectrum from wigglers is similar to bending magnets, however there is a much larger photon flux and a shift to shorter wavelengths and hard x-rays [1, 20]. The radiation produced is proportional to the fourth power of the particle speed and is inversely proportional to the square of the radius of the path [19].

Free electron lasers (FEL) use the undulator magnetic structure to generate coherent radiation by stimulated emission. In FELs the radiation power increases exponentially as the electron beam and radiation propagate along the undulator meaning a small source can be amplified by many orders of magnitude before saturation. The FEL functions as a single-pass amplifier, generating pulses with powers of 10^{10}W and pulse durations of femtoseconds, with pulse energies of typically around 1mJ [20, 21].

Synchrotrons and free-electron lasers are large research facilities which are expensive to build and run and tend to be national or international research facilities [22] with limited time and long waiting lists for access.

2.4.4 Laboratory Laser Produced Plasmas

Plasmas can be produced using optical lasers which in turn emit EUV radiation. Lasers deposit large amounts of energy in a very short time on a target surface creating a non-equilibrium atomic energy distribution which produces a plasma. The plasma produced on the surface of the target can then produce EUV radiation. Typically two laser pulses are used to do this, the first laser is a longer pulse duration pre-pulse which sets up a plasma plume, before a second short pulse, high intensity laser deposits the bulk of the energy in the plasma.

A technique for producing EUV radiation uses laser irradiation focused in a line onto a solid surface. Lasing occurs in the plasma produced from the surface of the solid target as it expands. A line focus allows amplification along the line focus with high gain to achieve population inversion [23, 24].

Most laser produced plasma experiments have a pre-pulse in order to ensure the main laser pulse interacts with the pre-formed plasma. With EUV lasing, this reduces refraction of the EUV laser beam produced [23, 25, 26].

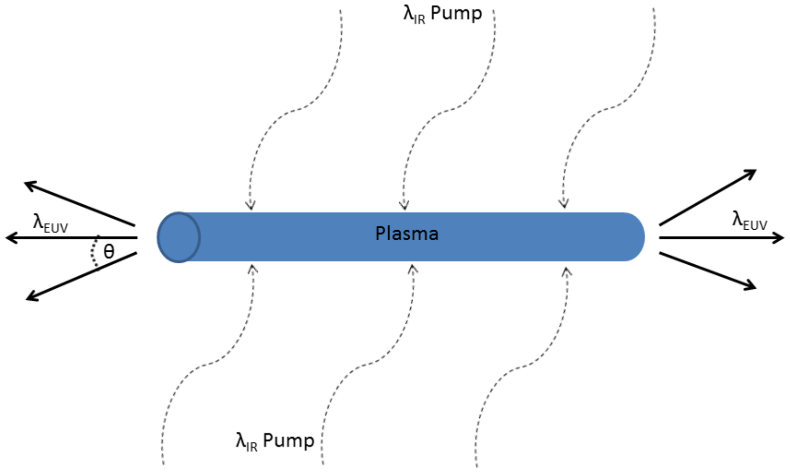

Figure 2.2: EUV laser based on IR laser incident on plasma coloum

An alternative to producing an EUV laser using a slab of solid target, a high aspect ratio plasma column can be formed by firing two pump lasers into a capillary containing the target material, usually a gas (see Figure 2.2). The first pump laser ionises the plasma column and the second more intense pulse creates the population inversion and lasing. The capillary

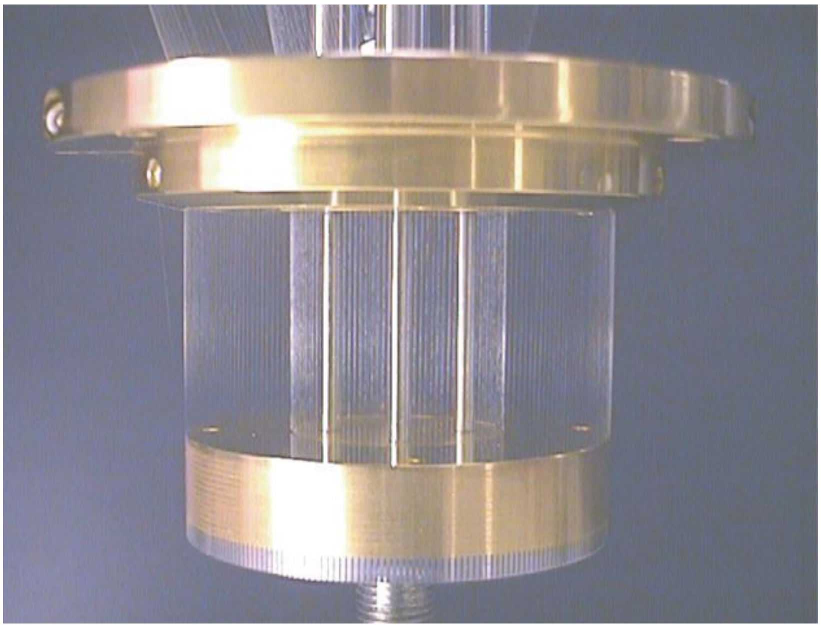

Figure 2.3: Photograph of a nested wire array mounted between two gold-plated electrodes, used at Sandia National Laboratories (from [31])

tube then also acts as a waveguide for the EUV radiation produced.

Producing EUV radiation in this way requires a high power, short pulse optical laser, typically a pico-second pulse of > 1J pulse energy is required. To achieve this work would need to be performed at large national laser facilities and therefore would not be suitable for a University based lab. However, work by Regan *et. al.* shows recent development of diode-driven high energy, high repetition rate, 5ps lasers, and the development of a cryogenic Yb:YAG active mirror amplifier that produces 1.5 J pulses at 500 Hz repetition rate [27].

2.4.5 Z-pinch Wire Arrays

Fast Z-pinches are used to convert the stored electrical energy in a pulsed-power accelerator into soft x-rays and EUV radiation. A large axial current is applied to an array of thin wires causing heating and ionisation to produce a plasma. The magnetic field induced in the array causes a magnetic force ($\tilde{\mathrm{J}} \times \tilde{\mathrm{B}}$) that accelerates the plasma radially inward creating an x-ray source on the cylindrical axis of symmetry [28]. The wire cores continue to ablate due to the heat flux from the nearby plasma. The plasmas produced by this method have a very high temperature and density causing high production of x-rays with energies greater than 1.8MJ and powers in the range of 210TW [29,30].

The characteristics of the produced plasma is demerited by wire number, array mass, and load radius. For example, an array of 300 tungsten wires in an array of diameter 24mm in a 10 mm long cavity has generated x-ray photons of energy 145eV [32].

The high energy x-rays produced from a wire array are ideal for use as radiation sources for Inertial Confinement Fusion (ICF) experiments. Design of hohlaraums have been introduced with wire-arrays incorporated as an x-ray source [31].

Although a z-pinch wire array could be set-up in a university lab, a larger amount of lab space is required to do so.

2.4.6 Capillary Discharge Lasers

Capillary discharge lasers operate in a similar way to the capillary method mentioned in Section 2.4.4 and the z-pinch method in Section 2.4.5. The energy required for ionization and population inversion is provided though an electrical discharge instead of through a laser pulse. A series of ceramic high-voltage capacitors are charged to a chosen voltage, and discharged through a capillary channel (for more detail see Chapter 5) [33].

EUV capillary discharge lasers use Ne-like Argon as the lasing medium. The argon is pre-ionised by a RF pulse to produce a uniform plasma, a pre-ionisation pulse ionises the argon plasma, then a high voltage pulse causes the amplification in the $3s^1P_1 - 3p^1S_0$ transitions of Ar^{8+} ions, and compresses the plasma in a Z-pinch, which causes the population inversion and produces energy of wavelength 46.9nm [34]. The physics of the capillary laser is discussed more in Chapter 5.

2.5 Conclusions

A number of methods of producing warm dense matter by EUV radiation have been investigated. The method most suited to this research is the Capillary discharge laser. The other methods mentioned above require larger laser systems or access to laser facilities. This both limits time and can be expensive. The capillary discharge laser is table top sized and can be added to a current lab set-up making it the ideal method of producing EUV radiation for this research.

Chapter 3

The Interactions and Optics of EUV Radiation

This chapter discusses the interactions of EUV radiation produced by a capillary discharge laser at a wavelength of 46.9nm. The absorption processes of inverse bremsstrahlung and photo-ionisation are discussed along with the difficulties of working with this wavelength experimentally due to the high absorption. A design for scandium silicon multilayer mirrors to give approximately 50% reflectivity is discussed.

3.1 Absorption Processes

The main absorption processes occurring in materials irradiated by EUV radiation are inverse bremsstrahlung and photo-ionisaton [23, 35].

Bremsstrahlung acceleration occurs when one electron, passes within a distance of closest approach of a positively charged nucleus and is accelerated. A large number of incident electrons and a variety of impact parameters means a broad continuum of radiation is produced [1]. Following work by Tallents [37] we find the acceleration of the electron depends on the charge of the ion ($+Z_ie$) and on the distance of closest approach (p), where

$$\frac{dv}{dt} = \frac{1}{4\pi\epsilon_0}\frac{Z_ie^2}{m_0p^2}. \tag{3.1}$$

If a bremsstrahlung pulse lasts for time, t_a and if the collision occurs over a time $2p/v$, when Fourier analysed the dominant part of the frequency spectrum becomes

$$\omega = \frac{1}{t_a} = \frac{v}{2p}. \tag{3.2}$$

The power radiated by an accelerated charge can then be given by

$$Pt_a = \Big(\frac{e^2}{4\pi\epsilon_0}\Big)^3 \frac{4}{3c^3} \frac{Z_i^2}{m_0^2 p^3 v}. \tag{3.3}$$

The number of collisions per unit time per electron between p and $p + dp$ is

$$n_{Z_i} v 2\pi p dp, \tag{3.4}$$

where n_{Z_i} is the ion density. This gives the power in frequency range $\omega + d\omega$ due to one electron,

$$\frac{dE(\omega)}{dt} d\omega = Pt_a n_{Z_i+1} v 2\pi p dp = \Big(\frac{e^2}{4\pi\epsilon_0}\Big)^3 \frac{4}{3c^3} \frac{Z_i^2}{m_0^2 v} 2\pi n_{Z_i} d\omega. \tag{3.5}$$

To calculate the power radiated by all electrons, we integrate over the velocity distribution for all electrons which have enough energy to produce photons of energy $\hbar\omega$. The number of electrons per unit volume with velocity between v and $v + dv$ for a Maxwellian distribution is given by,

$$f_v(v)dv = n_e \Big(\frac{m}{2\pi k_B T}\Big)^{3/2} 4\pi v^2 \exp\Big(-\frac{m_0 v^2}{2k_B T}\Big) dv. \tag{3.6}$$

To find the total power $\epsilon_{tot}(\omega)d\omega$, we integrate Equations (3.5) and (3.6) over ω to $\omega + d\omega$,

$$\epsilon_{ff}(\omega) = \int_{(2\hbar\omega/m_0)^{1/2}}^{\infty} \frac{dE(\omega)}{dt} f_v(v) dv, \tag{3.7}$$

giving this per unit time per unit volume,

$$\epsilon_{ff}(\omega)d\omega = 16\sqrt{\pi}\Big(\frac{e^2}{4\pi\epsilon_0}\Big)^3\frac{4}{3c^3}\frac{Z_i^2}{m^2}n_e n Z_i\Big(\frac{m_0}{2k_BT}\Big)^{1/2}I_{ff}d\omega \tag{3.8}$$

where

$$I_{ff} = \int_{\sqrt{\frac{\hbar\omega}{k_BT}}}^{\infty} x\exp(-x^2)dx. \tag{3.9}$$

which gives

$$\epsilon_{ff}(\omega)d\omega = 8\sqrt{\pi}\Big(\frac{e^2}{4\pi\epsilon_0}\Big)^3\frac{4}{3c^3}\frac{Z_i^2}{m_0^2}n_e n Z_i\Big(\frac{m_0}{2k_BT}\Big)^{1/2}\exp\Big(-\frac{\hbar\omega}{k_BT}\Big)d\omega \tag{3.10}$$

showing that the electron temperature can be measured through power measurements over a range of frequencies.

Bremsstrahlung is the dominant radiation process for high temperature plasmas of low atomic number. The total bremsstrahlung emission can be used for radiation loss calculations and can be found by integrating Equation (3.10) over all frequencies,

$$\epsilon_{fftot} = \int_{\omega=0}^{\infty}\epsilon_{ff}(\omega)d\omega = 4\sqrt{2\pi}\Big(\frac{e^2}{4\pi\epsilon_0}\Big)^3\frac{4}{3\hbar c^3}\frac{Z_i^2}{m_0^{1.5}}n_e n Z_i\big(k_BT\big)^{1/2} \tag{3.11}$$

which depends on the ion charge (Z_i), Temperature (T) and densities (n) [36, 37].

Inverse bremsstrahlung the opposite process, where an electron passes within the field of an ion and absorbs energy from electromagnetic radiation. If the rates of bremsstrahlung and inverse bremsstrahlung are equal the radiation field is in equilibrium, from this the absorption coefficient for inverse bremsstrahlung (K_{ib}) can be obtained. This relationship between inverse processes is known as Kirchhoff's law. Applying Kirchhoff's law we write that

$$k_{ff} < I_p(\omega) >= \epsilon_{ff}(\omega) \tag{3.12}$$

where the term $< I_p(\omega) > d\omega$ is the black body radiation intensity for frequencies ω to $\omega + d\omega$, where

$$< I_p(\omega) >= \frac{\hbar\omega^3}{\pi^2 c^2} \frac{1}{\exp\left(\frac{\hbar\omega}{k_B T}\right) - 1} \tag{3.13}$$

which gives the absorption coefficient for inverse bremsstrahlung,

$$K_{ff} = 8\sqrt{\pi}\left(\frac{e^2}{4\pi\epsilon_0}\right)^3 \frac{4}{3c^2} \frac{Z_i^2}{m_0^2} n_e n_{Z_i} \left(\frac{m_0}{2k_B T}\right)^{1/2} \frac{\pi^2 c^2}{\hbar\omega^3}\left(1 - \exp\left(-\frac{\hbar\omega}{k_B T}\right)\right) \tag{3.14}$$

Photo-ionisation occurs when a photon is absorbed by an atom causing the emission of a photo-electron which has an energy equal to the energy of the incident photon minus the binding energy of the emitted photo-electron [1]. The expression for the absorption coefficient for photo-ionisation can be obtained using Kirchhoff's law from the power emitted by recombination radiation,

$$\epsilon_{fb}(\hbar\omega) = 8\sqrt{\pi}\left(\frac{e^2}{4\pi\epsilon_0}\right)^3 \frac{4}{3c^2} \frac{Z_i^2}{m_0^2} n_e n_{Z_i} \left(\frac{m_0}{2k_B T}\right)^{1/2} \left[\frac{2R_d Z_i^2}{n^3} \frac{e^{\frac{E_{ion}}{k_B T}}}{k_B T}\right] e^{-\frac{\hbar\omega}{k_B T}} \tag{3.15}$$

which is the same as Equation (3.11), the power radiated by bremsstrahlung multiplied by $\left[\frac{2R_d Z_i^2}{n^3} \frac{e^{\frac{E_{ion}}{k_B T}}}{k_B T}\right]$, which shows the dependencies on, photon energy, electron temperature, ion charge, and electron and ion density. The main difference being that recombination radiation only applies to photon energies greater than the ionisation energy of the quantum state involved.

Photo-ionisation is the inverse to recombination, so in an equilibrium plasma the absorption coefficient for photo-ionisation is related to the power emitted in radiative recombination by,

$$K_{bf} < I_p(\omega) \tag{3.16}$$

where $I_p(\omega)$ is the black body radiation intensity over the frequency range ω to $\omega + d\omega$. From Equation (3.15) we can obtain the photo-ionisation absorption coefficient,

$$K_{bf} = 8\sqrt{\pi}\left(\frac{e^2}{4\pi\epsilon_0}\right)^3 \frac{4}{3c^2} \frac{Z_i^2}{m_0^2} n_e n_{Z_i} \left(\frac{m_0}{2k_B T}\right)^{1/2} \frac{\pi^2 c^2}{\hbar\omega^3}\left(1 - e^{-\frac{\hbar\omega}{k_B T}}\right) C_b f \tag{3.17}$$

where C_bf is given by

$$C_bf = \Big[\frac{2R_dZ_i^2}{n^3}\frac{e^{\frac{E_{ion}}{k_BT}}}{k_BT}\Big]. \tag{3.18}$$

Assuming the system is in local thermodynamic equilibrium at high electron densities, the populations of ionisation stages are in equilibrium and the ratio of the ground state population of two quantum states in adjacent ionization stages can be given by the Saha equation [23]. The Saha-Boltzmann ratio for n_{Z_i+1}/n_{Z_i} can be used to obtain the absorption coefficient for photo-ionisation in terms of the population of the ion absorbing radiation,

$$K_{bf} = 32\pi^2\frac{gZ_i+1}{gZ_i}\Big(\frac{e^2}{4\pi\epsilon_0}\Big)^3\frac{4}{3c^2}\Big(\frac{1}{h}\Big)\frac{\pi^2c^2}{\hbar\omega^3}\Big(1-\exp\Big(-\frac{\hbar\omega}{k_BT}\Big)\Big)\Big[\frac{2R_dZ_i^4}{n^3}\Big]n_{Z_i} \tag{3.19}$$

where gZ_i+1 and gZ_i are degeneracies for the final and initial bound quantum states.

The term $\Big(1-\exp\Big(-\frac{\hbar\omega}{k_BT}\Big)\Big)$ allows for stimulated emission. This will have a negative effect of the photo-ionisation absorption coefficient. The Cross-section for photo-ionisation for a single electron, ignoring stimulated emission is,

$$\begin{cases} \sigma_{bf} = K_bf/n_{z_i} \\ = 32\pi^2\frac{gZ_i+1}{gZ_i}\left(\frac{e^2}{4\pi\epsilon_0}\right)^3\frac{4}{3c^2}\left(\frac{1}{h}\right)\frac{\pi^2c^2}{\hbar\omega^3}\left[\frac{2R_dZ_i^4}{n^3}\right] \\ = \frac{16}{3\pi}\frac{gZ_i+1}{gZ_i}\alpha^3\frac{\pi^2c^2}{\hbar\omega^3}\left[\frac{2R_dZ_i^4}{n^3}\right] \end{cases} \tag{3.20}$$

where

$$\alpha = \frac{e^2}{4\pi\epsilon_0\hbar c} \approx \frac{1}{137} \tag{3.21}$$

As the photo-ionisation is an atomic parameter, it is independent of any plasma parameters. This means that the above equation is dependent on the ionisation energy, where if the photon energy is less than the ionisation energy the cross-section is equal to zero, therefore the above equation only applies if the photon energy is greater than the ionisation energy [37,38].

3.2 Refractive indices in the EUV

The refractive index of a material is determined by the sum of scattered radiation from all atoms that interfere with the incident wave to produce a forward propagating wave. The refractive index of EUV radiation tends to deviate from unity by very small amounts, and can be written as,

$$n(\omega) = 1 - \delta + i\beta \tag{3.22}$$

where, δ and β are the real and imaginary parts of the refractive index respectively and are related to the scattering factors $f_1^0(\omega)$ and $f_2^0(\omega)$ by,

$$\delta = \frac{n_a r_e \lambda^2}{2\pi} f_1^0(\omega), \tag{3.23}$$

$$\beta = \frac{n_a r_e \lambda^2}{2\pi} f_2^0(\omega), \tag{3.24}$$

where n_a is the atomic density and r_e is the classical electron radius. By measuring phase shift and absorption in materials, δ and β can be determined. However, due to the difficulty of interferometry at EUV wavelengths it is often not possible to get accurate measurements. Instead we can return to Equations (3.23) and (3.24) and use the Kramers-Kronig relations for the the complex scattering factor $f^0(\omega)$,

$$f_1^0(\omega) = Z - \frac{2}{\pi} Pc \int_0^\infty \frac{u f_2^0(u)}{u^2 - \omega^2} du \tag{3.25}$$

$$f_2^0(\omega) = \frac{2\omega}{\pi} Pc \int_0^\infty \frac{u f_1^0(u) - Z}{u^2 - \omega^2} du \tag{3.26}$$

where Z is the number of electrons per atom and Pc is the Cauchy principal value. The Kramers-Kronig relations relate the real and imaginary parts of a physical "response" to a "stimulus" in linear systems. They allow the refractive index profile and the chromatic dispersion of a medium to be calculated, solely from its frequency-dependent losses, which

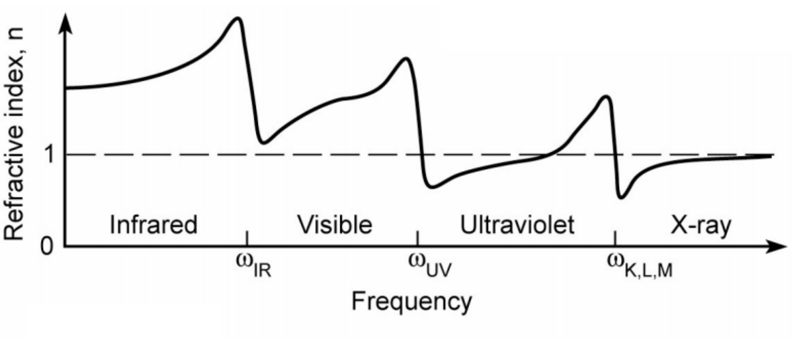

Figure 3.1: The real part of the refarcive index variations in the infrared to x-ray region of the electromagnetic spectrum, note that at EUV wavelengths refractive index is close to or less than one [1]

can be measured over a large spectral range. If either the real or imaginary part of Equations (3.25) and (3.26) are already known, this is enough to determine the other part. If f_2^0 is determined through absorption methods across a range of frequencies, then f_1^0 can be deduced [1]. Some work has been undertaken to experimentally confirm the EUV and soft x-ray values for f_1^0 and f_2^0, using techniques such as interferometry [2].

The real refractive index over a range of frequencies from the IR to x-ray ranges in the electromagnetic spectrum are schematically plotted in Figure 3.1. This shows that the EUV region will typically have real refractive index values of less than one. This is due to the high atomic resonances at lower frequencies in this spectral range. EUV radiation is mainly absorbed by electrons in the conduction band, so the refractive indices are similar to those in a plasma ($n < 1$).

Due to the high absorption it is very difficult to manipulate EUV radiation at near normal incidence. The radiation is absorbed by most reflective and refractive optics, so it was not until the development of multilayer mirrors that EUV radiation could be more widely studied at normal incidence [1]. In Section 3.5 we discuss the reflectivity of multilayer mirrors, where the waves which are reflected as they pass through the multilayer are added constructively at certain angles to produce a Bragg effect and give a significant increase in reflectivity [39].

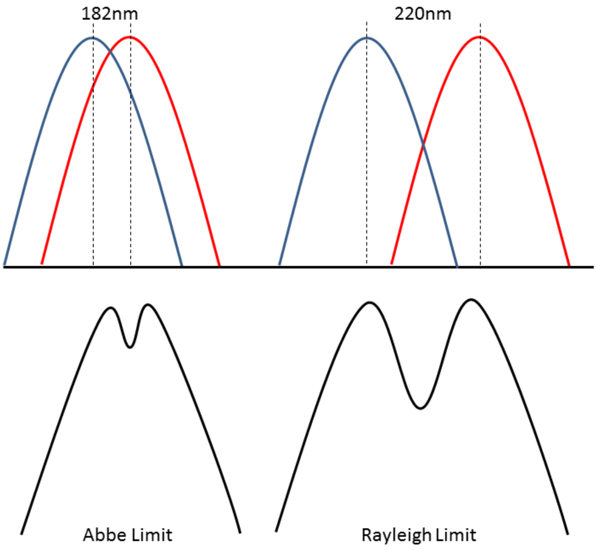

Figure 3.2: An example of the Abbe and Rayleigh criterion for the seperation of two sources for a system with $\lambda = 510nm$ and $NA = 1.4$.

3.3 Diffraction

A short wavelength laser such as the capillary discharge laser operating at 46.9nm enables focusing in the diffraction limit to diameters $d = \lambda(2N_A)$, where N_A is the numerical aperture of the focusing optic [40].

In the late 19th century Abbe and Rayleigh derived a criterion which describes the minimum distance at which two objects are clearly distinguishable as two separate sources [41]. Abbe's criterion is

$$d = \frac{0.5\lambda}{NA} = \frac{0.5\lambda}{n\sin(\theta)} \tag{3.27}$$

where d is the separation of the two sources, NA is the numerical aperture of the lens, λ is the wavelength of the source, and n is the refractive index of the medium between the two sources.

The difference in the Abbe and Rayleigh criterion is the value of the coefficient, this comes from the difference in opinion of the point at which two sources are distinguishable. Abbe has stated 0.5, as this is the point at which a small dip can be seen between the two maxima of

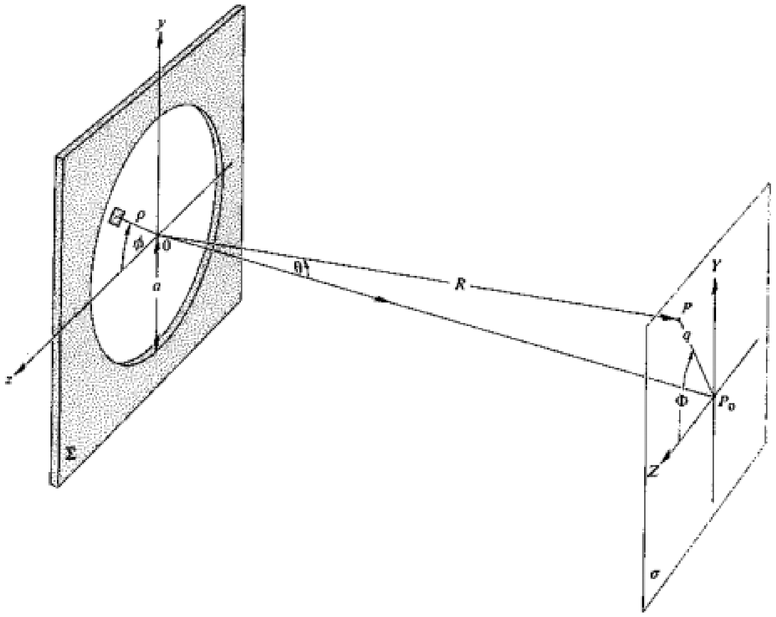

Figure 3.3: Geometry of diffraction from a circular aperture (from [40])

the Airy profiles. Rayleigh stated the coefficient to be 0.61, which is where the first minimum of one Airy profile overlaps the maximum of the second Airy profile, with the sum of the two profiles showing a distinct dip [42]. An example of these differences are shown in Figure 3.2 for a system with wavelength 510nm and numerical aperture 1.4. Abbe's criterion can be used to give an estimate of the half-width half-maximum of a diffraction limited focal spot from the capillary discharge laser.

Capillary discharge lasers, have a small circular beam at the output of the laser so the diffraction theory of a circular aperture can be applied. A circular geometry is also applied when considering the focusing of the laser output. The expression for the electric field at some arbitrary distant point P from a surface is given by integrating the electric field amplitude $\varepsilon(A)$ and phase at the surface. We have following [40] that,

$$\tilde{E} = \frac{e^{i(\omega t - kR)}}{R} \int\int_{Aperture} \varepsilon_A e^{ik(Yy+Zz)/R} dS \tag{3.28}$$

where $\tilde{E}$ is the electric field amplitude per unit angle at distance R from arbitrary point P. The geometry of this is shown in Figure 3.3.

The intensity can then be given as,

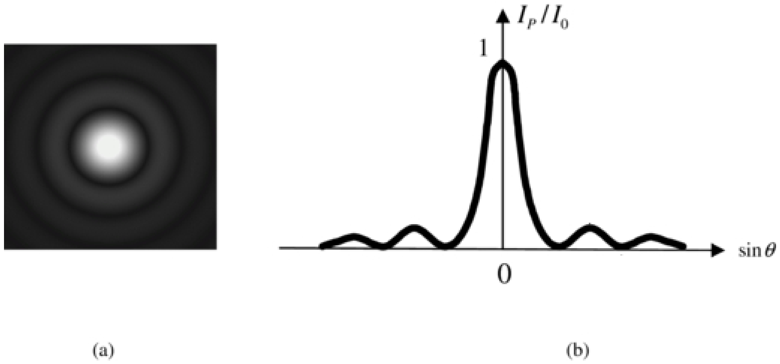

Figure 3.4: (a) Airy disk from the diffraction pattern from a circular aperture on a screen (b) Plot of the irradiance of an Airy disk produced by the diffraction pattern from a circular aperture (from [43])

$$I(\theta) = I(0)\left[\frac{2J_1(ka\sin\theta)}{ka\sin\theta}\right]^2 \tag{3.29}$$

where θ is the diffraction angle of the beam, J_1 is the first order Bessel function, and a is the spherical coordinate where $z = a\cos\theta$.

This can now be plotted to produce what is known as an Airy Disk, an example of which is shown in Figure 3.4. The Airy disk has a central maximum column, which because of the circular symmetry produces a high irradiance circular spot with ripples spreading outwards from the central spot [40].

3.4 Aberrations

Aberrations in an optical system arise when rays varying in angle, position and/or wavelength focus to different positions on a surface of interest. Chromatic aberrations arise from the wavelength variation of refractive indices. For the work in this thesis we are only concerned with a single wavelength of 46.9nm and therefore chromatic aberrations will not be an issue.

Spherical aberrations are differences in focused position of rays created by a spherical mirror or focusing optic. Figure 3.5 shows an example of spherical aberration, where marginal and paraxial rays, which represent the inner-most and outer-most extreme rays, focus at different points along the optical axis [44].

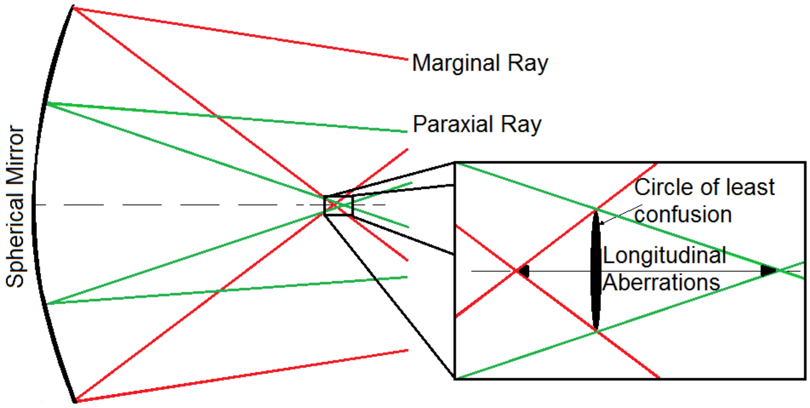

Figure 3.5: Terms used for the focusing effects of spherical aberration from a spherical mirror.

For a first order paraxial image, Fermat's principle can be applied to get an approximation for focal distance. We have,

$$\frac{n_1}{s_o}\frac{n_2}{s_i}=\frac{n_2-n_1}{R} \tag{3.30}$$

where R is the radius of curvature of a spherical lens, s_o is the object distance and s_i is the image distance, n_1 and n_2 are the refractive indices of material for the incident ray and the refractive material respectively [40, 44].

When applying Fermat's principle to third order spherical aberrations which include marginal rays we get,

$$\frac{n_1}{s_o}\frac{n_2}{s_i}=\frac{n_2-n_1}{R}+h^2\left[\frac{n_1}{2s_o}\left(\frac{1}{s_o}+\frac{1}{R}\right)^2+\frac{n_2}{2s_i}\left(\frac{1}{R}-\frac{1}{s_i}\right)^2\right] \tag{3.31}$$

where h is the height above the optical axis at which the incident ray strikes the spherical interface [40]. Marginal rays with a higher value for h bend more towards the optic axis and are thus focused in front of the paraxial rays. This difference in focusing position is a measure of the longitudinal spherical aberrations (Figure 3.5). In Figure 3.5 a positive longitudinal aberration is shown. The height above the optical axis at which a given ray strikes a screen is a measure of the transverse spherical aberrations.

Aberrations can be reduced by stepping down the aperture but this will also reduce the amount of light entering the system. The best focus will be achieved at the point where

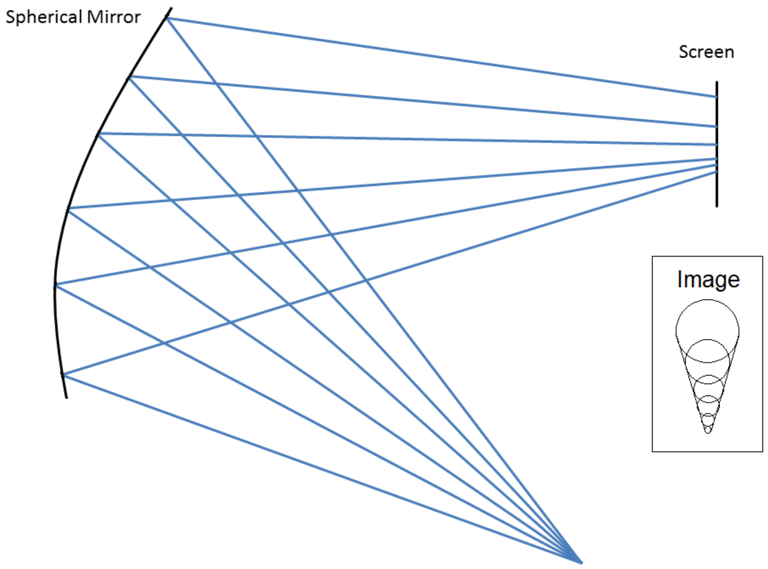

Figure 3.6: Example of coma aberrations where the focus is displaced from the optic axis.

the distance between the marginal and paraxial rays is smallest. This is known as the circle of least confusion as this is the area with the smallest amount of blur around the focal spot [40, 44].

For an object which is lying on the optical axis of a cylindrically symmetric system, the image will experience only spherical aberrations and will not have any aberrations caused by any of the other primary monochromatic aberrations. The image of an object which is lying off axis can experience coma and astigmatism, as well as spherical aberrations [44].

Coma is a similar effect to spherical aberrations, however the off axis object causes the marginal and paraxial rays to focus at different distances above or below the optical axis. The focal lengths and therefore magnifications will be different for rays striking the lens at different angles [40] this is demonstrated in Figure 3.6. The effect is called coma (Latin for comet) because the off axis tilt causes the shape of the focus to change from being a perfect circle to being a elongated comet like shape, this is also shown in Figure 3.6.

Astigmatism occurs when an object is quite a large distance from the optical axis. Incident rays strike the lens asymmetrically which causes aberrations [40]. If the focal length of the lens is different for different planes of incident light, there will be no point where all the rays from the object reach a sharp focus, thus causing astigmatism. Figure 3.7 shows that rays in the tangential plane are focused closer to the lens than rays in the sagittal plane. For the sagittal plane, the extreme rays are symmetric with respect to the central ray. For the tangential plane, the pathlengths and angles of incidence on the lens surface are different for the top and bottom rays [45]. The effects of this are shown in Figure 3.8 , where a wheel imaged using a perfect lens with no astigmatism, is compared to the image at the sagittal focus where the spokes of the wheel are in focus but the rim is not, and to the tangential focus where the rim of he wheel is in focus but the spokes are not.

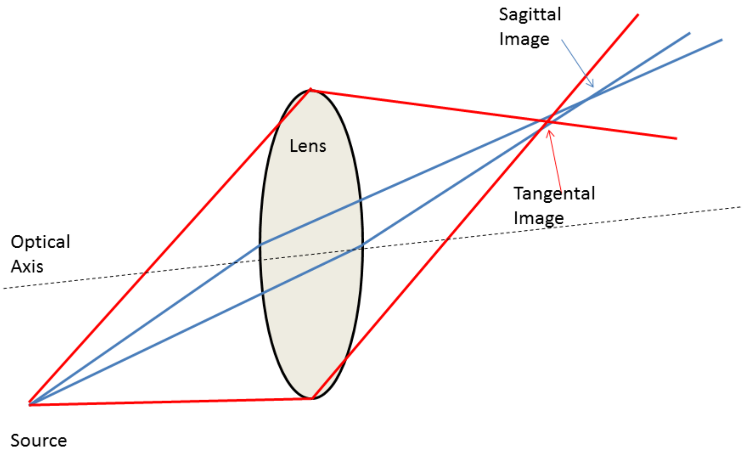

Figure 3.7: Example of astigmatism caused by incident rays striking the lens asymmetrically

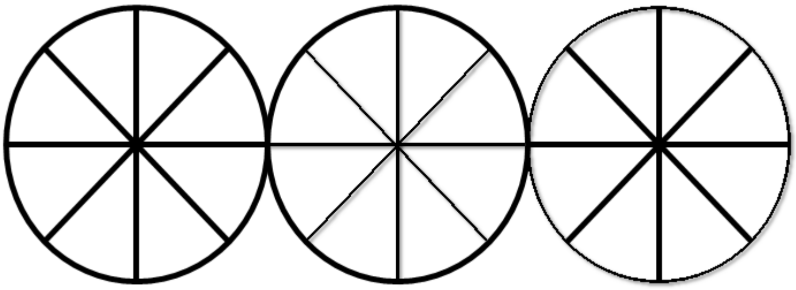

Figure 3.8: Examples of the effect of astigmatism on focused imgaes. The left figure has no astigmatism, centre is focued in the sagittal plane and right is focused in the tangential plane.

3.5 Multilayer Mirrors

Multilayer mirrors have been used successfully in the EUV wavelength range since the 1960s. Molybdenum and silicon mirrors work very well at 13.5nm and have been shown to have reflectivities of over 70%. Molybdenum/silicon mirrors are now used in EUV semi-conductor lithography [46]. Based on the success of Mo/Si mirrors, we will investigate the design of Sc/Si mirrors. These have previously been used with capillary discharge lasers and have shown to have reflectivities of approximately 40% at 46.9nm [47]. However Sc/Si mirrors were not originally designed to be used at 46.9nm therefore, if the mirrors are fully optimised it may be possible to increase this reflectivity.

Multilayer mirrors consist of alternating layers of two materials, usually one material of high atomic number and one with low atomic number. These layers will have a thickness of a few nm and are designed so that the reflection at the boundaries between layers interfere constructively. The Fresnel equations determine the reflection and transmission at the boundary of the two different layers [39]. For example at normal incidence peak reflectivity occurs when the incident wavelength is approximately equal to twice the multilayer period or bi-layer thickness. Peak reflectivity is achieved where the values of λ and θ satisfy the Bragg condition at non-normal angle of incidence (θ) [1].

The real refractive index from Equation (3.22), can be used to find the refraction at the interface of two layers of a multi-layer mirror using Snells law,

$$n_1 \sin\theta_i = n_2 \sin\theta_r \tag{3.32}$$

which gives the reflectivity for s and p polarised light at the interface between two materials of different refractive index,

$$R_s = |\frac{n_1 \cos\theta_i - n_2 \cos\theta_t}{n_1 \cos\theta_i + n_2 \cos\theta_t}|^2 \tag{3.33}$$

$$R_p = |\frac{n_1 \cos\theta_t - n_2 \cos\theta_i}{n_1 \cos\theta_t + n_2 \cos\theta_i}|^2 \tag{3.34}$$

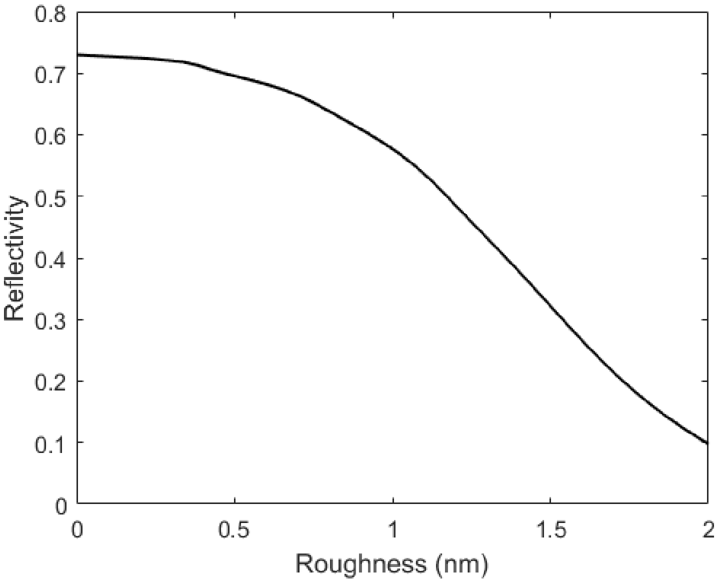

Figure 3.9: The reflectivity of a molybdenum/silicon mirror of bilayer thickness D=7nm and a layer thickness ratio of $\Gamma = 0.5$ at wavelength 13.48 nm as a function of the surface roughness between layers for normal angles of incidence

the transmission can then be given as $T = 1 - R$.

The software package IMD [48] solves the Fresnel equations (Equations (3.22), (3.33) and (3.34)) for a multi-layer stack to give optical parameters such as, reflectivity, phase and transmission as a function of incident angle, polarisation and wavelength. The roughness of a surface is determined by introducing randomised height variations at the reflective surface.

Any imperfections in the manufacture of the mirror, either arising as surface roughness or a diffuse interface between layers gives rise to losses in the specular reflectance [49]. The surface roughness is the measure of the height of surface irregularities. Increasing the surface irregularities causes a decrease in the reflectivity due to the scattering possibilities at the rough surface [50]. The IMD code has been used to produce Figure 3.9 which shows increasing the surface roughness of a Mo/Si multi-layer reduces the reflectivity significantly over just a few nm.

IMD has been used to produce a reflectivity curve for Sc/Si mirrors (Figure 3.10). Here the bilayer thickness (D) is set to 23nm and layer thickness ratio (Γ) is 0.6. Altering the bilayer thickness and layer thickness ratio of the multi-layer materials can change the peak reflectivity and the optimum wavelength.

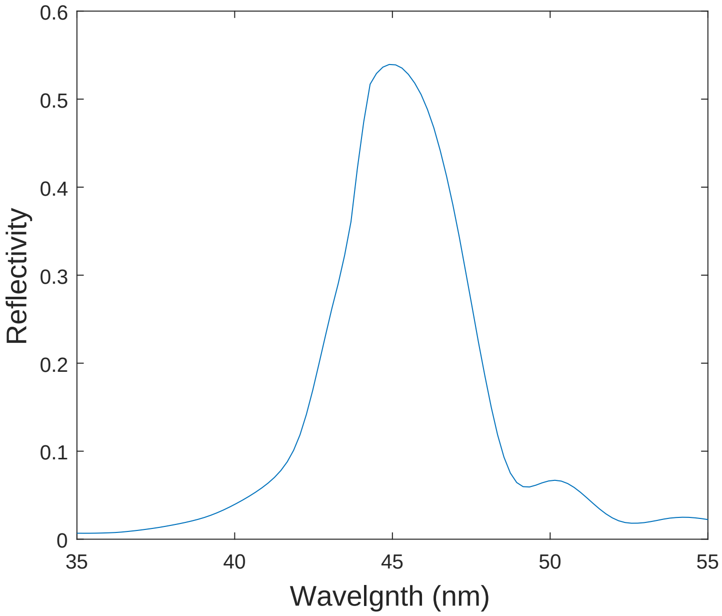

Figure 3.10: The reflectivity of a scandium/silicon mirror of bilayer thickness D=23nm and Γ=0.6 at wavelength 46.9 nm for normal angles of incidence, assuming surface roughness is less than or equal to 1nm.

Scandium silicon multi-layer mirrors have been manufactured to achieve a high reflectivity at 46.9nm, making them ideal for use with a capillary discharge laser. Scandium is used as it has a high refractive index and low absorption at 46.9nm. Silicon is used as a low refractive index spacer material, as it is often used as a coating or substrate for optics [47, 51].

Figure 3.10, shows a reflectivity curve giving approximately 50% reflectivity for 46.9nm wavelength [52]. It is possible to optimise the mirrors to increase this reflectivity. Figure 3.11 shows the curves for different bilayer thickness's and layer thickness ratios at 46.9nm. From Figure 3.11 these conditions have been optimised to give the highest possible reflectivity at 46.9nm, where D=26nm and $\Gamma = 0.4$ which gives a reflectivity of 56%, in agreement with values predicted by Yulin [52].

The number of layers and the surface roughness of mirrors must be optimised for maximum reflectivity. If there are too few layers the light will pass through the mirror. If there are too many layers the light does not reach the lower levels. The cost of mirrors is partly determined by the number of layers, so having unnecessary non-reflecting layers can be an unnecessary expense. In Figure 3.13 the reflectivity at a wavelength of 46.9nm has been calculated for varying numbers of layers. There is a general increase in reflectivity with the

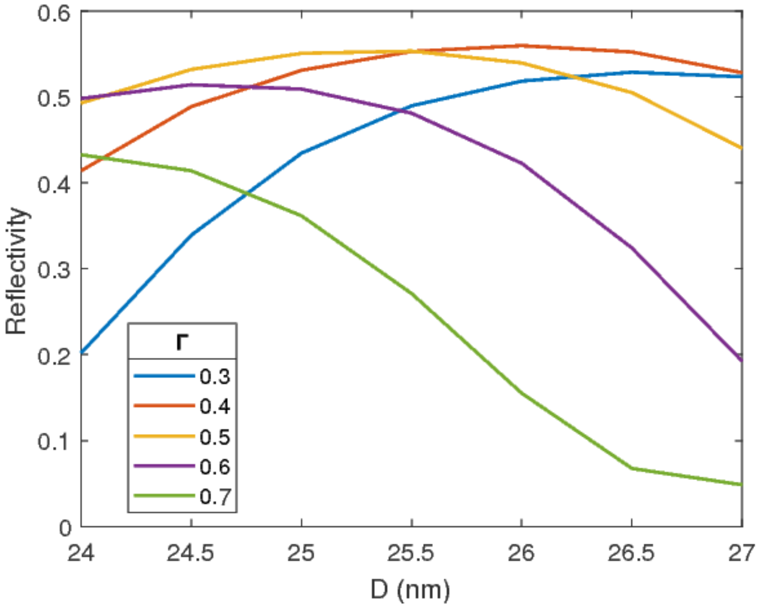

Figure 3.11: The reflectivity of scandium/silicon mirrors with values of Γ=0.3, 0.4, 0. 5. 0.6 and 0.7 (as labelled) at wavelength 46.9 nm as a function of the bilayer thickness D assuming normal angles of incidence. The layer surface roughness is assumed to be less than or equal to 1nm.

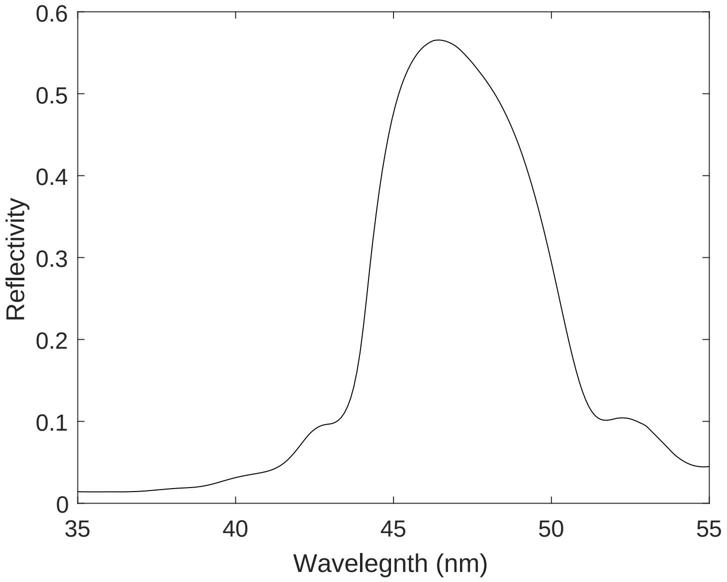

Figure 3.12: The reflectivity of a scandium/silicon mirror of bilayer thickness D=26nm and Γ = 0.4 as a function of wavelength at normal angles of incidence. The layer surface roughness is assumed to be less than or equal to 1nm.

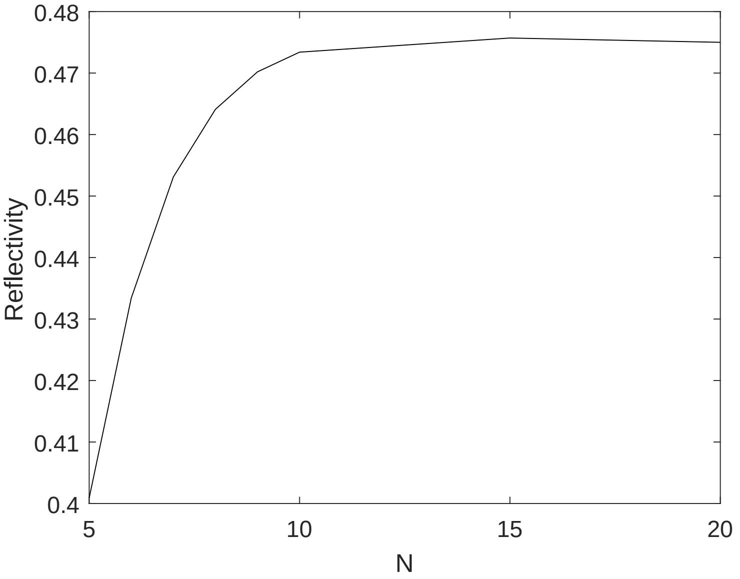

Figure 3.13: The reflectivity of a scandium/silicon mirror with a bilayer thickness of D=26nm nm and Γ =0.4 at wavelength 46.9nm as a function of number of bilayers (N). The layer surface roughness is assumed to be less than or equal to 1nm.The reflectivity does not increase significantly when the number of layers N increases above 10.

number of layers then the reflectivity curve will plateau (Figure 3.13).

The effect of varying surface roughness is shown in Figure 3.14. Realistic values for roughness depends on the layer deposition process and surface polishing.

With the optimum conditions for reflectivity established for the Sc/Si mirrors, we can now study how the reflectivity changes as a function of incident angle. Figure 3.15 shows the peak reflectivity of a mirror for radiation incident at various angles for a wavelength of 46.9nm. Importantly the reflectivity of the mirror stays above 40% for angles of less than 18°.

3.6 Gold Mirrors

The IMD code has also been used to simulate the reflectivity of un-protected gold coated mirrors. Although a lower reflectivity is expected for the gold mirrors they are readily available as an off the shelf product from most optics companies and cost a fraction of the price of a scandium silicon mirror.

The reflectivity at normal incidence is shown in Figure 3.16. This gives a reflectivity of

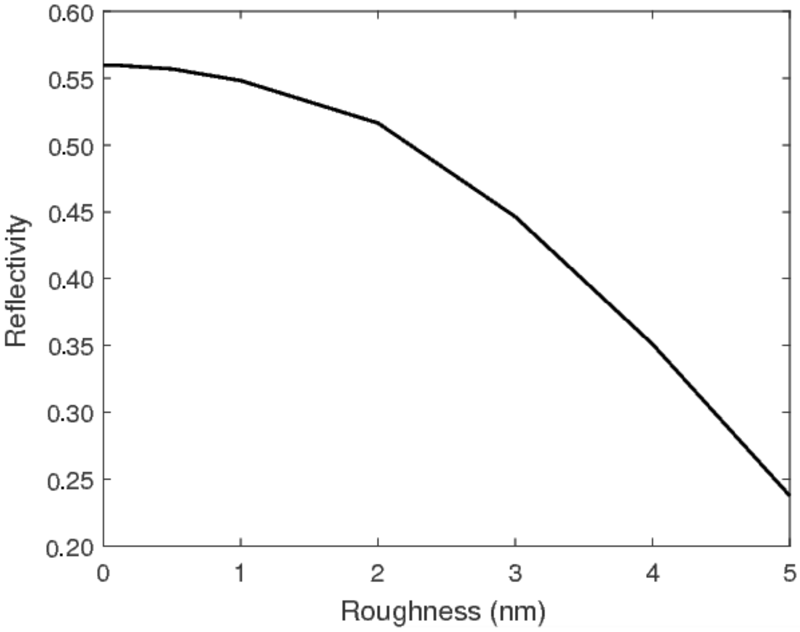

Figure 3.14: The reflectivity of a scandium/silicon mirror of bilayer thickness D=26nm and Γ=0.4 at wavelength 46.9 nm as a function of the surface roughness between layers assuming normal angles of incidence.

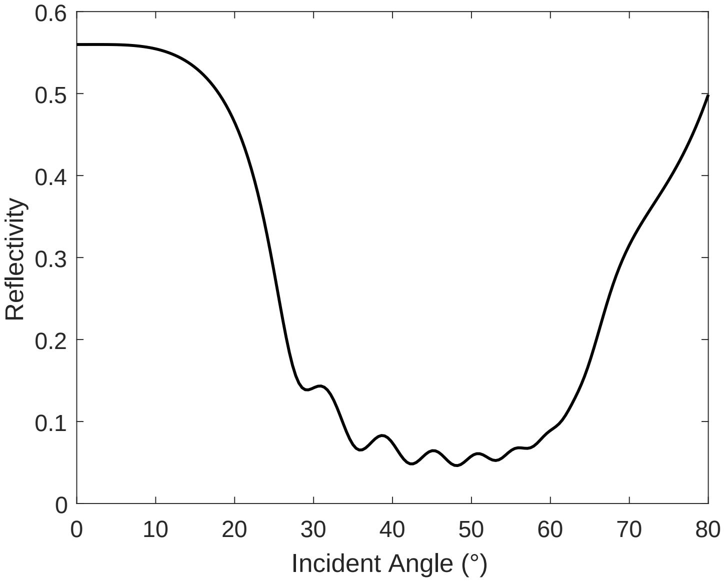

Figure 3.15: The reflectivity of a scandium/silicon mirror of bilayer thickness D=26nm and Γ=0.4 at wavelength 46.9 nm as a function of the angle of incidence. The layer surface roughness is assumed to be less than or equal to 1nm.

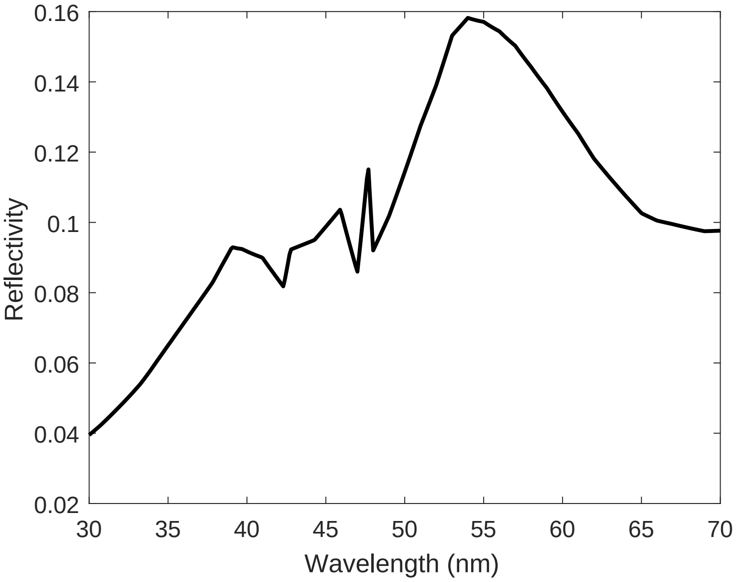

Figure 3.16: The reflectivity of a gold mirror as function of wavelength at normal angles of incidence. The layer surface roughness is assumed to be less than or equal to 1nm.

approximately 8% with optimum conditions. As with the scandium silicon mirrors, the reflectivity reduces as a function of the surface roughness as shown in Figure 3.17. Assuming a reasonable values for the surface roughness the reflectivity as a function of incident angle can then be calculated (Figure 3.18). The dependence on the incident angle shows a more simple trend than for the multi-layer mirrors as there is no interference from the multiple reflections on the alternating surfaces. Figure 3.18 shows that as the incident angle approaches grazing incidence the reflectivity increases. For on-axis a reflectivity of 8% is reasonable for a wavelength of 46.9nm, but grazing incident optics gold mirrors give a comparable reflectivity to the Sc/Si mirrors.

3.7 Conclusions

A review of the absorption processed of EUV radiation and development of both a scandium silicon multilayer mirror and a gold coated mirror has given the mirror coatings that can be used to focus the EUV radiation. The scandium silicon mirrors have been optimised to give a reflectivity of over 50% and studies of gold coating show that at normal incidence they have a reflectivity of 8% increasing with angle of incidence. This shows that both would be suitable for on-axis focusing but the gold mirrors are also well suited for grazing incidence

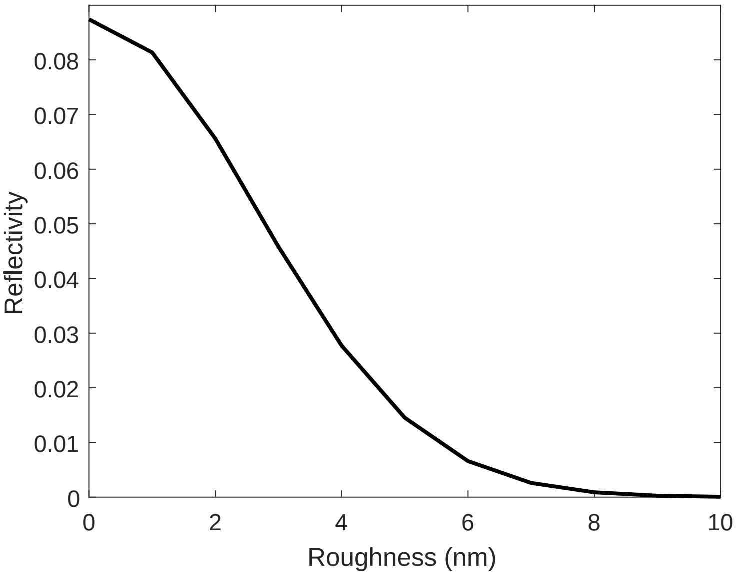

Figure 3.17: The reflectivity of a gold mirror as function of the surface roughness measured at normal incidence for 46.9nm rdiation.

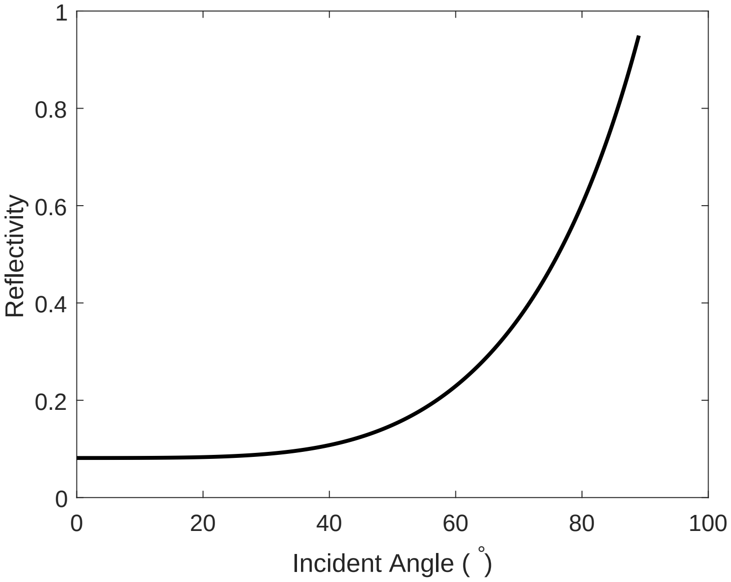

Figure 3.18: The reflectivity of a gold mirror as a function of angle of incidence, assuming the surface roughness is less than or equal to 1nm for 46.9nm rdiation.

focusing as reflectivity increases with angle of incidence. A review of spherical aberrations and diffraction has shown the limits of focusing. This has lead us to study single mirror on axis focusing in order to reduce the effects of coma and astigmatism, or to use multi-mirror systems in order to cancel out the effects of aberrations caused by off-axis focusing.

Chapter 4

Review of EUV Focusing Techniques

This chapter presents a number of methods for focusing a capillary discharge laser output at 46.9nm. Using information from Chapter 3, on spherical aberrations and multilayer mirrors an investigation into the focusing method which will give the lowest spherical aberrations and the highest focused irradiance has been conducted. There are a number of factors which will determine the suitability of a focusing method. The most important is the available lab area. The capillary discharge laser requires approximately one meter of space from the laser aperture to the experimental chamber, this is to allow for diagnostics and vacuum systems to be installed in appropriate positions. This leaves a distance of 1.3m from the laser aperture to the centre of the experiential vacuum chamber. This chamber being used in this experiment is a 60cm by 60cm square breadboard for mounting optics. This must also be taken into account as focusing systems which need more space will not be suitable. This will also affect the choice of focusing optic due to the beam divergence at that distance. Of these methods the on-axis spherical mirror and Schwarzschild focusing methods are discussed in more detail as these methods are used in experiments and simulations in later chapters.

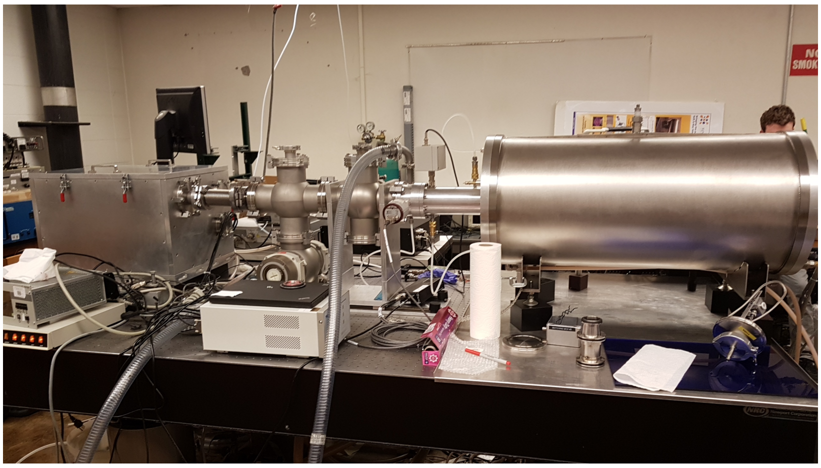

Figure 4.1: Photo of capillary discharge laser set-up with two six-way crosses to allow for differential vacuum pumping and additional diagnostics

Table 4.1: Optical properties and equations for Fresnel zone plates [1].

Diameter of zone plate	$D = 4N\Delta r$
Focal length	$f = \frac{4N(\Delta r)^2}{\lambda}$
F number	$F = \frac{\Delta r}{\lambda}$
Numerical aperture	$NA = \frac{\lambda}{2\Delta r}$
Chromatic blurring	$N < \frac{\lambda}{\Delta\lambda}$

4.1 Fresnel Zone Plates

Fresnel zone plates are circular diffraction gratings used to focus radiation. They typically consist of alternating layers of transparent and opaque material (Figure 4.2), where the radius of the edges of the zone plates are defined by,

$$r^2 = nf\lambda + \frac{n^2\lambda^2}{4} \tag{4.1}$$

where n is the zone number, λ is the wavelength and f is the focal length of the zone plate. This gives the total size of the zone plate. The specification of a zone plate are determined by three parameters, photon energy determined by wavelength, λ, resolution determined by the outer zone width, Δr, and chromatic blurring determined by number of zones, N [1]. From these three, characteristic parameters can be determined (Table 4.1) [53].

The efficiency of a zone plate is approximately 10%. This is because the alternating transparent and opaque zones will only transmit 50% of incident radiation, and because a significant fraction of light is diffracted into other orders. Fresnel zone plates are also expensive to make

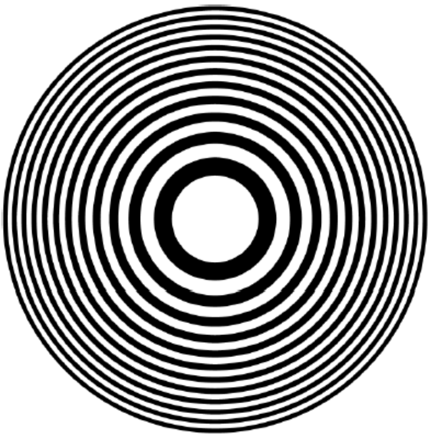

Figure 4.2: Fresnel zone plate with alternating black and white regions representing absorbing and transmitting regions.

Table 4.2: Physical properties of Fresnel zone plates used to focus capillary discharge laser

Focal Length	2.1mm
Outer diameter	0.5mm
Outer zone width	200nm
Number of zones	625
Central opening	50μm

and so has very small diameters. In this case the Fresnel zone plate has an outer diameter of 0.5mm (Table 4.2) this will only focus a very small portion of the EUV beam.

In order to satisfy the equations in Table 4.1 zone plates have been made with physical properties listed in Table 4.2 [33] and used to focus a capillary discharge laser. The parameters listed in Table 4.2 provide a focal spot diameter of approximately 200 nm close to the diffraction limit. However, the limited diameter of the zone plate and the divergence of the beam from the capillary discharge laser, means the zone plate is too small to focus the full beam of a capillary discharge laser. This reduces the efficiency of the zone plate to approximately 3%, giving a focused intensity on the order of 10^9W/cm^2 for a capillary discharge laser [33].

4.2 Off-Axis Spherical Mirrors

Multilayer mirrors as described in Chapter 3 have been used to focus the capillary laser output at non-normal angles of incidence. Such a geometry means that the target does not

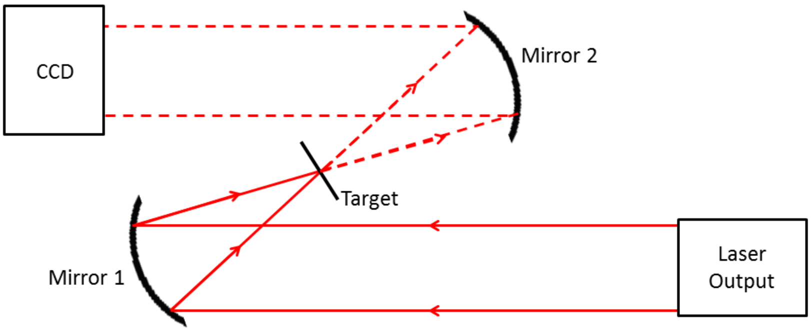

Figure 4.3: Experimental set-up for off-axis spherical mirror experiments.

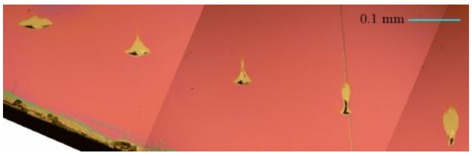

Figure 4.4: Microscope image of an ablation profile after 100 shots on a parylene-N target obtained using an off-axis focussed mirror at 46.9nm radiaiton; adjacent spots were exposed 0.1 mm apart along the beam propagation axis [54].

block the incoming beam, but the arrangement does result in significant aberration in the focus.

In the experiment reported by Aslanyan et al [54], a second mirror was employed to image the capillary laser beam transmitted through the targets onto a CCD detector (see Figure 4.3). Although this method allows for measurements to be taken of the energy transmitted through the target simultaneously, the post shot analysis has shown major coma aberrations (Chapter 3) in the focal spot (Figure 4.4).

Having these aberrations increases the diameter of the focal spot size therefore missing the aim of achieving a diffraction limited focal spot diameter. This also reduces the focused intensity on the target to approximately $3 \times 10^{10}\mathrm{W/cm^2}$. Using the same mirror on axis give a focussed intensity of approximately $2.5 \times 10^{12}\mathrm{W/cm^2}$ [54, 55].

4.3 On-axis Spherical Mirrors

Curved mirrors have been used in optics for centuries due to their lens-like properties, the radius of curvature R, of a spherical mirror produces a focus at a distance s_i if the object is at a distance s_o, with a relationship,

$$\frac{1}{s_o} - \frac{1}{s_i} = -\frac{2}{R} \tag{4.2}$$

This is a variation of the lens equation for a mirror, where the focal length is given by

$$f = -\frac{R}{2} \tag{4.3}$$

As for a thin lens, for a spherical mirror parallel off-axis rays are focused to approximately the same point on a focal plane, at a distance f, from the mirror.

In focusing light onto solid targets with a spherical mirror, it is useful to tilt the mirror so that the target does not obscure the incoming light. However, off-axis focusing causes aberrations in the form of coma, astigmatism and spherical aberrations in the focus as outlined in Section 4.2.

With a capillary discharge laser we have a rare opportunity to focus on-axis. The annular shape of the beam allows the radiation to be focused back along the beam path and onto a target in the annulus of the beam without significantly obstructing the beam path as the laser intensity at the centre of the beam is small (Figure 4.5). Using an on-axis spherical mirror minimises coma and reduces spherical aberrations, allowing the potential to have a near-diffraction limited focal spot with little loss of incoming laser radiation arising from a target bocking the beam [56].

We can investigate the aberrations of spherical mirrors using some simple geometry considerations. We calculate the focusing of paraxial rays with angles close to that of an optical axis and marginal rays with the steepest angles to the optical axis. We assume that the mirror focuses a point laser source with a small range of divergence angles. The longitudinal aberration is taken as the difference in distance between where paraxial rays, V_p cross the optical axis and marginal rays, V_m cross the optical axis. The circle of least confusion is

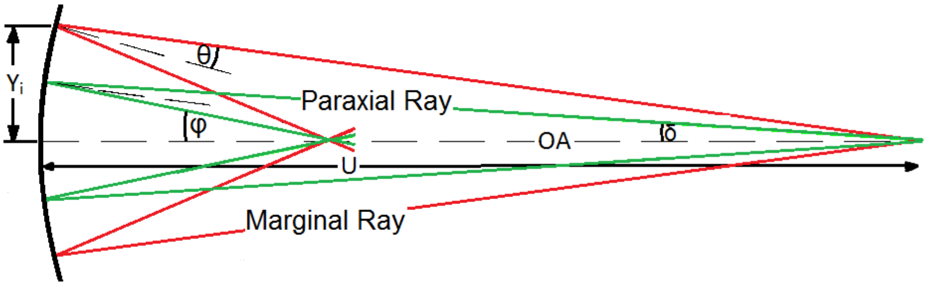

Figure 4.5: Single on-axis spherical mirror focusing.

determined from the longitudinal aberrations and the divergence angle of the focused beam. The divergence angle of the incoming laser beam profile, δ, can be converted to the height above the optical axis (Y_i) at which it strikes the mirror by using,

$$\tan\delta = \frac{Y_i}{U}, \tag{4.4}$$

where U is the distance from the laser source to the mirror. A ray is reflected off the surface of the mirror of radius of curvature R, so that the reflected ray crosses the optical axis at a point V, at angle ϕ, where

$$\phi = 2\Big[\sin^{-1}\Big(\frac{U}{R}\Big)\sin(\delta)\Big] - \delta, \tag{4.5}$$

and

$$V = \frac{U\sin(\delta)}{\sin(\phi)}, \tag{4.6}$$

The longitudinal aberrations (L_A) are then given by,

$$L_A = V_m - V_p, \tag{4.7}$$

where V_m and V_p are the marginal and paraxial rays respectively. The diameter of the circle of least confusion can be calculated to obtain the theoretical focal spot size.

$$D_{clc} = 2\Big(\sin(\phi_m)\frac{L_A\sin(\phi_p)}{\sin(\pi-\phi_m-\phi_p)}\Big) \tag{4.8}$$

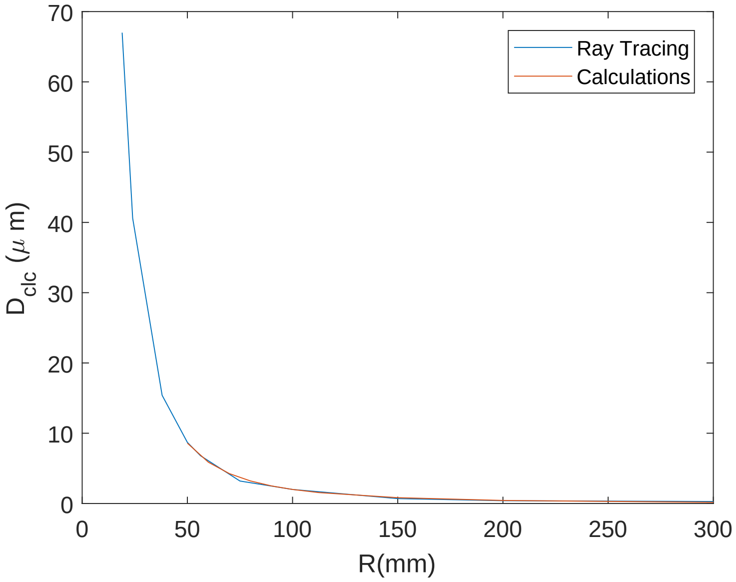

Figure 4.6: The diameter of the circle of least confusion as a function of the radius of curvature of the mirror (R) for calculated values (blue) and CAD ray tracing (red) where distance from laser aperture, U=1.5m. We consider rays at height Y_i=2.5mm and 4.5mm above the optical axis.

where ϕ_m and ϕ_p are the angles at which the marginal and paraxial rays cross the optical axis.

Figure 4.6 shows the diameter of the circle of least confusion as a function of the radius of curvature of a spherical mirror, R, with distance from source, U=1.5m and Y_i=2.5mm and 4.5mm. A 2D CAD modelling programme has been used for ray tracing to confirm the above trigonometric calculations (Figure 4.6). The results show that as the radius of curvature of the mirrors increases, the spherical aberrations decrease.

4.3.1 Diffraction

From Section 3.3 we know that Abbe's criterion can be used as an estimate for the diffraction limit of the focal spot produced from spherical mirrors. Abbe's criterion gives the diameter of a focus as diffraction limited,

$$d = \frac{\lambda}{n\sin(\Phi)}, \tag{4.9}$$

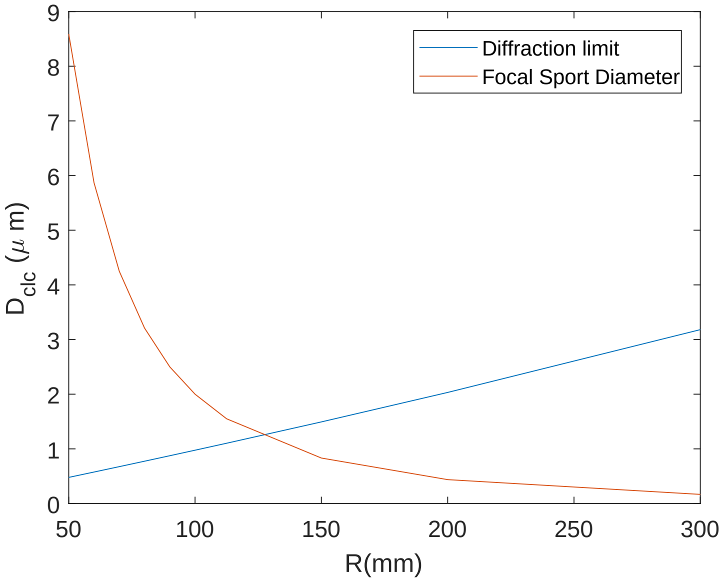

Figure 4.7: The diameter of the diffraction limit from Abbe's criterion (blue) and the diameter of the circle of least confusion measured from CAD ray tracing (red) as a function of the radius of curvature (R) of an on-axis spherical mirror for 46.9nm radiation.

where n is the refractive index of the medium of propagation which for most materials at this wavelength range is close to unity, λ is the wavelength of the incident radiation (46.9nm) [42] and Φ is the difference in angle ϕ, where rays cross the optic axis for the marginal and paraxial rays,

$$\Phi = \phi_{ma} - \phi_p. \tag{4.10}$$

The diffraction limit for an on-axis spherical mirror, at a distance U=1.5m from the source at beam heights of $Y_i = 4.5$mm and $Y_i = 2.5$mm is shown in Figure 4.7. The focal spot becomes diffraction limited for mirrors of radius of curvature over 130mm at wavelength 46.9nm as the circle of least confusion is smaller than the diffraction limit (Figure 4.7). Therefore mirrors with radius of curvature of 100mm or 150mm can be used as both will give focused spot sizes of approximately 2μm.

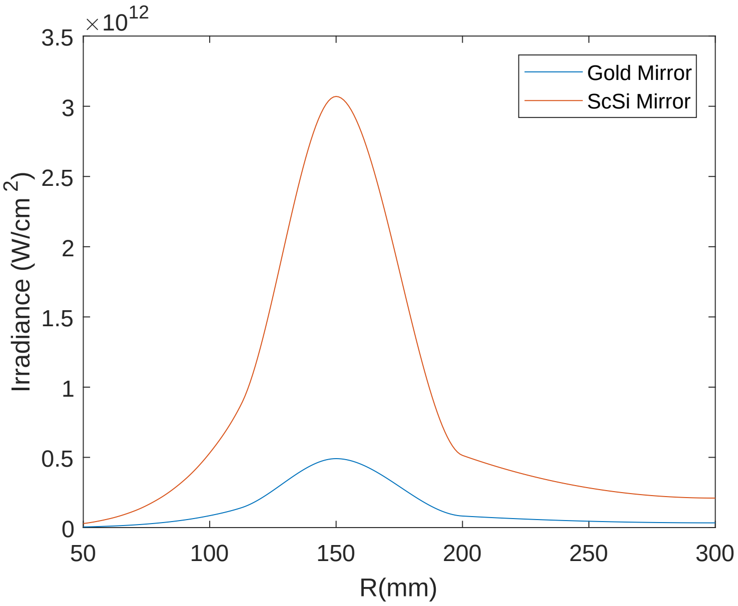

Figure 4.8: Irradiance of the diffraction limited focal spot produced by Sc/Si multilayers and gold mirrors of varying radius of curvature (R) assuming laser beam intensity extends uniformly from the optic axis between Y_i of 2.5 and 4.5 mm and is zero elsewhere

4.3.2 Focused Intensities

With a knowledge of the capillary discharge laser beam energy and pulse duration we can estimate the focused irradiance of the EUV laser. The laser has an average energy output of approximately $50\mu J$. The reflectivity of the Sc/Si mirrors (Chapter 3) is approximately 50% so we have a total energy on target of $25\mu J$. Assuming the pulse duration of the laser is t=1.5ns, the average irradiance is calculated using

$$I(Wcm^{-2}) = \frac{E}{\pi |r_{clc}|^2 t} \tag{4.11}$$

where r_{clc} is the radius of the circle of least confusion [40]. Using the circle of least confusion data from Figure 4.6 and the information on the diffraction limit for each mirror, it is possible to calculate the focused irradiance of the laser over a range of values for the radius of curvature R of the mirror.

Figure 4.8 shows that the irradiance peaks for a 100mm radius of curvature scandium silicon mirror at a value of 3×10^{12}W/cm^2 and for the same mirror in gold (reflectivity 8% [48]) the peak is at 100mm radius of curvature with an irradiance of 5×10^{11}W/cm^2.

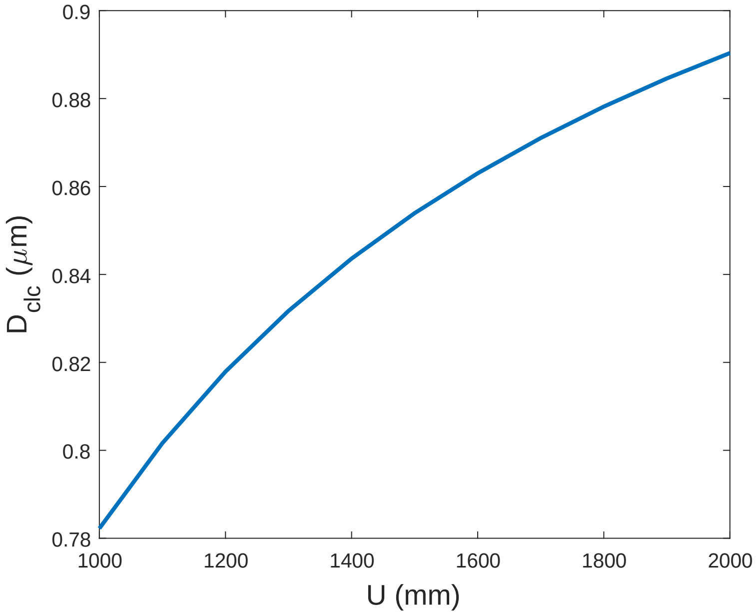

Figure 4.9: The diameter of the circle of least confusion as a function of the position U of the source along the optic axis.

4.3.3 Alignment

Any experimental set up will have focusing errors associated with the alignment of optics. As demonstrated in Chapter 3 the position of the mirror relative to the optic axis causes different types of aberrations. In order to minimise these the limits of the offset in the mirror position (i)along the optic axis, z, (ii)perpendicular to the optic axis (x or y for a cylindrically symmetric system) and rotationally needs to be investigated.

Deviations from an on axis position are modelled in a 2D CAD ray tracing programme, where investigations are carried out with a spherical mirror with radius of curvature 100mm. This mirror radius was chosen as with a diffraction limit of 9.3×10^{-7}m and a circle of least confusion of 7×10^{-7}m it has the smallest diffraction limit (Figure 4.7) and has the highest possible irradiance (Figure 4.8).

Movement of the spherical mirror along the optic axis (z-direction) can be analysed by changing the value of U in (Equation (4.4)-Equation (4.8)), in order to gauge the effect of a fixed focus movement of the mirror along the optic axis. However, the position of the focus will also change. As the distance of the mirror from the centre point changes the points at which the paraxial and marginal rays cross the optic axis, V (Equation (4.6)) also changes.

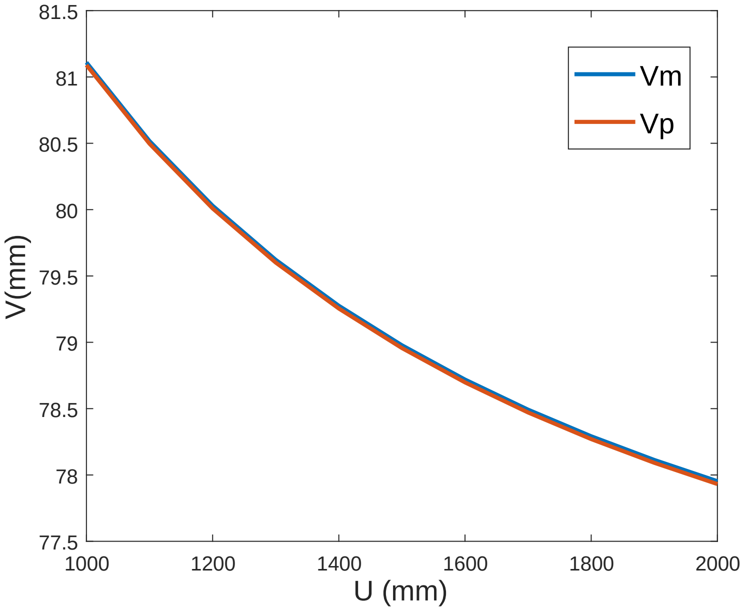

Figure 4.10: The distance V along the optic axis where rays cross the axis as a function of position U of the source for a spherical mirror. Two rays interacting with the mirror at heights of 2.5mm (V_p) and 4.5mm (V_m) are shown.

This indicates that the target must also be out of position in order to satisfy Equation (4.2), where U is the object distance and V is the image distance.

Moving the mirror in the z-direction will have little effect on the aberrations. Figure 4.9 shows that a total off-set of 1m in the z-direction will change the diameter of the circle of least confusion by approximately 100nm. However moving the mirror by 1m in the z-direction it will change the focus position by approximately 3mm.

Displacement of the spherical mirror in a direction perpendicular to the optic axis causes the focus to move off the optic axis, and may cause other aberrational effects such as coma or astigmatism which change the shape of the focal spot (Chapter 3). As the displacement in the y-direction (Δy) increases, the diameter of the circle of least confusion also increases. The aberrations are larger than the diffraction limit for a displacement greater than 0.2mm (Figure 4.11). The aberrations are much more sensitive than displacement in the z-direction.

Rotational displacement here refers to the mirror being rotated about the point where it meets the optic axis. As with displacement in the y-direction, rotational displacement may also cause coma and astigmatism and thus change the shape of the focal spot. The mea-

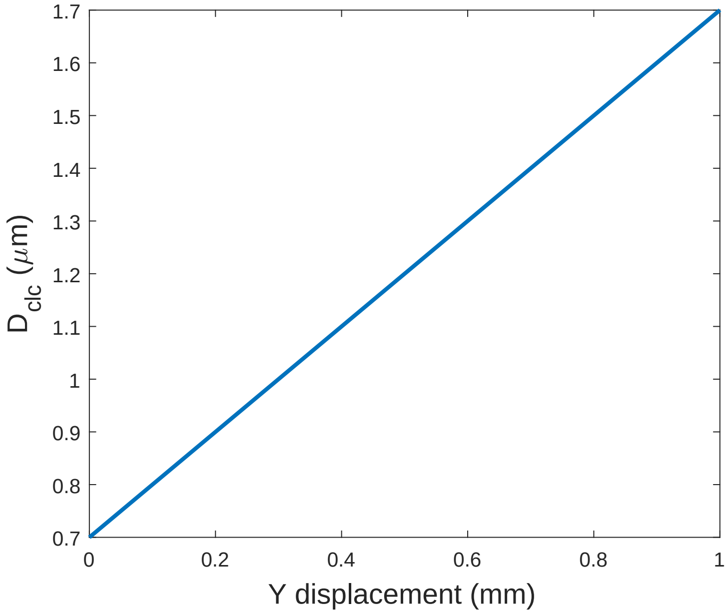

Figure 4.11: The diameter of the circle of least confusion as a function of the position Y of the mirror centre from the optic axis. Other parameters are as for Figure 4.10.

surements of the diameter of the circle of least confusion are shown in Figure 4.12, where the diameter of the circle of lest confusion is larger than the diffraction limit for a rotation of $\theta = 3$mrad. This again is much more sensitive to displacements than the z-direction due to the effects of coma and astigmatism on the focus.

4.4 Parabolic and Elliptical Mirrors

The issues presented in Section 4.2 can be overcome by using parabolic or elliptical mirrors. These allow for off-axis focusing and reduce the aberrations seen in Figure 4.4. A parabola is defined as,

$$y = Ax^2, \tag{4.12}$$

which gives a a symmetrical open plane curve formed by the intersection of a cone with a plane parallel to its side. A parabola will have two points of focus, one at a positive distance, x (real focus) from the central point and one at -x (virtual focus). The focal length for constant A is then given by,

$$f = \pm\frac{1}{4A} \tag{4.13}$$

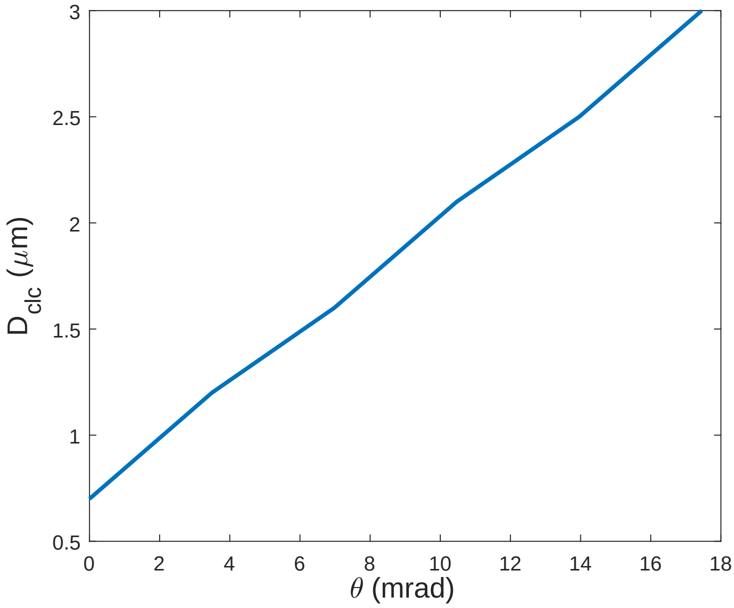

Figure 4.12: The diameter of the circle of least confusion as a function of the angle of mirror to the optic axis. Other parameters are as for Figure 4.10

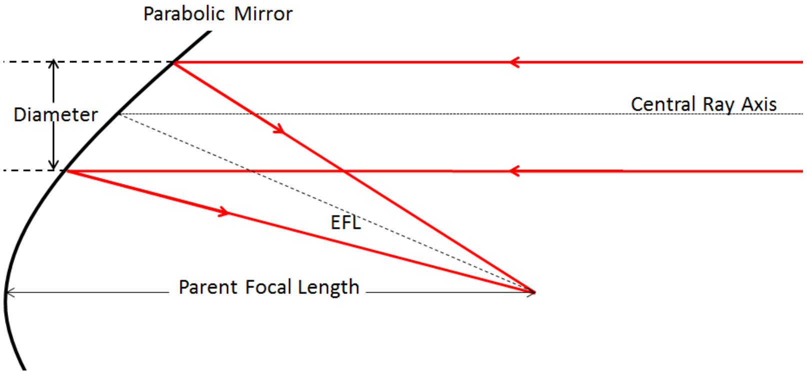

Figure 4.13: Parabolic mirror focusing incident radiation at the effective focal length (EFL)

assuming all incident rays are perfectly parallel to the axis.

A full parabolic mirror will focus a collimated beam at its focal point, similar to the focusing set-up used in Chapter 7. However, this is not always the desired outcome as the single surface parabola will intercept and block the incoming laser beam. Using just the edge of the parabolic mirror is possible and focuses the radiation slightly off axis (Figure 4.13).

Parabolic mirrors can only achieve a diffraction limited image when focusing a perfectly collimated beam at normal incidence at the parent focal point [57]. As can be seen in Figure 5.4 the beam produced by the capillary discharge laser is not collimated but has

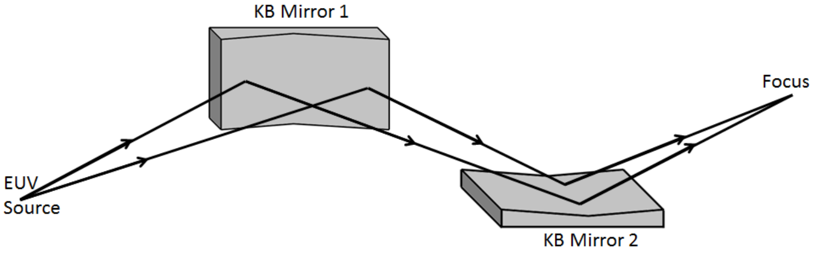

Figure 4.14: Kirkpatrick-Baez mirror system, rays are focused in the horizontal plane by the first mirror and in the vertical plane by the second mirror, cancelling out any astigmatism and producing a diffraction limited focal spot

a divergence of approximately 4.5mrad. This will cause coma and spherical aberrations, increasing focal spot size and decreasing focused irradiance.

4.5 Kirkpatrick-Baez Mirrors

EUV radiation can be reflected using grazing incidence techniques. The most effective of these techniques is the Kirkpatrick-Baez Mirror (KB mirror), which consists of two spherical mirrors placed orthogonally to each other at grazing incidence. The first mirror focuses in the horizontal plane and the second mirror focuses in the vertical plane. The result is a real image focused according to a point determined by the radius of curvature of the mirrors [58].

The two mirror system allows for astigmatisms (Chapter 3) to be cancelled out by the second mirror. Although this is an effective method for focusing EUV radiation with a high reflectivity which produces a diffraction limited focus, the grazing incidence means the whole beam profile may not be reflected by the mirrors. This causes a major reduction in the efficiency of the mirror system leading to a decrease in the focused intensity of the radiation. Kirkpatrick-Baez Mirrors could be made large enough so that the beam is not clipped, this is not a possibility for this experiment due to limited space in the experimental vacuum chamber.

4.6 Wolter Optics

Wolter optics are grazing incident mirrors usually used in telescopes. They consist of two conic surface at grazing incidence in order to satisfy the Abbe sine rule

$$\frac{\sin(\theta)}{\sin(\Theta)} = \frac{\sin(\phi)}{\sin(\Phi)}, \tag{4.14}$$

where θ and ϕ are the angles of any two rays as they leave the source, and Θ and Φ are the angles of the same rays at the image. The advantages of using Wolter optics is that they have a large solid angle and a large field of view, making them ideal for telescopes.

There are three different types of Wolter optic (Figure 4.15). Each of these uses slightly different mirror configurations, each with advantages and disadvantages. The most commonly used is type 1 as it is the simplest mechanically and also allows several telescopes to be nested inside each other. An example of a type 1 Wolter telescope is the Chandra X-Ray Observatory. The advantage of using a type 2 Wolter telescope is the higher magnification. This is because the second reflection is off the outside of a surface, which allows longer focal lengths. However, type 2 is much more prone to spherical aberrations therefore type 2 telescopes are generally only used for narrow-field imaging or as the optic for a dispersive spectrometer. The type 3 has never been used in x-ray astronomy but it can still be used as a focusing optic. Unfortunately it is much more mechanically difficult to set-up and is therefore not used.

Having multiple optics all focusing on axis means that coma can be avoided and spherical aberrations can be minimised using the second mirror. They can also reflect light from a larger source than a Kirkpatrick-Baez mirror. However, in this case there are four independent mirrors which will all have some freedom of movement. This makes the alignment process much more difficult than for a one or two mirror system [59].

4.7 Schwarzschild Optics

A Schwarzschild focusing optic consists of a system of two spherical mirrors, one large concave mirror with a hole in the centre and one smaller convex mirror (see Figure 4.16) [38]. Radiation coming from a source passes through the hole in the large mirror to the surface of

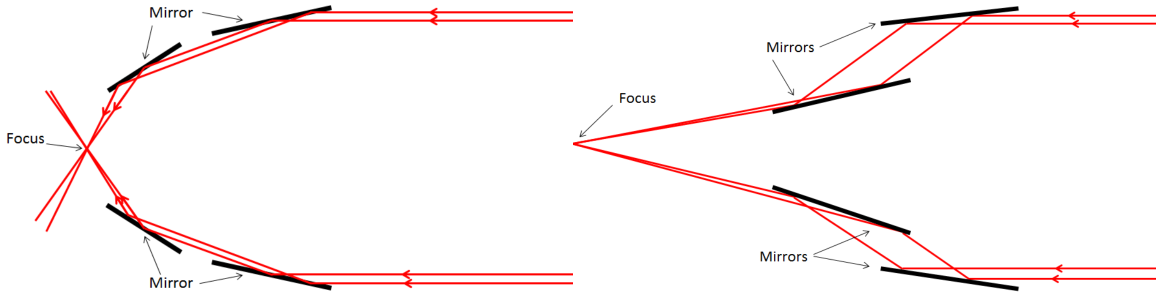

(a) Type 1

(b) Type 2

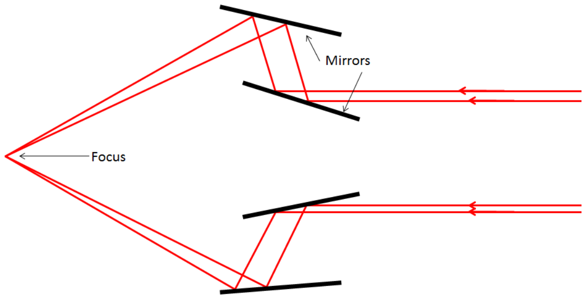

(c) Type 3

Figure 4.15: Type 1, Type 2 and Type 3 Wolter telescope set-ups

the small mirror and is reflected onto to the surface of the large mirror and focused towards a point. The Schwarzschild focusing optic is suitable for focussing of a wide range of wavelengths into the extreme ultra-violet (EUV) if suitable multilayer coatings are used as the reflective layer for the mirror surface. A Schwarzschild has a large aperture enabling higher numerical aperture focusing which minimises the diffracted beam size. Chromatic aberration is eliminated due to the reflection optics, though a multilayer will only reflect a limited wavelength range. The Schwarzschild geometry is particularly suited to ultra-short wavelengths which are absorbed in refracting optics [60]. If the two mirrors are set up correctly in a Schwarzschild focusing optic, third-order optical aberrations can be minimised. The spherical aberrations from the concave and convex mirrors when the correct radius of curvature is used can eliminate each other and can give a near aberration free focus [40, 60].

A Schwarzschild focusing optic is well suited for use with the beam profile produced by a capillary discharge laser. The centre on axis component of a beam is lost in a Schwarzschild focusing optic due to the reflection off the centre of the primary mirror back through the hole in the secondary mirror. As capillary discharge lasers have an annular beam profile, there is little laser light to lose from reflections off the primary mirror and the majority of the beam

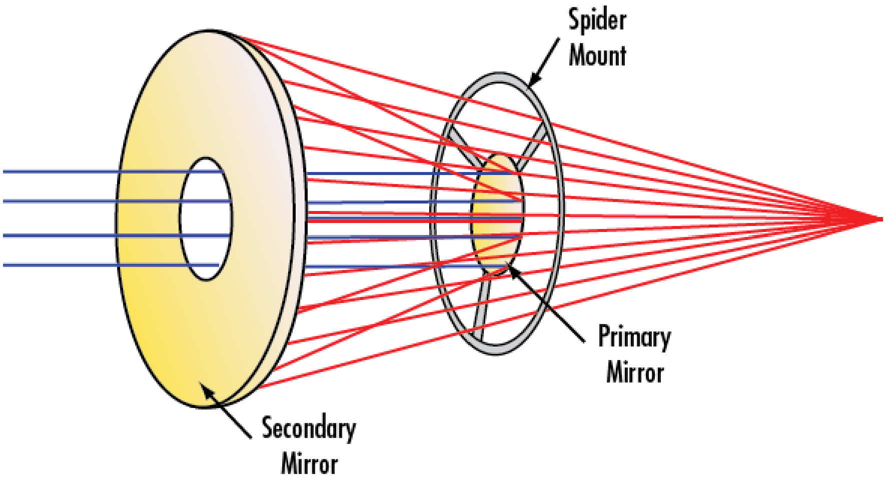

Figure 4.16: A schematic of the geometry of a basic Schwarzschild focusing optic (Taken from [61])

is kept and can be used, increasing the overall transmission of the mirror system.

The geometry of a Schwarzschild focusing optic is shown in Figure 4.17. This shows a ray from a source at distance (U) travelling at angle, δ to the optic axis, reflection off the small inner convex mirror (primary mirror) at angle, θ_1, onto the larger concave mirror (secondary mirror) at angle, θ_2, and the distance (V) at which it crosses the optical axis at angle, ϕ.

The longitudinal spherical aberrations can be calculated by taking the difference between the values for V for two rays incident at different angles, δ, from the optical axis. If the longitudinal aberrations go to zero then the circle of least confusion (CLC) and transverse aberrations will also be minimised.

Assuming the radius of curvature of the primary and secondary mirror are R_1 and R_2 respectively, the rays are incident on the mirrors at angles θ_1 and θ_2 respectively, we have

$$R_1 \sin(\theta_1) = R_2 \sin(\theta_2) \tag{4.15}$$

The angle δ at which the ray is emitted from the point source is,

$$\tan(\delta) = \frac{Y_i}{U - \sqrt{(R_1^2 - Y_i^2)}} \tag{4.16}$$

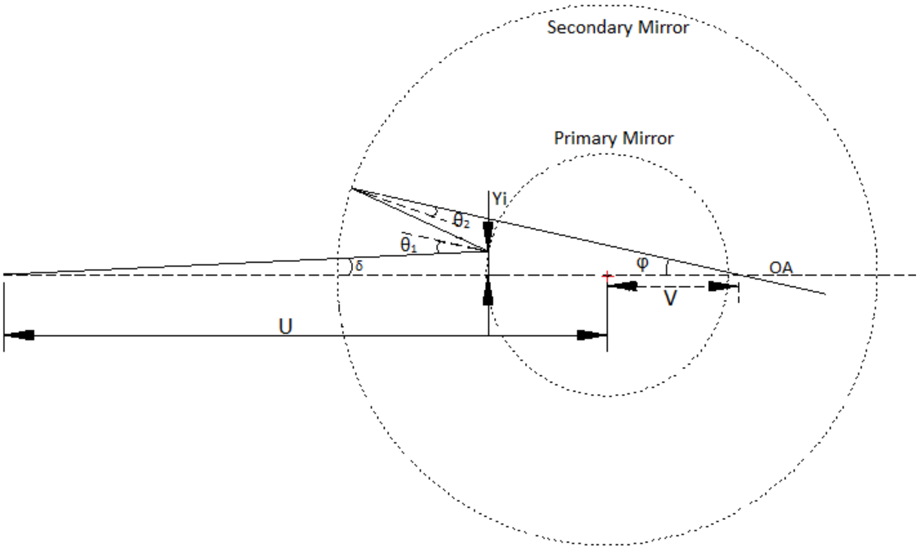

Figure 4.17: The geometry of a Schwarzschild focusing set-up showing a point source at distance U from the optical centre and angle δ from the optical axis, reflections off primary at height Y_i and angle θ_1 and refection off a secondary mirror at angle θ_2. The focus is measured at distance V from the optical centre and angle ϕ from the optical axis.

where Y_i is the height at which the ray strikes the mirror and chosen based on the beam divergence and source distance U.

From this the incident angle on the mirrors can be calculated,

$$\theta_1 = \sin^{-1}\left(\frac{Y_i}{R1}\right) + \delta \tag{4.17}$$

and

$$\theta_2 = \sin^{-1}\left(\frac{R_1 \sin(\pi - \theta_1)}{R_2}\right) \tag{4.18}$$

It is then possible to express ϕ in terms of the ratio of the radius of curvature of the two mirrors, where $r = \frac{R_2}{R_1}$, and the distance U,

$$\phi = 2\left[\sin^{-1}\left(\frac{U}{R_1}\sin(\delta)\right) - \sin^{-1}\left(\frac{U}{R_1}\frac{1}{r}\sin(\delta)\right)\right] - \delta \tag{4.19}$$

This is used to calculate, V, the distance from the centre of the optical system to the

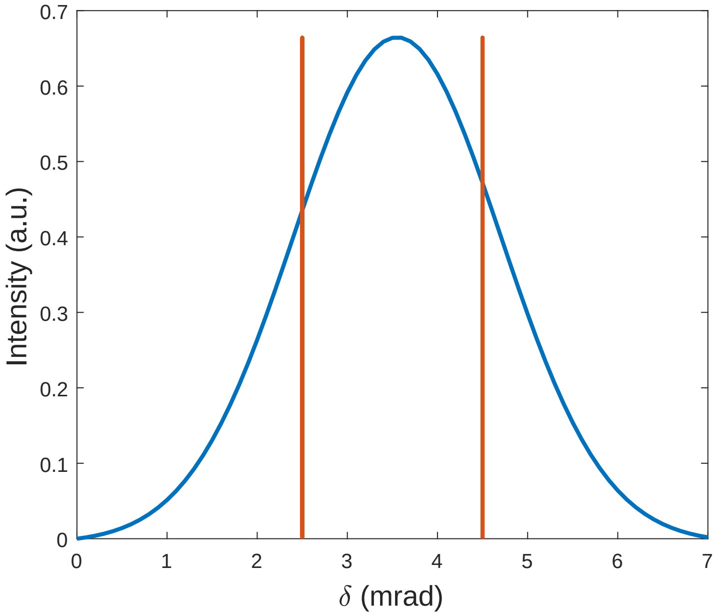

Figure 4.18: Fit of an EUV laser beam profile from a capillary discharge laser showing an intensity peak at a beam divergence of 3.5mrad (measurements from [62]). The range reflected by our Schwarzschild design is indicated by the red lines

focus,

$$V = \frac{U\sin(\delta)}{\sin(\phi)} \tag{4.20}$$

Repeating this for two values of Y_i for the Paraxial and marginal rays the longitudinal aberrations (L_A) can be calculated using,

$$L_A = V_{paraxial} - V_{marginal} \tag{4.21}$$

The spherical aberrations for the Schwarzschild focusing system to be used with the 46.9nm capillary discharge laser can now be calculated using Equations (4.16) to (4.21) from above.

The values for Y_i for the paraxial and marginal rays are chosen based on the beam divergence at distance U from the source. U is determined by the space available in the vacuum chamber, which in this case is 1.5m. At 1.5m the beam divergence gives Y_i for the paraxial and marginal rays as 2.5mm and 4.5mm respectively.

The radius of curvature of the primary mirror (R_1) again needs to be determined taking

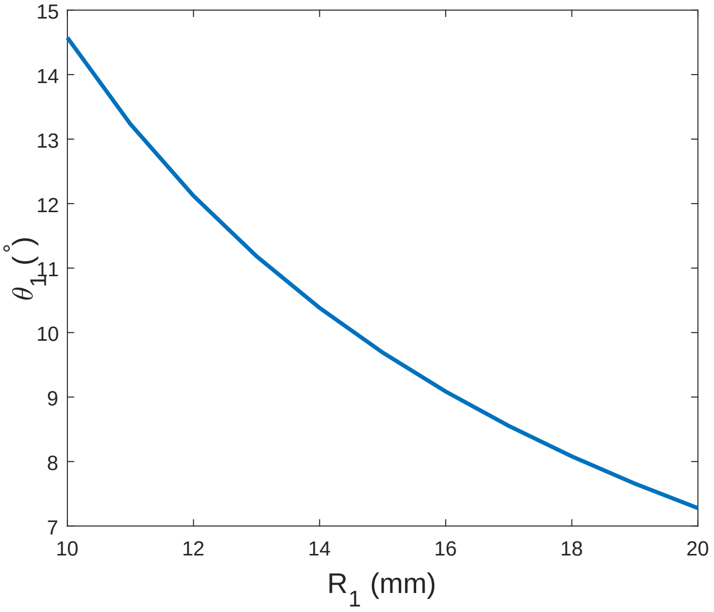

Figure 4.19: The incident angle at the primary mirror (θ_1) as a function of the radius of curvature of the primary mirror (R_1) assuming a distance of U=1.5m from source.

into account the reflectivity of the Sc/Si multilayer mirrors (Section 3.5). Using the IMD software to model the optical properties of multilayer films, reflectivities of scandium silicon multilayer mirrors have been calculated over a range of angles from 0° to 45° as shown in Figure 3.15. The simulations show that for angle of incidences less than 10° the reflectivity of the mirrors is approximately constant, but we know that the reflectivity of the multilayer drops off with increasing incident angle above 20°.

Figure 4.19 shows how the angle of incidence onto the first mirror, θ_1, changes with changing the radius of curvature of the mirror. In order to keep the first multilayer mirror reflectivity high the radius of curvature of the primary mirror was chosen to be 16mm, which implies a maximum $\theta_1 = 9°$. This was also chosen to allow for geometrical purposes, if the radius of curvature of the first mirror is too large it will intercept the rays reflected off the secondary mirror.

Equations (4.16) to (4.21) can be used to calculate the longitudinal aberrations with our chosen parameters for U, R_1 and the known divergence range, δ from the capillary discharge laser source. Figure 4.20 shows the values for the longitudinal aberrations as a function of the second mirror radius of curvature, R_2, for a Schwarzschild system with U=1.5m, Y_i=2.5mm and 4.5mm and R_1 = 16mm. The longitudinal aberrations are zero at $R_2 \approx 42$.

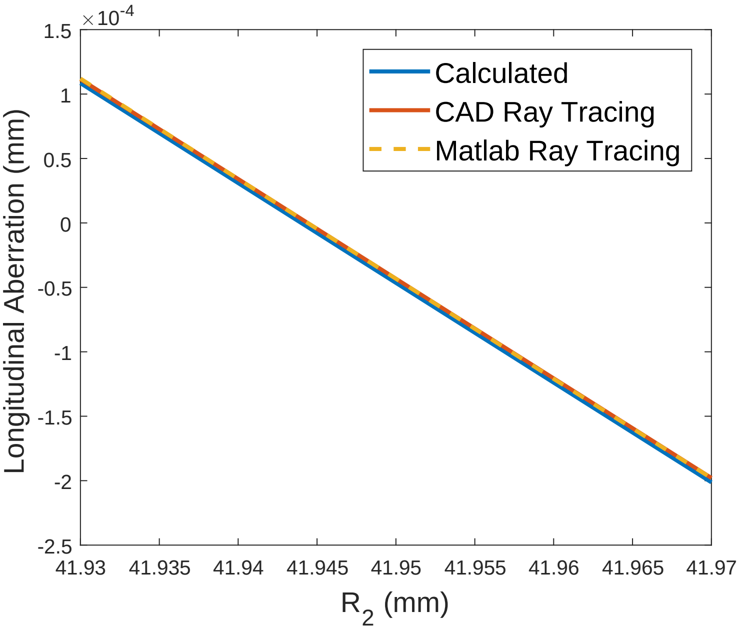

Figure 4.20: Longitudinal aberrations as a function fo the radius of curvature of the secondary mirror (R_2) for calculated values (blue), CAD ray tracing (red) and a Matlab ray trace (yellow), where U=1.5m, Y_i=2.5mm and 4.5mm and R_1 = 16mm. It is assumed that the laser output intensity is constant at the first Schwarzchild mirror for distances from the optic axis between 2.5 and 4.5 mm and zero at any other distance.

The above analysis agrees with research by Artyukov, [63], which suggests that the ratio of the radius of curvature of the two mirrors, $\frac{R_2}{R_1} = r$ should fit the inequality,

$$\frac{3+\sqrt{5}}{2} \leq r \leq 4 \tag{4.22}$$

Calculated optimum values give $r = 2.6$ which fits well within this range.

To confirm the results obtained with aberrations geometry, ray tracing of the experimental set-up was undertaken. A 2D CAD modelling programme (libre CAD) has been used for ray tracing to measure longitudinal aberrations superimposed on Figure 4.20 and shows identical results to our geometrical calculations. The results for the longitudinal aberrations from another code are also superimposed on Figure 4.20, obtained from a code written in Matlab which calculates the point at which the incident rays strike the mirrors and uses unit vectors to calculate the point at which the marginal and paraxial rays cross the optic axis. The longitudinal aberrations calculated in this way are identical to our geometrical calculations and ray tracing in CAD.

If a Schwarzschild with U=1.5m, R_1 = 16mm and R_2=42mm then Y_i = 2.5mm and 4.5mm rays focus identically and the focal spot diameter is dominated by diffraction effects. We assume that all aberrations are eliminated and that the phase of the light as a function of the focused angle (Φ) to the optic axis at a distance R from the focus is constant. Light incident at a distance (y) from the optic axis will have a phase difference of, $2\pi y\sin(\Phi/\lambda)$ relative to light focused on axis (y=0).

The electric field at y, E(y), is found by integrating over the spherical surface R using the Fresnel-Kirchhoff diffraction equations we get,

$$E(y) = \int_{area} E(\phi)\frac{e^{i2\pi y\sin\Phi/\lambda}}{R}\Big(\frac{1+\cos\Phi}{2}\Big)dA \tag{4.23}$$

where $E(\phi)$ is the electric field amplitude per unit angle at distance R. For radiation from a sphere onto a plane normal to the optic axis, the area dA will vary with angle so that $dA = 2\pi R\sin\Phi R d\Phi$ and Equation (4.23) becomes,

$$E(y) = \int_{\Phi_{low}}^{\Phi_{high}} E(\phi)\frac{e^{i2\pi y\sin\Phi/\lambda}}{R}\Big(\frac{1+\cos\Phi}{2}\Big)2\pi R\sin\Phi R d\Phi \tag{4.24}$$

The electric field variation on the surface of a sphere of radius R in direction of increasing angle Φ is labelled $E_\Phi(x)$ so $E_\Phi = E_\Phi(x)dx/d\Phi = RE_\Phi(x)$. We assume that the radiation outside the range Φ_{low} to Φ_{high} is zero and that radiation in the range Φ_{low} to Φ_{high} is constant,

$$E(y) = 2\pi E_\Phi(x)\int_{\Phi_{low}}^{\Phi_{high}} e^{i2\pi y\sin\Phi/\lambda}\Big(\frac{1+\cos\Phi}{2}\Big)\sin\Phi d\Phi, \tag{4.25}$$

in the small angle limit this becomes,

$$E(y) = 2\pi E_\Phi(x)\int_{\Phi_{low}}^{\Phi_{high}} e^{i2\pi y\Phi/\lambda}\Phi d\Phi. \tag{4.26}$$

From Abbe's criterion we can estimate the half-width half maximum using,

$$\Delta y = \frac{0.5\lambda}{\Phi_{high} - \Phi_{low}} \tag{4.27}$$

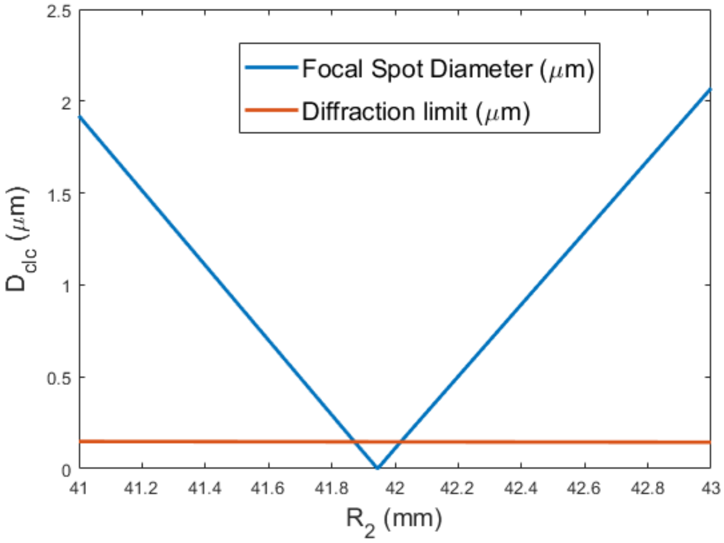

Figure 4.21: Circle of least confusion (blue) and the diffraction limit (red) as a function fo the radius of curvature of the secondary mirror (R_2), where U=1.5m, Y_i=2.5mm and 4.5mm and $R_1 = 16$mm. It is assumed that the laser output intensity is constant at the first Schwarzchild mirror for distances from the optic axis between 2.5 and 4.5 mm and zero at any other distance.

Using Abbe's criterion to estimate the diffraction limit of the Schwarzschild focusing system, and comparing to the values for the circle of least confusion as measured by the CAD ray tracing we get Figure 4.21, where within the range $41.87 \leq R_2 \leq 42.02$ where R_2 is the radius of curvature of the second mirror (R_2) the focus will be diffraction limited at 146nm.

With a knowledge of the capillary discharge laser beam energy and pulse duration we can estimate the focused irradiance of the EUV laser using a Schwarzschild focusing optic. We know the laser has an average energy output of approximately $50\mu J$, however from Figure 4.18 we know that only 50% of this is reflected by the Schwarzschild optic. Assuming the reflectivity of the primary and secondary mirrors are approximately 54% and 55% respectively we have a total energy on target of $7\mu J$. Assuming the pulse duration of the laser is t=1.5ns, the average irradiance is calculated using

$$I(Wcm^{-2}) = \frac{E}{\pi |r_{clc}|^2 t}, \tag{4.28}$$

where r_{clc} is the radius of the focal spot.

Using the data from Figure 4.21 where the diffraction limit is compared to the circle of

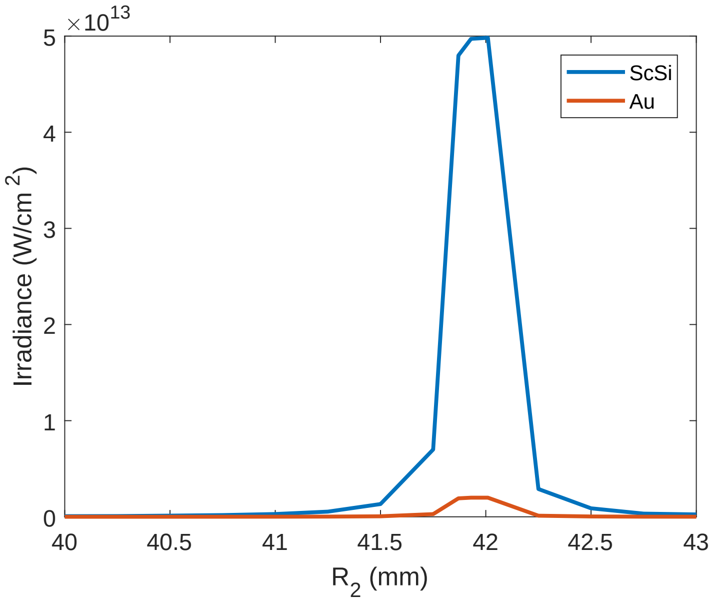

Figure 4.22: The irradiance of a Schwarzschild optic for Scandium Silicon multilayer mirrors (blue) and Gold mirrors (red) where U=1.5m, Y_i=2.5mm and 4.5mm and R_1=16mm over a range of values of R_2. It is assumed that the laser output intensity is constant at the first Schwarzschild mirror for distances from the optic axis between 2.5 and 4.5 mm and zero at any other distance.

least confusion it is possible to calculate the focused irradiance of the laser over a range of values for R_2. All values of R_2 within range give diffraction limited focal spots with a diameter of d=146nm. From this the irradiance of the capillary discharge laser focused using a Schwarzschild optic which uses Sc/Si multilayer mirrors will be $5 \times 10^{13}\mathrm{W/cm}^2$ and for a Schwarzschild optic using gold mirrors the irradiance will be $2 \times 10^{12}\mathrm{W/cm}^2$.

An irradiance curve has been produced in Figure 4.22, where the irradiance is calculated using the circle of least confusion radius for all values outside of the diffraction limit range. Figure 4.22, confirms that as the focus spot size decreases the irradiance will increase until it reaches the diffraction limit.

With two mirrors requiring alignment in the Schwarzschild geometry position, errors are critical. Assuming the small mirror of radius of curvature R_1 is fixed in space we can consider errors in positioning the second mirror of radius of curvature R_2.

Ray tracing has been performed to investigate the effect of he centre of the radius of curvature being (i) at an incorrect position along the optic axis and (ii) at an incorrect position perpendicular to the optic axis (Figure 4.9 and Figure 4.24)

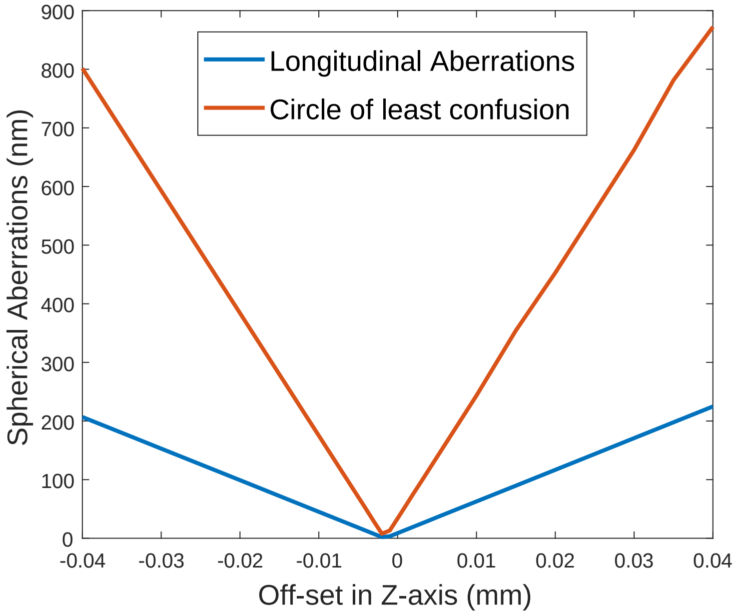

Figure 4.23: Spherical aberrations which occur when the secondary mirror is off-set in the z-axis, with U=1.5m, Y_i=2.5mm and 4.5mm and R_1=16mm and R_2=41.94mm. At z=0 the secondary mirror is placed at 41.94mm from the centre point. The negative movement indicates moving the mirror away from the centre point of the mirrors radius of curvature and positive z shows moving the mirror towards the centre point.

For this investigation U=1.5m, Y_i=2.5mm and 4.5mm and R_1=16mm and R_2=41.94mm, R_2 was then moved along the z-axis and the circle of least confusion and longitudinal aberrations for each position were recorded. Figure 4.9, shows the spherical aberrations as a function of distance from optimal position (z=0). It was expected that the results would show a minimum in spherical aberrations at z=0, however this is not the case. There is a slight offset, with the minimum aberrations occurring at $z = -2\mu$m which indicates that the best focus is achieved at -2μm (towards the laser aperture).

From Figure 4.23 the focus remained on axis and kept the same shape but changed in size. The spherical aberrations should remain smaller than the diffraction limit within the range $-30\mu\text{m} <\leq z \leq 30\mu$m where, the circle of least confusion $\leq$ 150nm.

The investigation into the axis perpendicular to the optical axis (the y-axis). The further from Y=0 the larger the aberrations become. From Figure 4.24, the spherical aberrations should remain smaller than the diffraction limit within the range $0\mu\text{m} <\leq Y \leq 7.0\mu$m where, the circle of least confusion is less than 150nm.

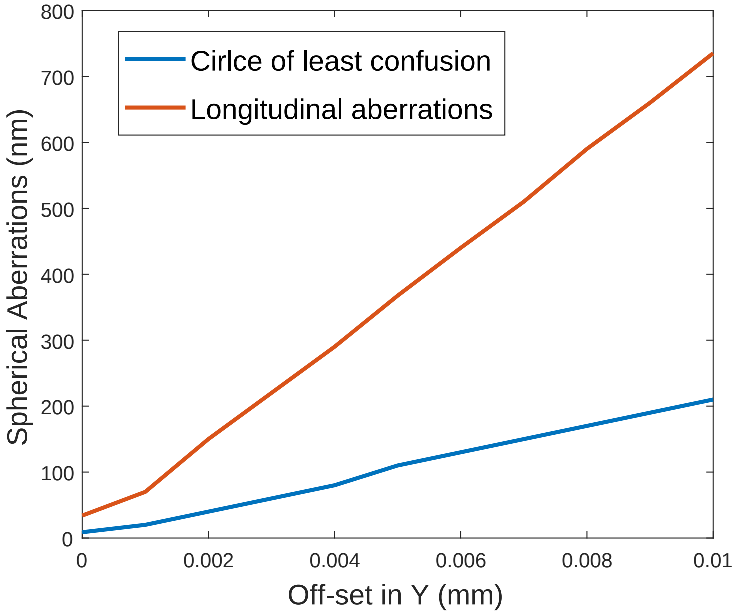

Figure 4.24: Spherical aberrations which occur when the secondary mirror is off-set in the Y-axis, with U=1.5m, Y_i=2.5mm and 4.5mm and R_1=16mm and R_2=41.94mm. At Y=0 the secondary mirror is placed on the optical axis.

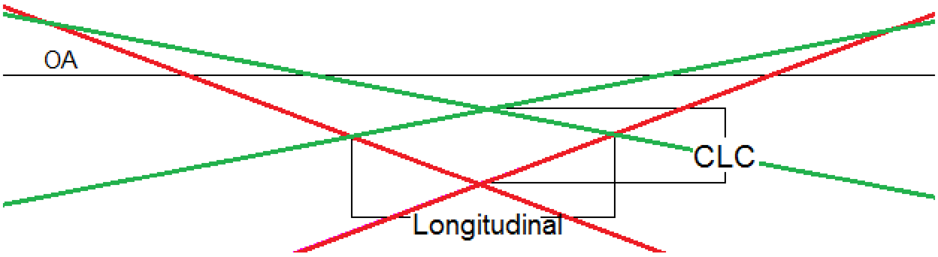

Figure 4.25: Image of the off-set and change in shape of the focus position for Y=+0.01mm showing paraxial (green) and marginal (red) rays. The circle of least confusion (CLC) and longitudinal aberrations (Longitudinal) are labelled.

The offset in the Y-axis also causes the focus position to move and for the shape of the focus to change. For positive values of Y, where the mirror is positioned slightly above the optical axis, the focus is moved below the optical axis and becomes distorted in shape as shown in Figure 4.25. For negative values of Y, the focus occurs above the optical axis and the distortion in shape occurs.

The final possibility of misalignment will be in the form of the secondary mirror being tilted off-axis by some angle, θ (Figure 4.26). The results from this are expected to be similar to the results for the y-scan, where the aberrations are smallest at $\theta = 0$, the focus position is

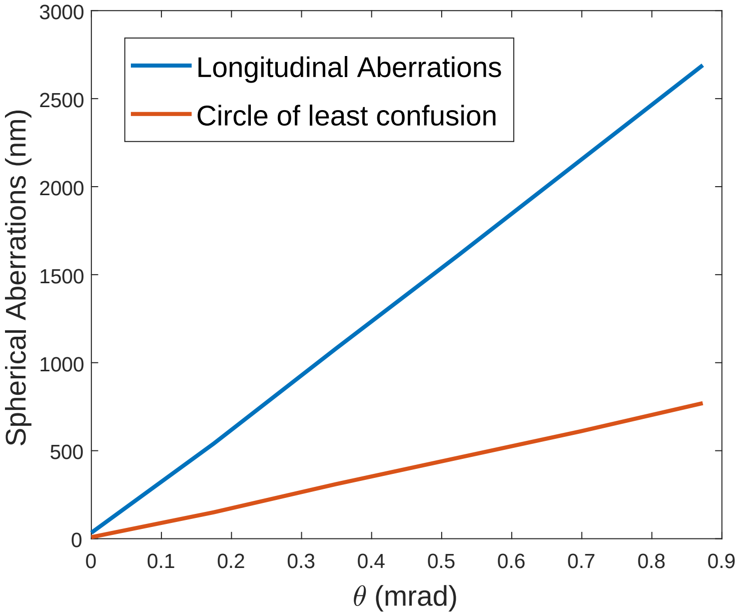

Figure 4.26: The longitudinal aberration and circle of least confusion when the secondary mirror is tilted off-axis by an angle θ, with U=1.5m, Y_i=2.5mm and 4.5mm and R_1=16mm and R_2=41.94mm

moved off-axis and the shape of the focus becomes distorted. Figure shows that this is true, however the effects of the mirror being tilted off-axis causes much worse aberrations than movement in the Z or Y-directions.

A tilt of $\theta = 0.1^o$ gives a circle of least confusion with a diameter of 1.5μm. This is approximately an order of magnitude bigger than the diffraction limit. This means that there is very little room for error in the tilt of the secondary mirror. Clearly the most important factor in aligning the Schwarzschild will be the tilt of the secondary mirror, with there being very little flexibility in the range of movement without causing large spherical aberrations.

It has been shown in this section that a Schwarzchild optic can potentially produce diffraction limited foci with focused irradiances of over 10^{13}W/cm^2. Unfortunately manufacturing lead times meant that it was not possible to perform ablation experiments using a Schwarzschild objective, but simulations have shown that of the methods presented the ablation would give the narrowest and deepest craters.

4.8 Simulations of Focusing Techniques

Some of the irradiances produced by the optics mentioned in Section 4.1 to Section 4.7 have been simulated using a 2D Eulerian radiative-hydrodynamic code POLLUX. POLLUX was written at the University of York and was originally developed to simulate optical and infra-red laser radiation focused into a narrow line or spot which heats a slab or thin film target to create a plasma using a laser irradiance in the range of ($10^9 - 10^{14}$Wcm^{-2}). The hydrodynamic behaviour of the plasma is determined by the laser and target characteristics. POLLUX uses a combination of 2D fluid code modelling with a rapid atomic physics algorithm to simulate EUV interactions with solid targets, the expected energy deposition within the target, the produced plasma parameters and the ablative flow away from the target. The code has been modified in order to represent the EUV laser interaction and includes absorption by photo-ionisation and inverse bremsstrahlung [64, 65].

The hydrodynamic code solves Eulers equations conserving density, momentum and energy in a 2D cylindrical geometry or in a 1D geometry. The 2D axes z and r are formed into a grid which displays the evolution of the plasma over time. The input parameters for POLLUX are based on the characteristics of the incident laser and target including pulse profile (Figure 4.27), power and focal spot size. By altering these variables we can study the effects on the ablation profile of using different incident powers, and focal spot diameters. One dimensional line-outs give data with spatial parameters as shown in Figure 4.28. POLLUX gives the spatial characteristics of the ablation profile at designated time steps throughout the interaction. The POLLUX codes also shows the density profile of the ablation crater, for example Figure 4.30, where the ablation caused by the capillary discharge laser is focused onto a PMMA target.

The focusing methods simulated in POLLUX are assumed to be produced using spherical scandium silicon multilayer mirrors and gold mirrors focused on-axis, Schwarzschild optics or Fresnel Zone Plates (FZP) [66]. The pulse input parameters for each of these methods are shown in Table 4.3. Table 4.3 shows us that the irradiance for a FZP is much lower than for the gold or Sc/Si mirrors despite the similar focal spot size. The Schwarzschild optic has a much lower power on the target as the laser is being reflected by two mirrors, however the diffraction limit is much smaller for a Schwarzschild giving a smaller focal spot radius and higher irradiance. Simulations were run with these parameters assuming a PMMA target

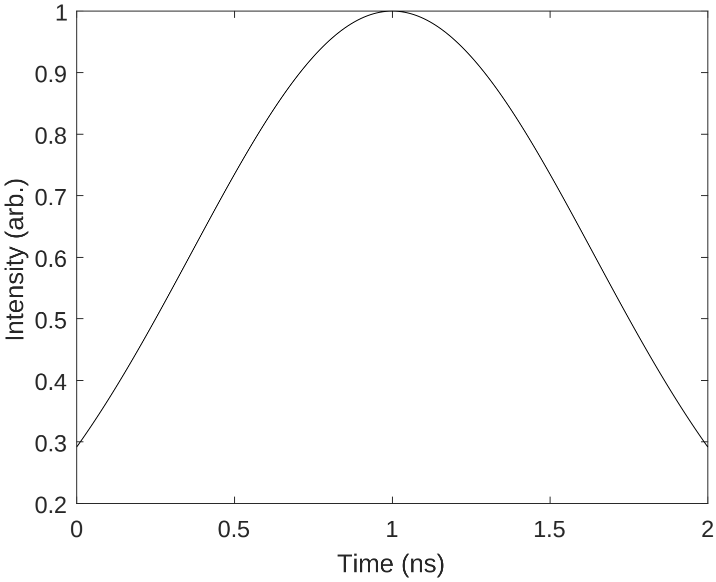

Figure 4.27: Temporal pulse profile input parameters for POLLUX, with $FWHM = 1.5ns$, $t_{rise} = 1ns$ and pulse intensity in arbitrary units.

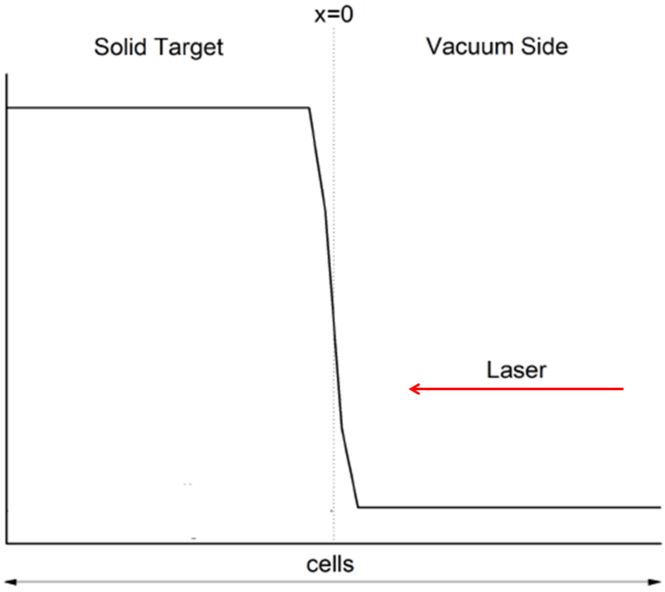

Figure 4.28: 1D POLLUX spatial parameters

Table 4.3: POLLUX input parameters for Sc/Si multilayer mirrors, gold mirrors, fresnel zone plates [65] and Schwarzschild Optics (Chapter 4) all with a pulse duration of t=1.5ns

Focusing Optic	Focal Spot Radius (μm)	Power (erg/s)	Focused Irradiance (W/cm^2)
Sc/Si spherical mirror	0.4	5.3×10^{10}	3.1×10^{12}
Gold spherical mirror	0.4	8.5×10^{9}	4.9×10^{11}
FZP	0.5	5.2×10^{8}	1.0×10^{9}
Sc/Si Schwarzschild	0.073	8.3×10^{10}	4.9×10^{13}

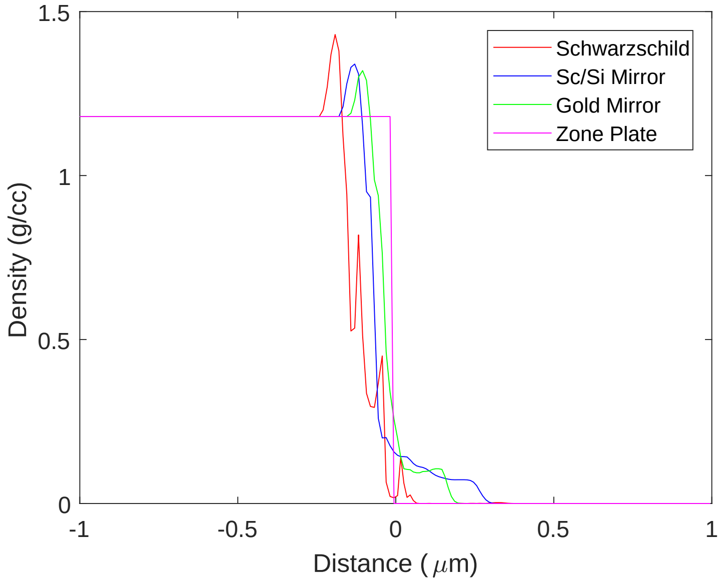

Figure 4.29: 1D Ablation of PMMA target for ScSi Mirrors (I=2.5 × 10^{12}W/cm^2), Gold mirrors (I=3.3×10^{11}W/cm^2), FZP (I=1×10^9W/cm^2) and Schwarzschild (I=5×10^{13}W/cm^2) at t=85ps

(see Figure 4.29).

Figure 4.29 shows, that the Schwarzschild with the highest focused irradiance gives the deepest ablation after a given time. The FZP has such a low irradiance such that after 85ps the pulse has not reached the ablation threshold of the PMMA target and no ablation has occurred. The irregular density peaks seen in the Schwarzschild, Sc/Si mirrors and gold mirrors as the simulation passes the target surface are caused by shock waves (also seen in Figure 4.30). Ablation was measured at 85ps because due to expansion of the plasma in the cells within the code the simulation stopped running for higher intensity simulations.

The 2D profile gives both the depth of the ablation and the width, and can be used to determine which focusing method will give the narrowest ablation. For an incident irradiance of I=2.5 × 10^{12}W/cm^2 for Sc/Si mirrors at t=85ps the depth shown here is the same as in Figure 4.29 at approximately 0.1μm, and the width shown here is approximately 3μm (radius 1.5μm). The Schwarzschild optic shows a much narrower deeper ablation, with a depth of approximately 0.2μm and a width of approximately 1.6μm. This is because of the smaller focal spot radius which not only reduces the diameter of the ablation but increases the irradiance on the target giving both narrower and deeper ablation. The simulation for the gold mirror set-up with incident irradiance of I=3.3 × 10^{11}W/cm^2 at t=85ps shows a similar width to the Sc/Si mirrors of approximately 3μm but a lower depth at approximately 0.07μm.

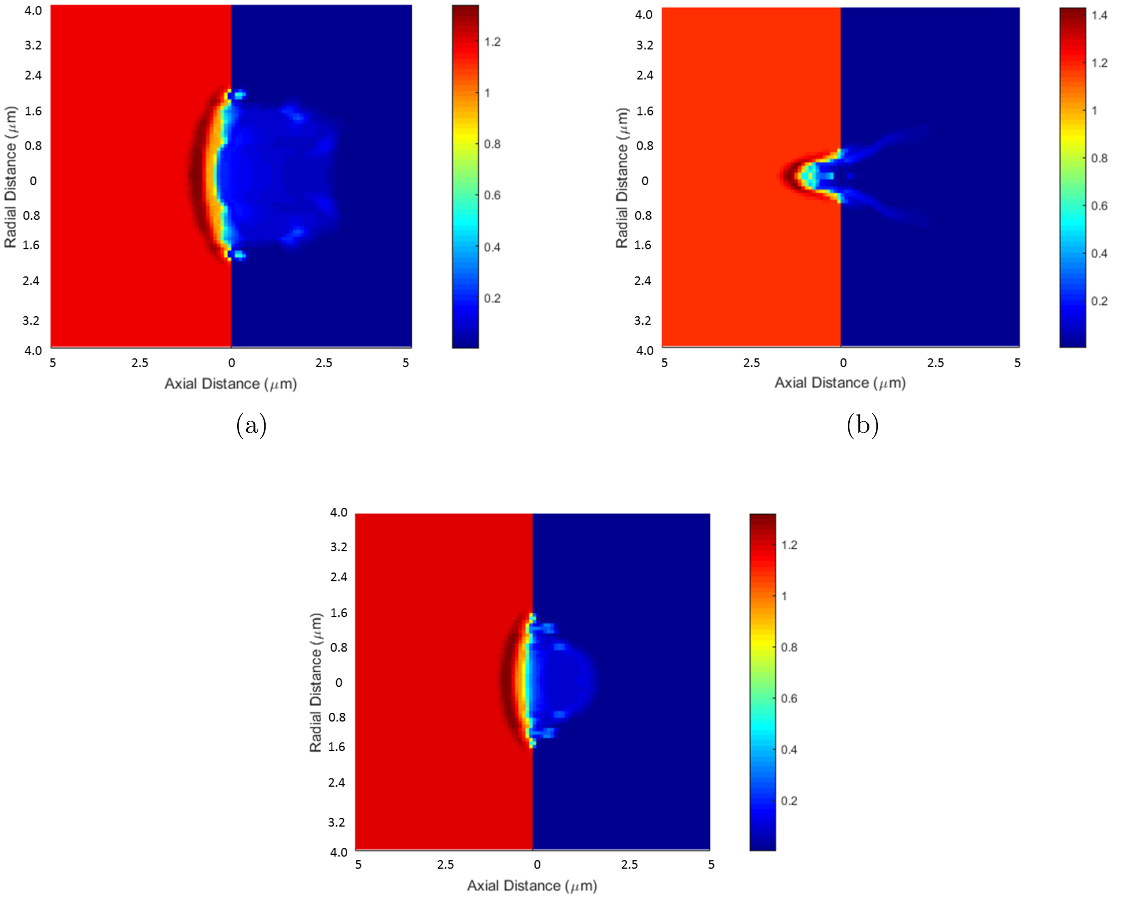

(a) (b)

(c)

Figure 4.30: Ablation profiles for (a) Sc/Sc Mirror, irradiance 2.5×10^{12}W/cm^2 and focal spot radius 0.4μm (b) Schwarzschild, irradiance 5×10^{13}W/cm^2 and focal spot radius 0.073μm (c) gold Mirror, irradiance 3.3×10^{11}W/cm^2 and focal spot radius 0.4μm .

4.9 Conclusions

A number of focusing methods have been reviewed and of these an on-axis spherical mirror will focus the radiation produced by a capillary discharge laser back along the beam path and produce a reasonable focal spot diameter and focused intensity. This is the simplest method of producing a low aberration focus. This method will be experientially tested in later chapters. Focusing can be improved upon by using a Schwarzschild optic. The use of two mirrors allows any spherical aberrations to cancel out and theoretically this will produce a diffraction limited beam. A Schwarzschild optic will produce a much smaller focal spot size and a much higher focused irradiance than that produced by a single spherical mirror.

Chapter 5

Extreme Ultraviolet Capillary Discharge Lasers

Now that The methods of focusing a capillary discharge laser have been established, we must understand how the laser works before an experiment can be run. Capillary discharge lasers have a complex method of producing EUV radiation. Radiation is emitted from a plasma which is formed in the ceramic capillary tube by ionising argon to Ar^{8+} which has neon-like energy levels. This chapter discusses the properties of the plasma produced and how the output radiation and plasma parameters can be measured using multiple different diagnostic techniques.

5.1 Neon-like Argon Lasers

Neon-like ions have closed shells up to principle quantum number n=2. The closed shell structure of their ground state causes neon-like ions to be in high abundance over a wide range of electron temperatures making them particularly useful for the production of laser output [67].

Inelastic electron collisions with ground state neon-like argon ions cause excitation and create the population inversion between excited states of the neon-like ion. Collisional excitation from the $2p^6$ ground state to $2p^5 3p$ states creates a population inversion between $2p^5 3p$ and $2p^5 3s$ states. The $2p^5 3p$ state is metastable to radiative decay back to the ground state,

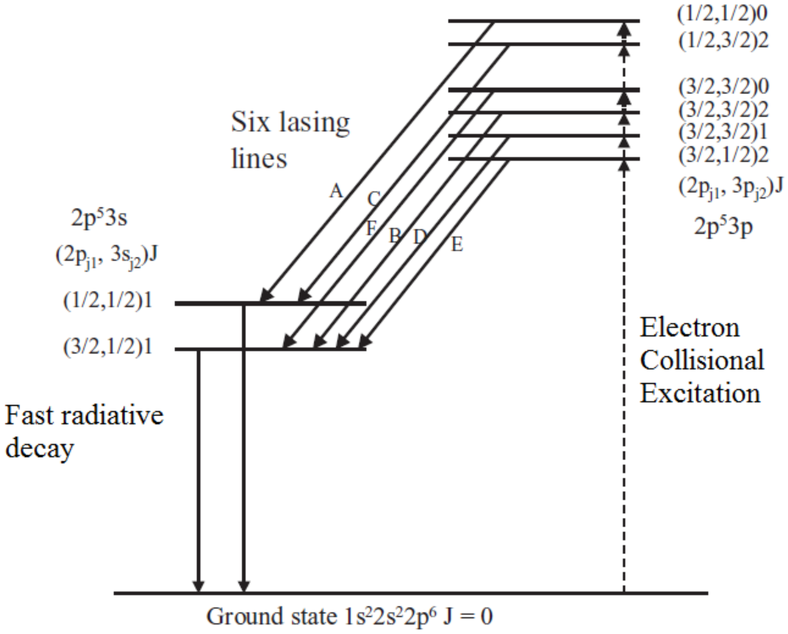

Figure 5.1: Energy level diagram of Neon-like lasers

but can be collisionally excited by so-called collisional monopole excitation (see [37] p221). The lower $2p^5 3s$ laser level rapidly radiatively decays to the ground state. The energy levels of the excited neon-like argon ion are intermediate in coupling between LS and JJ, so the detailed structure of each sub-shell is determined by the j (of individual electrons) and J (for the ion) quantum numbers (see Figure 5.1).

In Neon-like Argon the transition in the J=0-1 line was observed to lase with a wavelength of 46.9nm using a capillary discharge laser. To achieve this a 40kA pulse was used to excite an Argon plasma column in a 3mm diameter capillary up to 21cm in length [68]. The mechanisms to produce lasing in the capillary laser are discussed further in Section 5.1.1.

5.1.1 Laser gain and Saturation

It is not possible to operate the capillary laser with a cavity. The capillary laser has a gain duration of 1- 2 nanoseconds, so only one pass through the 21 cm long gain medium would be feasible in a laser cavity. In addition, as discussed in Chapter 3 mirrors in the EUV have reflectivities of typically 50% and it is particularly difficult to make an output mirror with good transmission and reflectivity. Consequently, the capillary laser uses a single gain pass

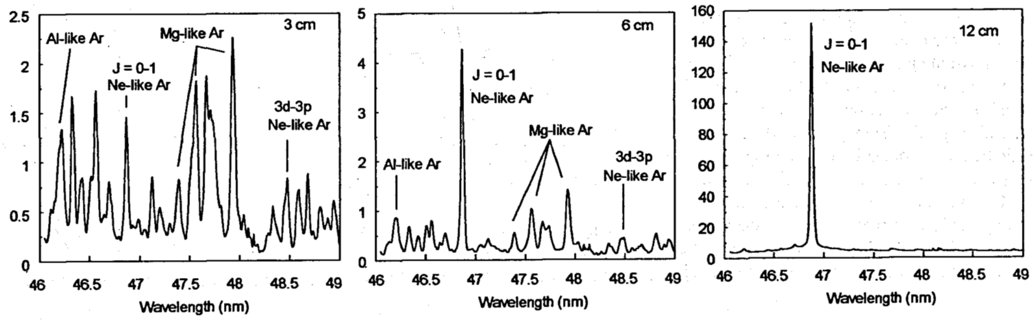

Figure 5.2: Spectra from Ar plasma columns length 3cm, 6cm and 12cm from [71]

to amplify the laser output [69]. The initial photons arise from spontaneous emission and so the laser operates in Amplified Spontaneous Emission (ASE) mode. Based on work by Rocca [70] and Tallents [23], for an ASE, laser the intensity of the laser line increases as a function of plasma length and is given by the Linford forumla,

$$I = I_0(e^{gl} - 1)^{3/2}(gle^{gl})^{-1/2}, \tag{5.1}$$

where l is the plasma length and g is the gain coefficient [70]. Experiments using capillary lasers confirmed the gain in the plasma column by measuring the integrated line intensity as a function of plasma column length (Figure 5.2). In a 3cm long capillary the intensity of the J=0-1 transition at 46.9nm is smaller than surrounding lines (Mg-like Ar, Al-like Ar and 3d-3p Ne-like Ar). Increasing the capillary length to 6cm increases the intensity of the J=0-1 line so it has a significantly higher intensity than the surrounding lines. Increasing the length of the capillary again to 12cm sees the J=0-1 line at 46.9nm becomes dominant and any surrounding lines are insignificant in comparison (Figure 5.2) [71].

The increase in intensity of the J-0-1 line at 46.9nm for longer capillaries has been tested in experiment and simulation by Rocca et al [71]. By solving the radiation transport equation for an homogeneously broadened transition, taking into account line narrowing, refraction effects and gain saturation the laser energy can be calculated as a function of plasma column length. The laser output as a function of length shown in Figure 5.3 demonstrates the laser energy where the laser energy increases exponentially until a plasma column length of 15cm where the energy remains constant at approximately 50μJ [70, 71].

In a typical collisionally excited laser system, gain saturation is reached at $gl \approx 14 - 20$. In

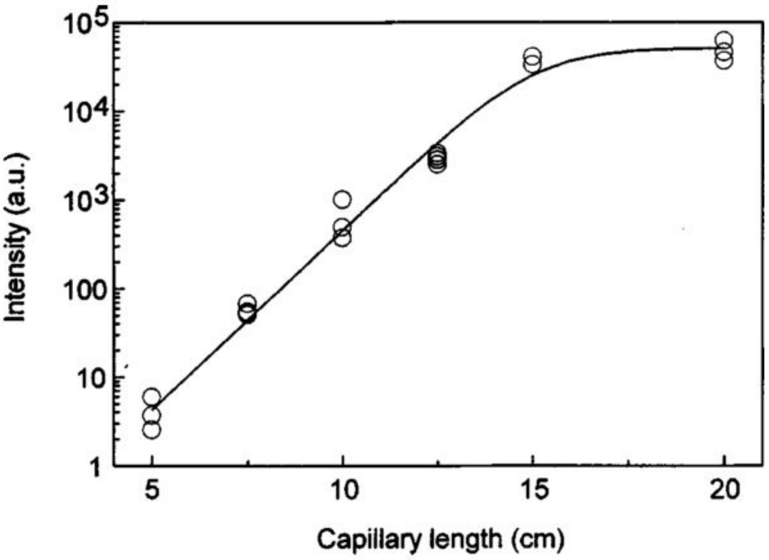

Figure 5.3: Computed (dashed line) and measured (solid line) laser output energies for varying plasma column length from [71]

the argon based capillary discharge laser the line intensity increases with a small signal gain coefficient of $g \approx 0.92\text{cm}^{-1}$ meaning saturation is reached at $l \approx 15\text{cm}$. This is shown in Figure 5.3 where the laser energy increases exponentially with capillary length until 15cm where saturation is achieved. At saturation the gain coefficient is reduced below that of the small signal gain found at short capillary lengths.

The gain coefficient of a laser is given by,

$$g = \sigma(N_2 - N_1\frac{g_2}{g_1}) \tag{5.2}$$

and

$$\sigma = \frac{A_{21}\lambda^2}{8\pi f(\nu)} \tag{5.3}$$

where σ is the stimulated emission cross-section and $N_2 - N_1\frac{g_2}{g_1}$ is the population inversion density obtained from the population N_2 and N_1 and degeneracies g_2 and g_1 of the upper and lower lasing level respectively. The Einstein coefficient for spontaneous emission is A_{21}, λ is the laser wavelength and $f(\nu)$ is the line shape parameter where $f(\nu) \propto \frac{1}{A_{21}}$ at line centre [37].

For a naturally broadened transition the gain coefficient,

$$g \propto N_2\lambda^2. \tag{5.4}$$

The power density required to achieve population density is

$$P = N_2 A_{21}\frac{hc}{\lambda} \propto N_2\lambda^{-3}, \tag{5.5}$$

as along an isoelectronic series $A_{21} \propto \lambda^{-2}$

The power density required to obtain a particular gain coefficient in a naturally broadened transition consequently varies as

$$P \propto \lambda^{-5} \tag{5.6}$$

It is clear that short wavelength λ laers require significantly more pumping power. The scaling shown in Equation (5.6) indicates that high power pumping at the population inversions is required to obtain lasing with the EUV capillary laser.

5.1.2 Refraction

For lasing at short wavelengths it is not sufficient to supply large pumping power. To achieve lasing with a reasonable gain coefficient, Equation (5.4) indicates that high densities N_2 are also required at short wavelengths. However, at high densities, the propagating EUV radiation can refract out of the amplifying region. Changes in refractive index of a plasma column occur due to electron density gradients. The refractive index of a plasma (n) is dependant on the electron density (n_e), such that

$$n = \sqrt{1 - \frac{n_e}{n_c}}, \tag{5.7}$$

where n_c is the critical density [70, 72] given by,

$$n_c = \frac{\epsilon m_e c^2}{e^2 \lambda^2}. \tag{5.8}$$

In a capillary discharge laser plasma column the electron density decreases as a function of distance from the central axis (r). Based on previous work by Rocca [70] we can investigate the effects of refraction, by approximating the electron density decrease from an axis to a linear form. We have

$$n_e(r) = n_e(0)\frac{L - r}{L}, \tag{5.9}$$

where L is the diameter of the plasma column. The refractive index increases with increasing radius r so that the plasma lasing medium acts as a diverging lens. The refraction causes a ray of EUV radiation to change its angle θ to the cylindrical axis as a function of distance z_p down the axis such that,

$$\frac{d\theta}{dz_p} = \frac{n_e(0)}{2n_c L}, \tag{5.10}$$

integrating this gives the angle of the ray to the axis (θ),

$$\theta = \theta(0) + \frac{n_e(0)}{2n_c}\frac{z_p}{L}, \tag{5.11}$$

where $\theta(0)$ is the initial angle of the ray. The radius of the ray at the output can then be calculated by,

$$\frac{r}{L} = \frac{r_0}{L} + \theta(0)\frac{r_0}{L} + \frac{n_e(0)}{4n_c}\left(\frac{r_0}{L}\right)^2, \tag{5.12}$$

where r_0 is the initial radius of the ray.

A ray propagating in such a plasma goes from a region of low refractive index to high refractive index and is bent away from the central axis which is the region of maximum gain. This causes losses and a decrease in the gain and amplification length, reducing the laser output energy. Refraction also effects the spatial distribution of the beam, increasing the

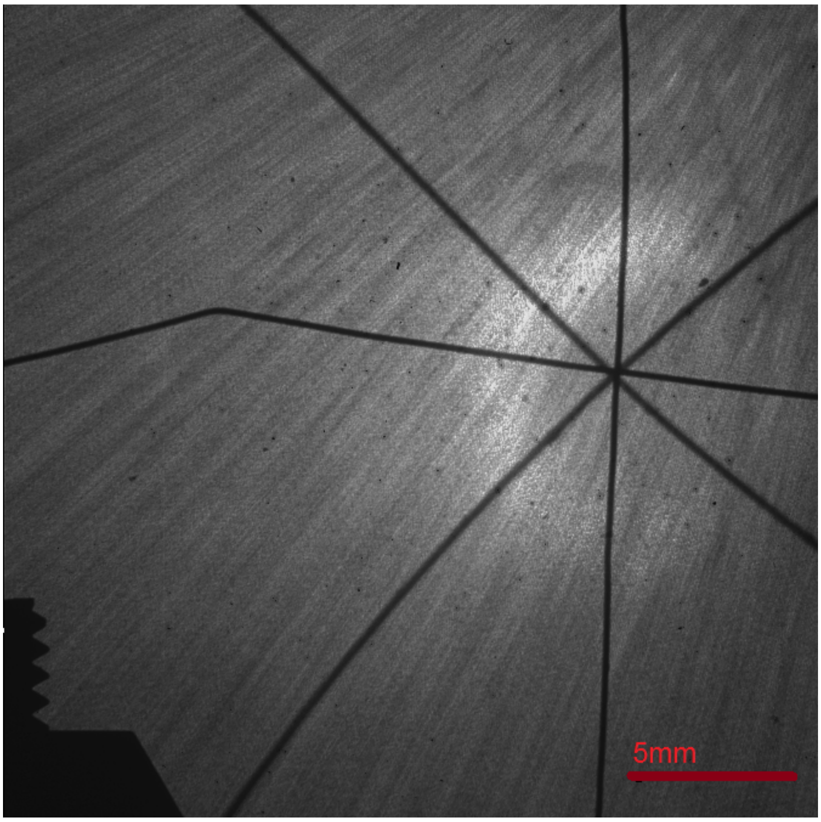

Figure 5.4: CCD image of Capillary discharge laser beam profile showing the annular shape caused by refraction within the capillary tube. CCD camera is covered with 0.8μm Al filters. Shadows can be seen from two alignment crosswires and a mirror-post with screw

divergence and in the case of the capillary discharge laser, causes an annular beam profile (Figure 5.4) [70].

5.1.3 Beam Profile

The output beam profile of the capillary discharge laser has an annular shape due to the refraction within the plasma. The annular profile produced has been imaged using a Andor iKon-L CCD camera (Figure 5.4). To express the beam profile analytically, lineouts were taken of the beam profile and a Gaussian fit was applied (Figure 5.5), where,

$$I_{fit} = y_0 + A \exp\left[-\left(\frac{r - r_0}{W}\right)^2 \right]. \tag{5.13}$$

The fit parameters, y_0, A, r_0 and W are estimated from the original data (blue) and r is the distance from the centre of the beam. The steep decrease in signal from 0mm to 1mm

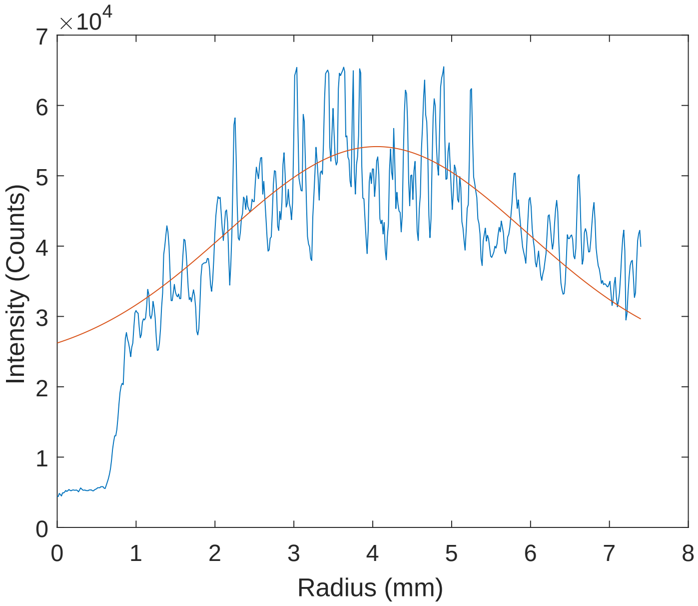

Figure 5.5: Lineout of beam profile (blue) and Gaussian fit (red) taken from the centre of the beam (r=0) outwards. The drop in intenstiy at r=1 is caused by the shadow of the cross-wires used for alignment in Figure 5.4. Background x-rays are producing a constant output of approxiamtly 2.5×10^4 counts.

is caused by the shadow of the cross-wires seen in Figure 5.4. The beam profile shown in Figure 5.5 gives the beam diameter at 1.65m from the pinhole exit of the capillary laser as approximately 7.5mm indicating a beam divergence of 4.5mrad. The annular profile of the beam is caused by refraction of rays away from the central axis of the plasma column within the capillary.

A ray in the capillary laser medium will experience the maximum amplification when $\theta(0) = 0$. For a length of amplification $z_p = 0.15m$ modelled scale length $L < 1$mm and peak electron density $n_e(0) = 10^{19}\text{cm}^{-3}$ we obtain $\theta \approx 5$mrad which is within range of the measured divergence of $\theta = 4.5$mrad.

5.2 Plasma current flow

Considering a uniform fully ionised plasma with a constant applied electric field. The current, J, is given by Ohm's law as,

$$\vec{J} = \sigma \vec{E}, \tag{5.14}$$

where σ is the conductivity of the plasma. This can be taken as the Spitzer conductivity,

$$\sigma = \frac{\pi Z_i e^2 m^{1/2} \ln \Lambda}{(4\pi\epsilon_0)^2 (k_B T_e)^{3/2}} \Omega m \tag{5.15}$$

where Z_i is the ion charge, T_e is the electron temperature in electron volts and $\ln \Lambda$ is the Coulomb logarithm, which is assumed to be equal to unity [73].

For temperature T expressed in eV, we have [74]

$$\sigma \approx 10^{-4} \frac{Z_i}{T^{3/2}}. \tag{5.16}$$

If the voltage of the applied electric field is known the power (P) supplied to the plasma can be calculated using,

$$P = \int_V J^2 / \sigma dV. \tag{5.17}$$

If the current flow is known this becomes,

$$\frac{I_p^2}{P} = \frac{\pi r_p^2}{z_p}, \tag{5.18}$$

where r_p is the radius of the plasma and z_p is the length of the plasma column. This gives an equation for the plasma current,

$$I_p = \frac{\pi r_p^2 V}{\sigma z_p}. \tag{5.19}$$

The plasma conductivity can be found by applying the electron temperatures required to ionise argon to Ar^{8+} which are in the range 40-80eV [68], to Equation (5.16), where $\sigma = 1 \times 10^{-5} - 3 \times 10^{-5} \text{cm}^{(-1)}$. Substituting this into Equation (5.19) along with the applied voltage (V=0.3MV) and z_P=21cm, the plasma current can be estimated. Assuming a plasma column radius of $r_p = 100\mu$m the plasma current is $I_p = 26 - 41$kA, which agrees with previously published work on capillary discharge lasers [68].

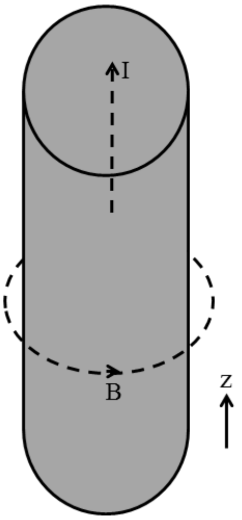

Figure 5.6: Magnetic field and current acting on a plasma column a Z-pinch

5.3 Z-pinch and Bennett Relation

A Z-pinch originates from the Lorentz force when a current carrying conductor experiences a inwards $\vec{J} \times \vec{B}$ force. In this case the current carrying conductor is a plasma and the inwards $\vec{J} \times \vec{B}$ causes the plasma to compress (Figure 5.6). The Bennett relation, assumes that the magnetic pressure is equal to the plasma pressure. From Ampere's law and the integral form of Maxwell's equation, we can find the magnetic force acting on the plasma,

$$B = \frac{\mu I}{2\pi r}. \tag{5.20}$$

The magnetic pressure caused by the induced magnetic field is given by,

$$P_B = \frac{B^2}{2\mu}, \tag{5.21}$$

which is equal to the plasma pressure.

The plasma pressure is related to the electron and ion temperature (T_e and T_i) and density (n_e and n_i) by,

$$P = n_i k_B T_i + n_e k_B T_e \approxeq n_e k_B T_e. \tag{5.22}$$

as the electron density for a highly energised plasma is greater than the ion density n_i. Equating equations Equations (5.21) and (5.22), we have

$$\frac{B^2}{2\mu} = n_e k_b T_e. \tag{5.23}$$

Substituting Equations (5.16) and (5.19) we obtain an expression for the plasma temperature,

$$T_e = \left[8 \times 10^{-8} \frac{n_e e}{\mu} \left(\frac{Z_i^3}{r_p^2} \right) \left(\frac{L_p}{V} \right)^2 \right]^{1/2} \tag{5.24}$$

The argon pressure can be used to estimate the ion density n_i. Using a given argon pressure (P) and assuming Avogadro's number of gas particles at room temperature and pressure (293° K and 1atm) occupy 22.4 litres gives an ion density of,

$$n_i = 2.46 \times 10^{25} \frac{P}{P_{atm}} \tag{5.25}$$

where P_{atm} =1atm. The initial radius of the plasma will occupy the capillary tube, r_c, the plasma current flow induces a Z-pinch which will compress this to r_p. Once the plasma has been compressed the ion density will increase to,

$$n_i = 2.46 \times 10^{25} \frac{P}{P_{atm}} \left(\frac{r_c}{r_p} \right)^2, \tag{5.26}$$

the electron temperature becomes,

$$T_e = \left[2.51 \times 10^5 \left(\frac{P}{P_{atm}} \right) \left(\frac{r_c}{r_p} \right)^2 \left(\frac{Z_i^3}{r_p^2} \right) \left(\frac{L_p}{V} \right)^2 \right]^{1/2}. \tag{5.27}$$

For the capillary discharge laser, the initial argon pressure $P = 0.3$Torr, the capillary radius r_c=1.5mm and the compressed plasma radius r_p=100μm as given by Rocca *et. al.* [75], Z_i=8 for Ar^{8+}. The plasma length L_p=21cm and the voltage V=0.3MV, we obtain an electron temperature of $T_e \approx 50$eV.

5.4 Laser Diagnostics

The capillary discharge laser is usually used with four diagnostics which monitor its performance: a Rogowski coil to measure plasma current flow in the capillary, a gold photo-diode to measure the laser output energy, an in-line photo-ionisation detector to provide a measurement of the laser energy without disturbing the beam and an EUV sensitive CCD camera to measure the laser beam profile. The Rogowski coil and in-line detector can be used without disturbing the beam, allowing voltage and energy measurements to be recorded throughout an experiment.

5.4.1 Rogowski Coil

The current flow in the capillary discharge is measured by a Rogowski coil. The Rogowski coil is placed as part of the capillary housing near the exit of the capillary, so that the rate of change of current produced by the plasma can be measured. A Rogowski coil is a solenoidal coil whose ends come together to make a torus. If a coil has a cross sectional area A_c, and n turns per unit length,

$$n = \frac{N}{2\pi r_c} \tag{5.28}$$

where N is the total number of turns and r_c is the radius of the coil. If we assume the magnetic field does not vary over each turn spacing ($|\nabla B|/B << n$), the flux can be written as an integral over each individual turn [73],

$$\Phi = n \oint_l \int_{A_c} dA\mathbf{B} \,.\, \mathbf{dl}. \tag{5.29}$$

According to Amperes law,

$$\oint_l \mathbf{B} \,.\, \mathbf{dl} = \mu I, \tag{5.30}$$

where I_p is the the plasma current encircled by l, and μ is the magnetic permeability. The flux can then be simplified to,

Figure 5.7: Photo of the Rogowski coil installed in the capillary discharge laser,which consists of a helical coil of wire with one end returning through the centre of the coil to the other end, so that both terminals are at the same end of the coil.

$$\Phi = nA_c\mu I_p, \tag{5.31}$$

and the output voltage is given by

$$V_{out} = nA_c\mu \frac{dI_p}{dt}. \tag{5.32}$$

For a sufficiently fast pulse the Rogowski coil is self integrating so a detected voltage is proportional to the plasma current,

$$V_{det} = \frac{R_{det}nA_c\mu}{L_{coil}} I_p, \tag{5.33}$$

where R_{det} is the impedance used to measure the voltage drop V_{det} and L_{coil} is the inductance of the Rogowski coil.

The rogowski coil used with the capillary discharge laser has $n = 33$ turns, A_c=0.6mm R=0.2Ω and L_{coil}=10μF. With a typical voltage reading of V_{det}=20V for a high voltage pulse, this corresponds to $I_p = 40$kA.

5.4.2 Gold Photo-diode

The gold photo-diode uses a high voltage applied as a bias across two metal plates to detect changes in pulse energy caused by the flow of electrons due to the photoelectric effect. Figure 5.8 shows that the laser pulse goes through a series of unbiased attenuators to a biased mesh before impacting the gold detector head. The biased mesh is at a voltage of -1800V so that when the laser pulse excites electrons from the gold detector head, the electrons are repelled towards the grounded mesh. The flow of the electrons from the detector head to the biased mesh creates an electrical current which is proportional to the energy in the laser pulse.

The laser pulse energy is related to the time integrated voltage V through,

$$E = \frac{E_{photon}A}{qHZ_{imp}} \int_{-\infty}^{\infty} V dt, \tag{5.34}$$

where E_{photon} is the photon energy (24.6eV), A is the signal attenuator used for measure-

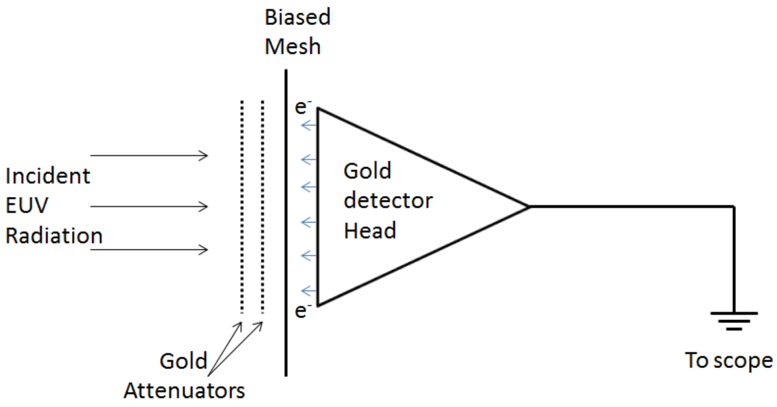

Figure 5.8: Schmetic of a gold photoionisation detector

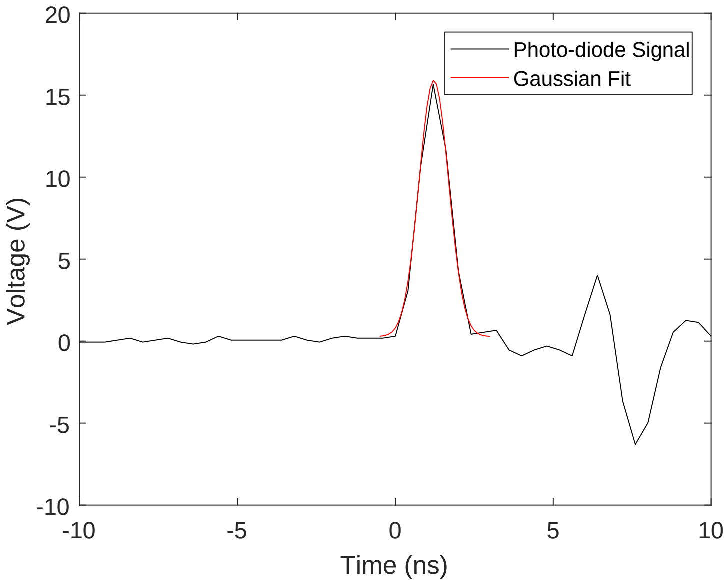

Figure 5.9: Photo-diode signal at 42kV input voltage, firing at 3Hz at a pressure of 283mTorr, a Gaussian fit to the photo-diode signal is superimposed

ments, Z_{imp} is the detector's impedance, H is the attenuation of the filter and q is the quantum efficiency of the absorbing material. For the diode used, the impedance $Z_{imp} = 50\Omega$ and the gold has a quantum efficiency $q = 0.054$. The gold coated mesh has a transmission fraction (H) of approximately 4%, which is determined by the number of holes in the mesh and the size of each hole. This has been callibrated using a source with a known energy output. The signal from the photo-diode is shown in Figure 5.9 corresponds to an energy of $E = 47\mu$J.

5.4.3 In-line photoionisation detector

The in-line photo-ionisation detector again uses a high voltage between two surfaces, creating an electric field. This electric field generates an electrical current detected on an oscilloscope from the electrons produced by the ionisation of the background argon and electrons are produced through the photoelectric effect. However, this causes a high dependence on the pressure of the background argon. A higher argon pressure will mean there are more argon atoms available to ionise making this a much less accurate method of measuring the beam energy than the photo-diode. The current produced is proportional to the number of photons in the laser pulse and therefore the pulse energy. The lower voltages recorded by the in-line detector also means that at low laser energy it is difficult to distinguish the pulse from background noise, therefore the in-line detector can only reliably be used to measure high energy pulses.

The detector is designed in such a way that it produces an electric field that crosses the path of the laser beam, The schematic in 5.10 shows that the geometry of the detector allows the laser to pass through two concentric cylindrical steel tubes one grounded outer tube and one smaller semi-circular inner tube with a voltage applied across it.

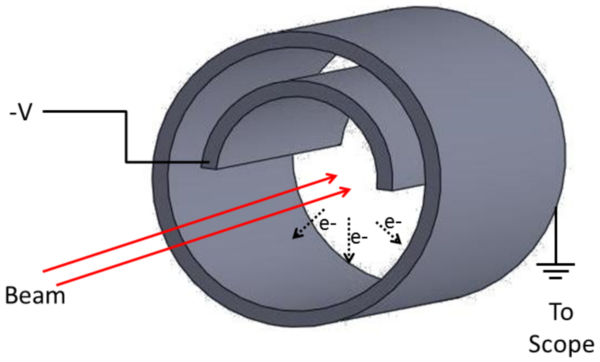

Figure 5.10: Schematic of the in-line photoimisation detector showing the semi-circular inner tube and the cylindrical outer tube. Electrons produced by photo-ionisation in background argon gas are collected at the outter cylinder.

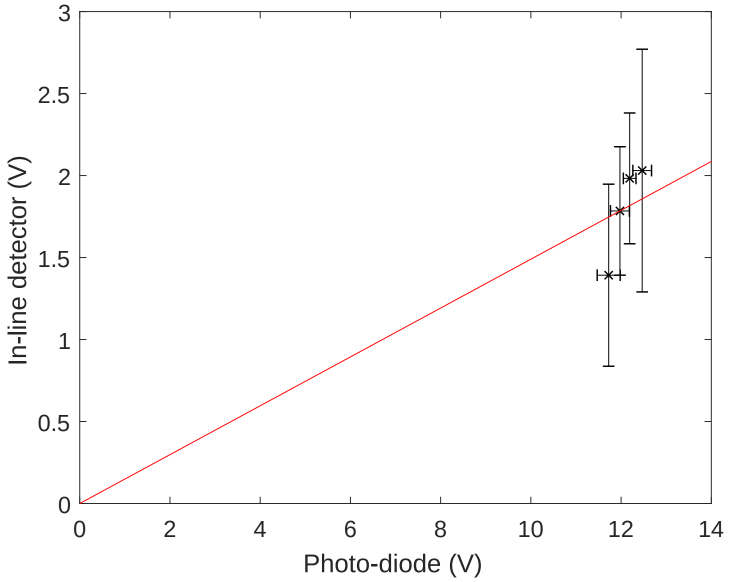

Figure 5.11: Comparison of voltage readings taken simultaneously on the gold photo-diode and in-line detector for various input voltages at 270mTorr Argon pressure.

The in-line detector and gold photo-diode can be calibrated for different argon gas pressures. A higher argon pressure will increase the number of electrons photo-ionised in the in-line detector and increase the energy readings. Once calibrated, the in-line detector can be used during experiments to give a reading for the beam energy without disturbing the beam.

The plot in Figure Figure 5.11 shows an average of the responses of the in-line detector and photo-diode at four different input voltages. This gives a cross-calibration of the results from the gold photo-diode and the in-line detector. Voltage signals from both detectors are measured by an oscilloscope and are numerically analysed using Equation (5.34) to deduce the output energy. Figure 5.11 confirms that the in-line detector can be used to measure beam energy fairly well. However, it is necessary to have the in-line detector well calibrated before use in order to achieve a reliable energy reading.

5.4.4 CCD Camera

A Charged Coupled Device (CCD camera) is used as a camera to image the output of the laser. CCD cameras work using arrays of electric potential wells in p-doped depletion regions induced in a silicon semiconductor by matrices of closely spaced electrodes. Information stored in the potential wells as electron charge excited to the conduction band is transferred

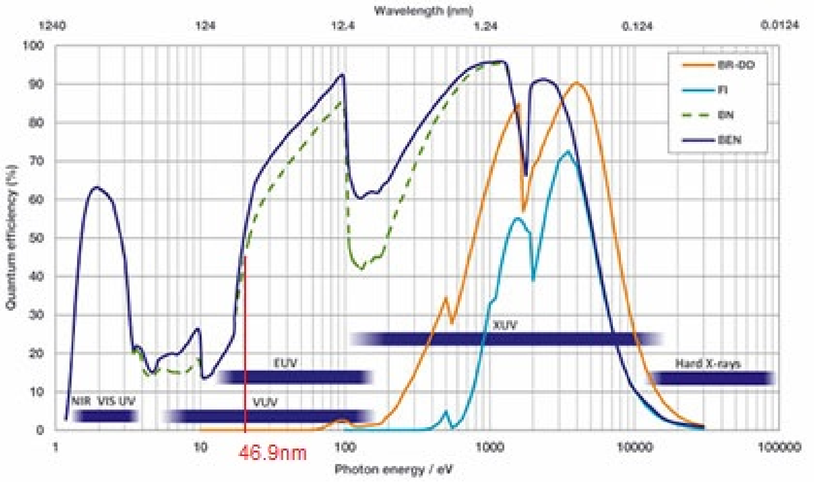

Figure 5.12: Quantum efficiency curve for Andor iKon-L SO cameras, the camera used in thie research has a BN sensor (dashed green). Taken from Andor iKon-L SO series specifications produced by the manufacturer [77].

by adjusting the voltage applied to the surrounding electrodes [76].

Traditional CCD cameras are front illuminated on the same side as the electrodes. Unfortunately, these are insensitive in the 10eV-500eV photon energy range due to the absorption of the radiation in the electrode structure. However, the EUV energy range can be detected using a back illuminated thinned substrate. Back illuminated CCD cameras provide direct access for incident radiation to the depleted region through the backside of a thinned silica substrate. A thin oxide layer (2nm) forms on the back surface of the substrate after thinning. This causes a positive charge which in turn causes a reverse potential towards the surface and a depletion region (100nm thick) develops. For wavelengths in this region of EUV the absorption length can be much less than 100nm therefore the recombination of photo-generated charge in this area must be minimised. This is done by adding a thin p-type semi-conductive layer at the back surface of the CCD chip, which also prevents damage. The degree of silicon thinning is specific to each research application [76, 77].

The camera used in this research is a Andor iKon-L SO with a BN back illuminated chip. The camera has a sensitive area of 27.6mm^2 with 2048 x 2048 active pixels with each pixel of area 13.5μm^2. The maximum active pixel well depth is approximately 100 electrons. The maximum quantum efficiency of the camera is 95%, but at 24.6eV (46.9nm) the quantum efficiency is approximately 57% (Figure 5.12) [77].

The image in Figure 5.4 was taken with a 0.8μm aluminium filter protecting the CCD chip.

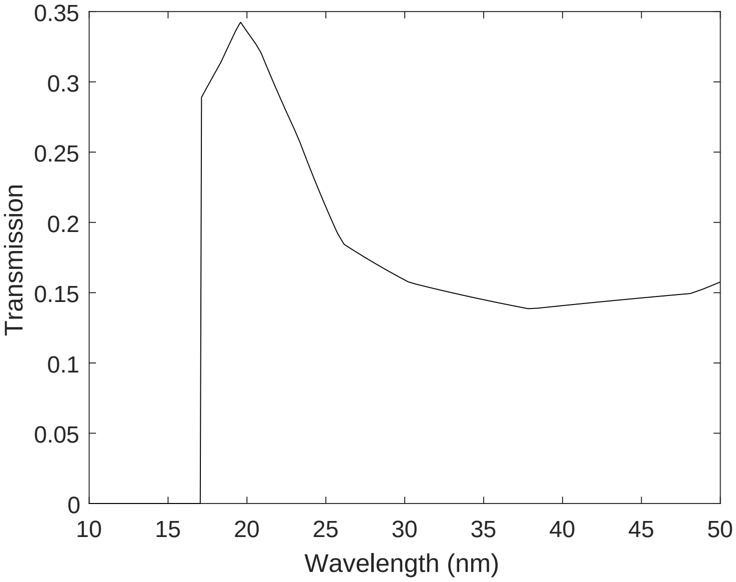

Figure 5.13: Transmission through 0.8μm Aluminium filters over a wavelength range of 10nm to 50nm [2]

The filter blocks all optical emissions from reaching the chip but allows transmission of EUV. Figure 5.13 shows the transmission through aluminium of EUV radiation with a wavelength range from 10m to 50nm, the peak transmission of 0.34 can be seen at a wavelength 19.6nm, and the aluminium L-edge can be seen at 17.1nm. The L-edge is associated with the removal of a core electron by photo-absorption from the most tightly bound atomic state where the L represents the quantum number n=2. At wavelengths below the L-edge the radiation is absorbed by the aluminium [1]. The transmission at 46.9nm is 0.148, which is sufficient to protect the CCD chip from over-exposure [2].

Transmission of the filter may be a little lower than the 0.148 shown in Figure 5.13 due to the oxidation of aluminium to aluminium oxide on the surface of the filter. This can be factored into calculations by measuring the thickness of the Al_2O_3. The Al_2O_3 surface on the Al filter was measured using a Film Metrics F20 film thickness measurement instrument. The F20 has a wavelength range from 380nm to 1050nm and can measure thickness from 15nm to 70μm. The Al_2O_3 surface was measured to be 50nm on each surface of the Al filter. The transmission for 50nm of Al_2O_3 is shown in Figure 5.14 where the transmission at 46.9nm is 1.4×10^{-2}. Combining this with the transmission of Al at 46.9nm the total transmission of a Al filter with a 50nm film of Al_2O_3 on each surface is 2.9×10^{-5}.

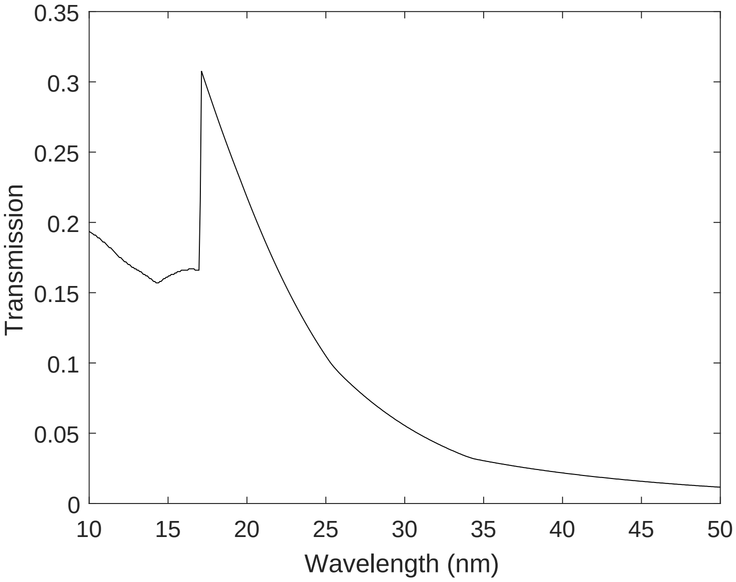

Figure 5.14: Transmission through thickness of 50nm Al_2O_3 over a wavelength range of 10nm to 50nm [2]

The transmission through an aluminium filter with an oxidised layer of thickness 50nm, on each surface allows the laser to be fired directly onto the CCD through the filter in order to image the beam profile (Figure 5.4) [2].

5.5 Conclusions

This chapter has reviewed the physics behind a capillary discharge laser. We have reviewed the atomic process of how lasing occurs at 46.9nm, and the characteristics of the beam which is produced. The main factors we have investigated have shown that the gain and refraction of the radiation within the compressed plasma are essential to the lasing at 46.9nm. It has also been shown that the beam profile is an unusual double gaussian or annular shape due to the refractions within the plasma column. The diagnostic techniques used in characterising the beam have also been discussed, using novel techniques such as the in-line detector.

Chapter 6

Characterisation of the Capillary Discharge Lasers

Chapter 5 discusses the physics behind the capillary discharge laser. This chapter discusses how this is applied to make a capillary discharge laser work, focusing on the electrical pulses and optimisation of the laser output. There is also discussion of the optical emission of the plasma produced at different stages throughout the ignition process and some of the issues with developing the laser.

6.1 Electrical Discharge Characterisation

6.1.1 Radio Frequency Plasmas

The initial argon plasma produced in the capillary is created by radio-frequency (RF) heating at 60MHz. A lightly ionised plasma is needed to conduct a 40kA pulse to produce sufficient heating to create a neon-like argon plasma and to achieve lasing at 46.9nm. A current is induced in a plasma by driving an RF current through an adjacent coil. The current flowing through the coil causes an evanescent magnetic and electric field disturbance which decays over a few cm into the plasma. The RF current in the plasma transfers kinetic energy to the electrons. The changing magnetic field created by the current in an external coil can easily enable H-mode coupling to the plasma. The coil can couple to the plasma electrostatically,

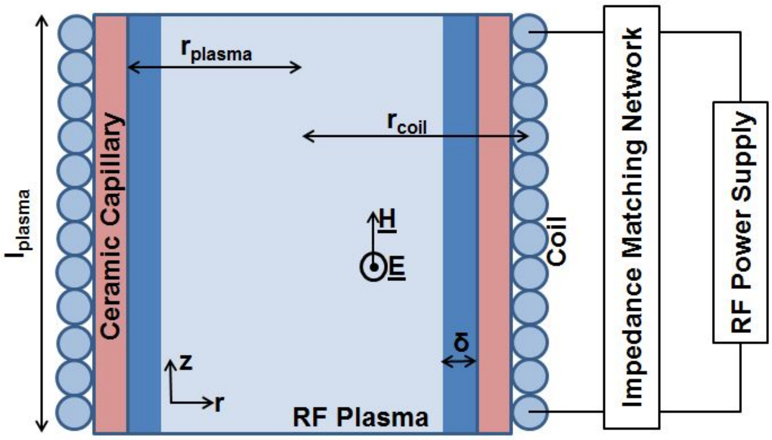

Figure 6.1: Schematic of the capillary, showing the inductive coil surrounding the capillary with the plasma forming inside. The electric and magnetic fields are shown and the plasma skin depth.

meaning the plasma may also operate in E-mode. Such inductively coupled plasmas (ICP) are usually heated in E-mode, but the heating undergoes an E-H transition as the power to the coil increases [78, 79].

For the case of a capillary discharge laser the RF plasma is generated inside the capillary, which is surrounded by the inductive RF coil (Figure 6.1). The power deposited from the RF power supply to the plasma is through an impedance matching network to minimise back reflections into the RF power supply.

6.1.1.1 RF plasma density

The inductive coil near the plasma has a number of turns (n), a resistance (R_{coil}) and inductance (L_{coil}). The RF signal has a sinusoidal voltage (V_{coil}) and a RF frequency (ω) which when applied to the coil produces a current (I_{coil}). The plasma acts as an electrically conductive fluid which forms the equivalent of a one turn secondary coil of an air-core transformer with inductance L_{mp} [78]. The impedance of the plasma depends on L_{mp} and the plasma resistance, R_p. The plasma resistance can used to find the skin depth of the plasma (δ), which is dependant on the plasma density, therefore linking the plasma resistance to the plasma density. The plasma resistance (R_p) can be measured through the electrical parameters of the RF circuit, which can then give us an estimate of the plasma density as shown by Bandyopadhyay and Chabert [78, 81].

For the capillary discharge laser, the measured values are; n=10, $R_{coil} = 0.2\Omega$ and $L_{coil} =$ 480nH. We can make an estimation for the electron collision frequency (v_e). For a gas pressure of 300mTorr, $v_e \approx 2 \times 10^8 s^{-1}$ [80]. Other important parameters include the plasma radius, r_p = 1.5mm, the coil radius r_{coil} = 5.3mm, and the length of the plasma column, l_{plasma} = 21cm.

The effective resistance (R_s) and inductance (L_s) across the coil is given by [73],

$$R_s = R_{coil} + M^2\omega^2 \left[\frac{R_p}{R_p^2 + \omega^2 \big(L_{mp} + \frac{R_p}{v_e} \big)^2} \right], \tag{6.1}$$

$$L_s = L_{coil} - M^2\omega^2 \left[\frac{L_{mp} + \frac{R_p}{v_e}}{R_p^2 + \omega^2 \big(L_{mp} + \frac{R_p}{v_e} \big)^2} \right], \tag{6.2}$$

where M is the mutual impedance between the coil and the plasma and is given by

$$M^2 = k_p^2 L_{coil}(L_{mp} + \frac{R_p}{v_e}) \approx k_p^2 L_{coil} L_{mp}, \tag{6.3}$$

where k_p is approximately the ratio of the radius of the coil to the radius of the plasma, $k_p \approx \frac{r_p^2}{r_{coil}^2}$ [78, 81].

For a high electron density plasma Equation (6.2) can be simplified to give,

$$L_s = L_{coil}(1 - \frac{r_p^2}{r_{coil}^2}), \tag{6.4}$$

where L_s = 438nH.

The inductance of the plasma (L_{mp}) in the high electron density scheme can be given by,

$$L_{mp} = \frac{\mu_0 \pi r_p^2}{l}, \tag{6.5}$$

which cancels with the equation for the inductance of the coil (L_{coil}), to give

$$L_{mp} = L_{coil}\Big(\frac{k_p}{n_{coil}^2} \Big), \tag{6.6}$$

where $L_{mp} = 0.418nH$.

We can now rearrange Equation (6.2) to obtain a value for the resistance of the plasma. We have that $\frac{R_p}{v_e} << 1\Omega s^{-1}$ so we can assume $\frac{R_p}{v_e} \approx 0$. We can find that the plasma $R_p = 0.024\Omega$ and using Equation (6.1) we then have the effective resistance of the coil $R_s = 0.309\Omega$.

Resistance (R_p) and inductance (L_{mp}) can also be found by solving Equations (6.1) and (6.2),

$$L_{mp} = \frac{L_{coil}}{n_{coil}^2}\left(\sqrt{\frac{\omega^2(L_{coil}-L_s)^2+(R_s-R_{coil})^2}{L_{coil}\omega^2\big[(L_{coil}-L_s)-\frac{1}{v_e}(R_s-R_{coil})\big]}}\right), \tag{6.7}$$

$$R_p = L_{mp}\Big(\big[\frac{L_{coil}-L_s}{R_s-R_{coil}}\big]-\frac{1}{v_e}\Big)^{-1}, \tag{6.8}$$

$$R_p = \frac{L_{coil}}{n_{coil}^2}\left(\sqrt{\frac{\omega^2(L_{coil}-L_s)^2+(R_s-R_{coil})^2}{L_{coil}\omega^2\big[(L_{coil}-L_s)-\frac{1}{v_e}(R_s-R_{coil})\big]}}\right)\Big(\big[\frac{L_{coil}-L_s}{R_s-R_{coil}}\big]-\frac{1}{v_e}\Big)^{-1}. \tag{6.9}$$

These can be simplified to give values for R_p and L_{mp} in terms of V_{coil}, I_{coil} and ϕ,

$$R_s = \frac{V_{coil}}{I_{coil}}\cos\phi \tag{6.10}$$

and

$$L_s = \frac{V_{coil}}{\omega I_{coil}}\sin\phi \tag{6.11}$$

where ϕ is the phase difference between the voltage and current,

$$\phi = \tan^{-1}\Big(\frac{\omega L_{mp}}{R_p}\Big) = \tan^{-1}\omega\left[\Big(\frac{L_{coil}-L_s}{R_s-R_{coil}}\Big)-\frac{1}{v_e}\right]. \tag{6.12}$$

The plasma conductivity σ is given by,

$$\sigma = \frac{l}{R_pA_{eff}}, \tag{6.13}$$

where A_{eff} is the effective cross-sectional area of the plasma and l is the width of the plasma column. The plasma being considered here as a cylindrical column of thickness δ, width l_{plasma} and length $2\pi r_c$, therefore the effective cross-sectional area is given by

$A_{eff} = \delta \times l_{plasma}$. The real part of the plasma conductivity is given as [81],

$$Re(\sigma) \approx \frac{2\pi r_c}{R_p \delta . l_{plasma}} = \frac{n_e e^2 . v_e}{m_e (V_e^2 + \omega^2)}, \tag{6.14}$$

where n_e is the plasma density.

The plasma skin depth is given as $\delta_n = \frac{c}{\omega_p}$ where c is the speed of light in a vacuum and ω_p is the plasma frequency . The plasma frequency can be written in terms of the plasma density [78],

$$\omega_p = \sqrt{\Big(\frac{n_e e^2}{m_e \epsilon_0}\Big)} \approx \sqrt{(3.2^3 n_e)} \tag{6.15}$$

combining this and Equation (6.14) we get an equation for the plasma density,

$$n_e = 3200 \Big(\frac{2\pi m_e}{c e^2}\Big)^2 \Big(\frac{r_c}{l_{plasma}}\Big)^2 \Big(\frac{v_e^2 + \omega^2}{v_e}\Big)^2 \Big(\frac{1}{R_p}\Big)^2, \tag{6.16}$$

Substituting known values into the above equations we find that $n_e \approx 7.5 \times 10^{18} \mathrm{m}^{-3}$.

6.1.1.2 Impedance Matching Network

Impedance matching networks (IMN) are essential in a RF plasma system as they are used to generate and stabilise the plasma as well as to protect the RF electrical circuit and enable power deposited in the plasma to be maximised. The IMN minimises the difference in impedance to the surrounding gas, to ensure efficient transfer of the RF power from the power supply to the plasma, and to compensate for variations in impedance as the plasma is running [82].

There are three main components of the ICP matching network employed in the RF heating of the capillary laser;

1. Shunt capacitor
2. Loading capacitor (Tuning capacitor)
3. Loading coil

The shunt capacitor can be manually controlled and consists of a series of fixed ceramic capacitors with a variable air capacitor. The loading capacitor is adjusted manually and monitored through a dual directional coupler, which allows an oscilloscope to record the forward and reflected electrical power in the RF circuit from the plasma (Figure 6.2). The dual directional coupler is a passive device that couples part of the transmission power in a transmission line. In the capillary discharge laser set-up the dual directional coupler measures the forward power (Pf) supplied to the plasma and the reflected power (Pr), the difference in these gives the power deposited in the plasma. The dual directional coupler operates in a frequency range from 40-80MHz, is terminated into 50Ω and has a coupling value of 50dB, where the coupling value is given by,

$$C = 10 \log \left(\frac{P_{in}}{P_{out}} \right), \tag{6.17}$$

A coupling value of 50dB gives that $\frac{P_{in}}{P_{out}} = 1 \times 10^5$.

The dual directional coupler gives a peak-to-peak forward voltage, $Vf_{pp} \approx 1V$ and a reflected voltage $Vr_{pp} = 0.1V$ (Figure 6.2). Converting the peak-to-peak voltage to the root mean square voltage (V_{rms}) for both forward and reflected voltage by,

$$V_{rms} = \frac{V_{pp}}{2\sqrt{2}}, \tag{6.18}$$

the average power can then be calculated,

$$P_{avg} = \frac{V_{rms}^2}{R}. \tag{6.19}$$

From this we get a value for the forward power, $P_f = 250W$, and reflected power, $P_r = 2.5W$.

6.1.2 Pre-ionisation Pulse

The pre-ionisation pulse is triggered by the DC pre-ionisation (DCP) and lesser high voltage (LHV) controls. The DCP unit charges the LHV which then produces an 8kV pre-ionisation

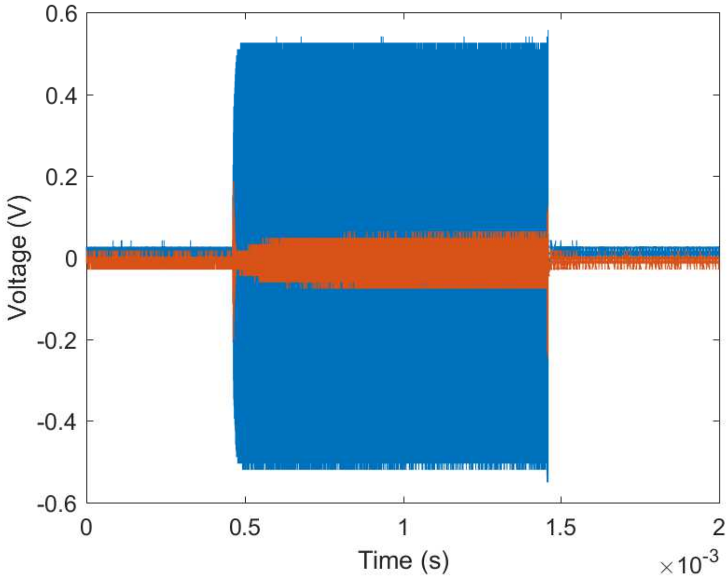

Figure 6.2: Forward (blue) and reflected (red) voltage of RF power injected and reflected by the Argon plasma, measured via a dual directional coupler. The rapid oscillation of the RF at frequency 60MHz is not observable on the timescale shown, but the relative amplitude of the forward and reflected power is apparent.

pulse which feeds into the laser tank and is discharged through the plasma in the bore of the capillary. The capillary already has an argon RF plasma ignited, the pre-ionisation pulse ionises the plasma, but does not excite the electrons to Ar^{8+} so lasing does not occur. The pulse is monitored through the a Rogowski coil which is at the exit of the capillary (see Section 5.4.1 for more details on Rogowski coils).

The pre-ionisation pulse occurs $2 - 4\mu s$ after the burst phase of the RF pulse (Section 6.5). This means the RF plasma is still ignited, but the extra power in the plasma will not damage the RF circuit. The pre-ionisation pulse has a duration of approximately $12\mu s$ and with a voltage from the Rogowski coil of approximately 150mV. The pulse should be optimised using the RF matching box to give a smooth curve, poor matching will cause instabilities in the pulse which may cause damage to the capillary or cause the laser to miss-fire.

6.1.3 Thyratron Trigger

A Thyratron is a gas filled valve which acts as a switch for the high voltage pulse. In the case of the capillary discharge laser the thyratron used is hydrogen based. When ionised the gas inside the thyratron undergoes a Townsend discharge. This occurs when free electrons

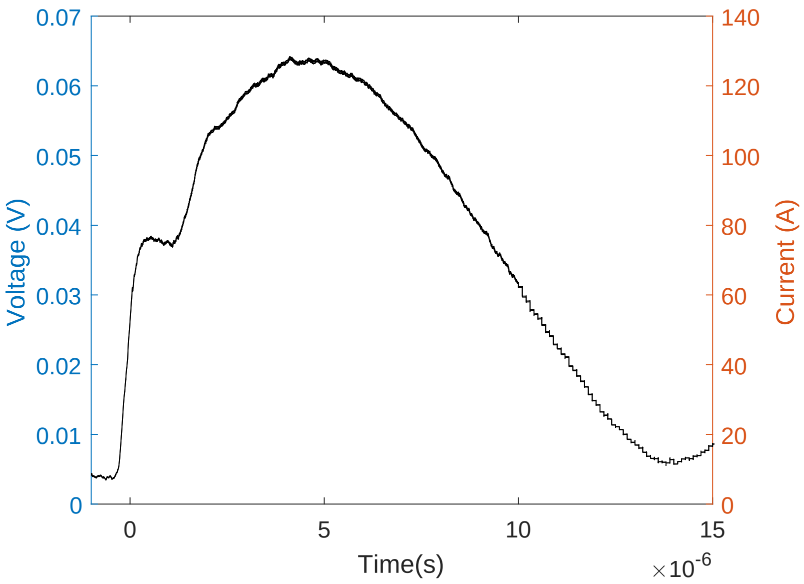

Figure 6.3: Pre-ionisation current fired using DCP and LHV controls as measured using the Rogowski coil. Left axis shows voltage measured by the oscilloscope and right shows the calculated current.

are accelerated by an electric field and collide with gas molecules. This produces more free electrons and causes a cascade effect which allows electrical conduction through the ionised gas. The advantages of using hydrogen as the ionised gas are the low molecular weight and high breakdown strength at low pressure. This allows for fast high voltage switching [83].

For testing purposes the thyratron is triggered on a lower voltage, this allows the thyratron pulse to be optimised with the pre-ionisation pulse to achieve optimum lasing conditions. When switched on the thyratron trigger should produce a low voltage pulse $6 - 12\mu s$ after the start of the pre-ionisations pulse. This mimics the timing of the main high voltage pulse. The current measured by the Rogowski coil should appear as shown in Figure 6.4 where the thyratron pulse occurs at $t \approx 11\mu s$. We can see from the image that the thyratron pulse is approximately 9μs after the initial rise of the pre-ionisation pulse.

6.1.4 High Voltage Pulse

The high voltage pulse is used to cause the $\vec{J} \times \vec{B}$ force, which pinches the plasma and causes the population inversion and lasing. The input voltage can be set using a controller and

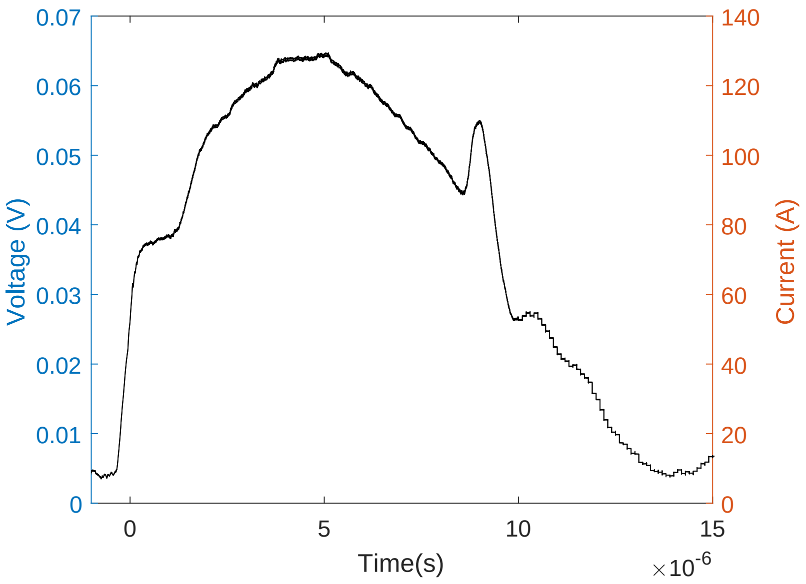

Figure 6.4: Pre-ionisation and thyratron pulses, with the Thyratron pulse occuring 9μs after the start of the pre-ionisation pulse, as measured with the Rogowski coil. Left axis shows voltage measured on the oscilloscope and right shows the calculated current.

can range from 10kV to approximately 45kV. All other pulses must be firing and optimised before the HV pulse is switched on. The pulse should occur in the same position as the thyratron trigger pulse, but has a much higher indicated voltage (≈30V measured by the Rogowski coil) and shorter duration (≈80ns) (Figure 6.5).

A new capillary will need to begin firing at an input voltage of 20kV and this can be gradually increased up to 40-42kV, where lasing should occur. However, the new capillary needs to be conditioned, which can require up to 10000 shots before lasing occurs. This allows the plasma to remove any residual contaminants which may be inside the capillary. These could be oil traces from the transformer oil or residue from the cleaning processes.

The gold photo-diode can be used to detect if lasing is occurring. It needs to be set up with a -1800V power supply and a readout to the oscilloscope. Once lasing occurs a peak should appear from the photo-diode, as shown in Figure 5.9. This peak represents the lasing voltage produced by the photo-diode, and can be converted to beam energy using Equation (5.34). Typically the pulse energy is 50μJ.

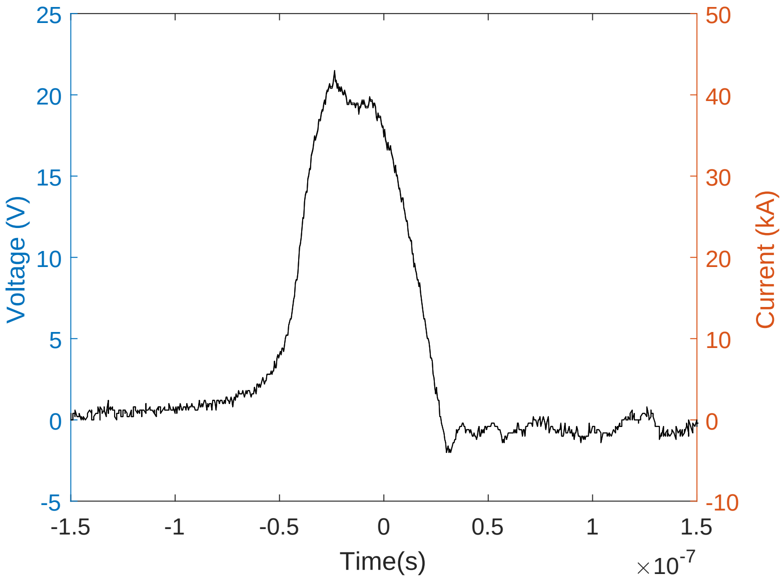

Figure 6.5: High Voltage pulse firing with 40kV input voltage, as measured with the Rogowski coil. Left axis shows voltage measured on the oscilloscope and right shows the calculated current.

6.2 Electrical Pulse Forming Network

The electrical pulse forming network on a capillary discharge laser produces a high voltage electrical current down the argon filled capillary causing argon to ionise to Ar^{8+}. The plasma is also compressed as a z-pinch. The pulse forming network uses Blumlein transmission lines to amplify and compress a lower voltage pulse generated from a standard high voltage power supply.

In a Blumlein transmission line a resistive load is connected to two transmission lines of equal length which are charged by a power supply (Figure 6.6).The impedance of the transmission line is half of the impedance of the load, which means the voltage step is reflected. This gives two equal voltage steps of opposite polarity, giving a voltage increase by a fraction of 2.

The duration of the pulse (Δt) is determined by the length of the transmission lines (D) where [84],

$$\Delta t = \frac{2D}{c}, \tag{6.20}$$

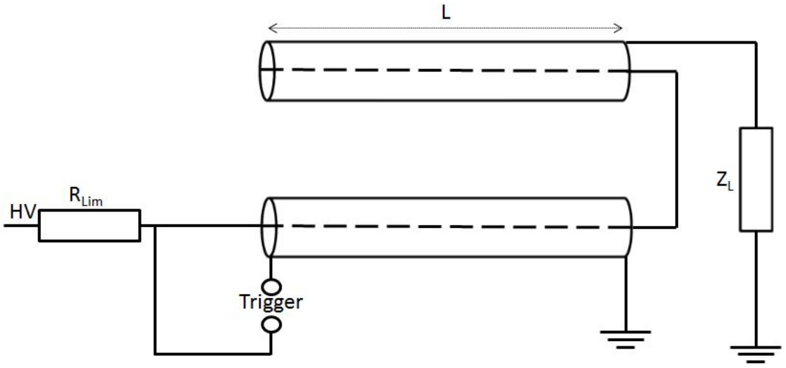

Figure 6.6: Circuit diagram of a Blumlein line showing the high voltage input (HV), the current limiting resistance (R_{Lim}) and the load impedance (Z_L)

In the capillary discharge laser a voltage of 40kV is compressed sequentially in a series of Blumlein transmission lines to produce a voltage of 300kV, which is applied to the argon plasma generated in the capillary. The number of transmission lines needed to produce 30kV is given by,

$$n = \frac{\log_{10}\left(V_{out}/V_{in}\right)}{\log_{10}(2)}. \tag{6.21}$$

If $V_{in} = 40$kV and $V_{out} = 300$kV, n = 14.2, so a total of 15 transmission lines are needed to produce the required voltage .

6.3 Optimisation

In order to achieve the most efficient and highest energy output from the laser the operating conditions need to be optimised. These conditions vary from capillary to capillary and so this needs to be carried out each time a capillary is changed. There are four parameters which can be changed to optimise the laser output, the RF matching circuit impedances, the input voltage from the external power supply, argon pressure and the pulse timing. Optimum lasing usually occurs at a input voltage of 42kV and a pressure of approximately 300mTorr, with the high voltage pulse occurring $\approx 9\mu s$ after the pre-ionisation pulse. With these estimates in mind, the input voltage and pressure were varied (Figure 6.7) . The highest recorded output voltages were at a pressure of 0.253Torr of argon. At this pressure the highest laser output was recorded using an input voltage of 42kV. The pulse timing remained constant throughout, at $\Delta t = 9.6\mu s$, with the laser firing at a rate of 1Hz.

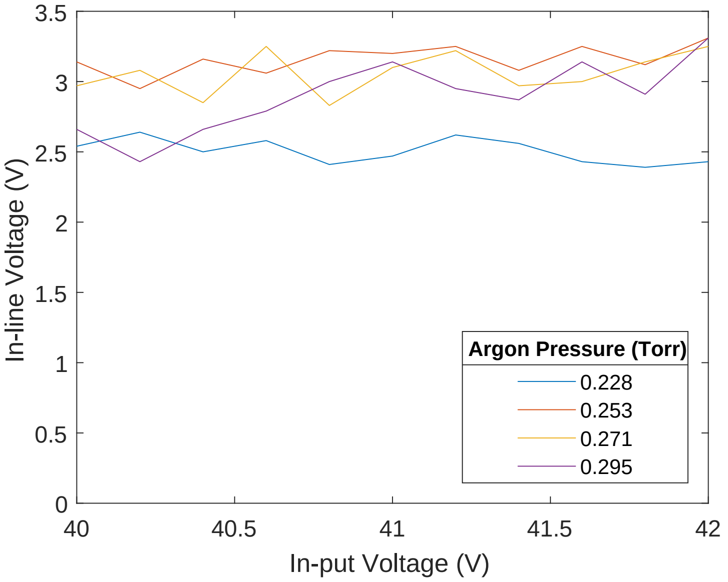

Figure 6.7: Laser pulse energy measured as voltage by the in-line detector as a function of the driving input voltage as a function of the background gas pressure in the capillary.

Following this the input voltage and argon pressure were kept constant and the pulse timings adjusted. The operating range for the high voltages pulse is $6\mu s < \Delta t < 12\mu s$. The high voltages pulse timings are changed by changing the Thyratron controller delay. The peak output measured by the in-line detector of $3.75V$ was recorded at a Thyratron trigger start time of $49006\mu s$ and end time of $49024\mu s$. This corresponds to the pulse occurring at $9\mu s$ after the start of the pre-ionisation pulse.

6.4 Optical Emission Spectroscopy

Although the capillary discharge laser output is in the EUV, the plasma produced in the capillary also emits optical radiation. Spectroscopy of the optical output from the plasma allows aspects of the capillary plasma to be measured and studied. The optical emission averaged in time and space is produced by the plasma present without significant Z-pinch compression and heating due to the high current pulse. Optical spectra of the plasma were taken at each stage of the ignition process, the RF, pre-ionisation, high voltage and then

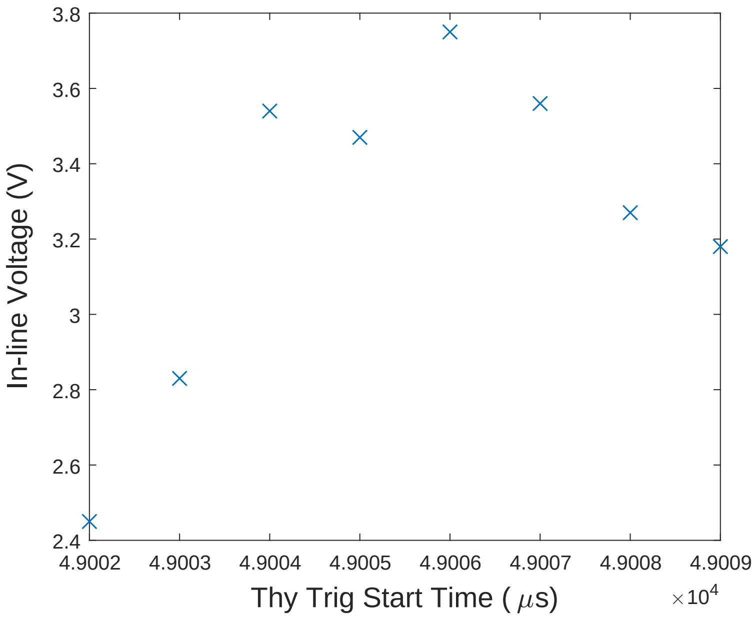

Figure 6.8: Laser output pulse energy as measured as voltage by the in-ine detectoras a function of the Thyrotron trigger timing

lasing plasma emission have been measured. This allows a measure of the evolution of the plasma to be recorded. The optical emission spectra can also show the presence of impurities present in the plasma. Impurities may cause the plasma to not function at optimum.

The spectroscopy was set up as shown in Figure 6.9. The optical light from the plasma passes through a window and was focused onto a fibre optic using a lens with focal length of 50mm, placed 60mm from the window. The fibre optic was connected to a Maya ocean optics spectrometer which uses a grating with a groove density of 300mm^{-1}. The wavelength range for light detection was $300 - 1000$nm. Ocean optics spectral suite software was used to calibrate the incident light as a function of wavelength [85]. The spectrometer was calibrated using an Ocean Optics LS-1-CAL tungsten halogen light source assuming an integration time of 1ms. Calibration allows for an absolute temperature measurement by calibrating the intensity as a function of wavelength.

The peaks in the spectra where identified using data given in the NIST database (Figure 6.10). If no argon ion was identified for a particular peak within a reasonable error range, that peak is identified as an impurity. Figure 6.10 shows peaks identified for neutral Argon (Ar I), singly ionised argon (Ar II) and hydrogen (H). The hydrogen peaks confirm that there are impurities present in the plasma. These could come from a vacuum leak,

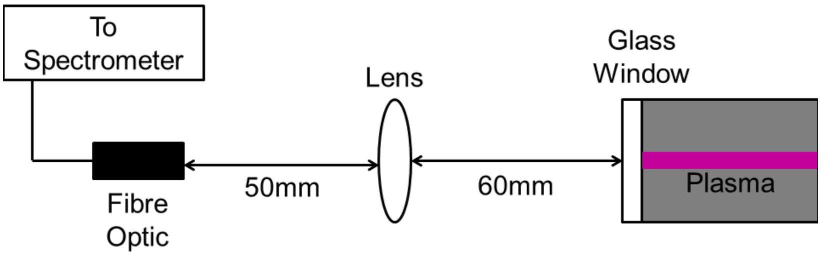

Figure 6.9: Experimental set-up to measure the spectral emission in the visible from the capillary plasma. A lens placed 600 mm from a glass window to the capillary discharge focuses plasma emission onto a fibre optic coupled to a visible grating spectrometer

water vapour or an oil leak. The three hydrogen lines represent the Balmer series where the dominant line at 656nm represents the first in the series (Hα) with peaks at 486nm (Hβ) and 434nm (Hγ).

The spectra of the plasma created with the RF and pre-ionisation pulse is shown in Figure 6.11. There are both hydrogen and oxygen lines present. We also see the increase in intensity of argon II lines as the pre-ionisation pulse is ionising the argon gas to a higher ionisation state than the RF pulse alone.

Figure 6.12 shows the spectrum and identified peaks for the high voltage pulse at an input voltage of 42kV. This spectra shows contaminations of hydrogen, carbon and oxygen. The carbon probably indicates an oil leak contaminating the capillary, while oxygen and hydrogen could be indication of oil leak or water vapour. The intensity of the Ar II peaks has increased with respect to the Ar I at the higher voltage as more argon is ionised.

The electron density and temperature of the plasma can be determined assuming a Boltzmann ratio of upper state populations between quantum states. For Boltzmann analysis to be true the plasma must be in local thermodynamic equilibrium (LTE). For a plasma to be in LTE the electron density must be great enough for the collisional transitions to domi-

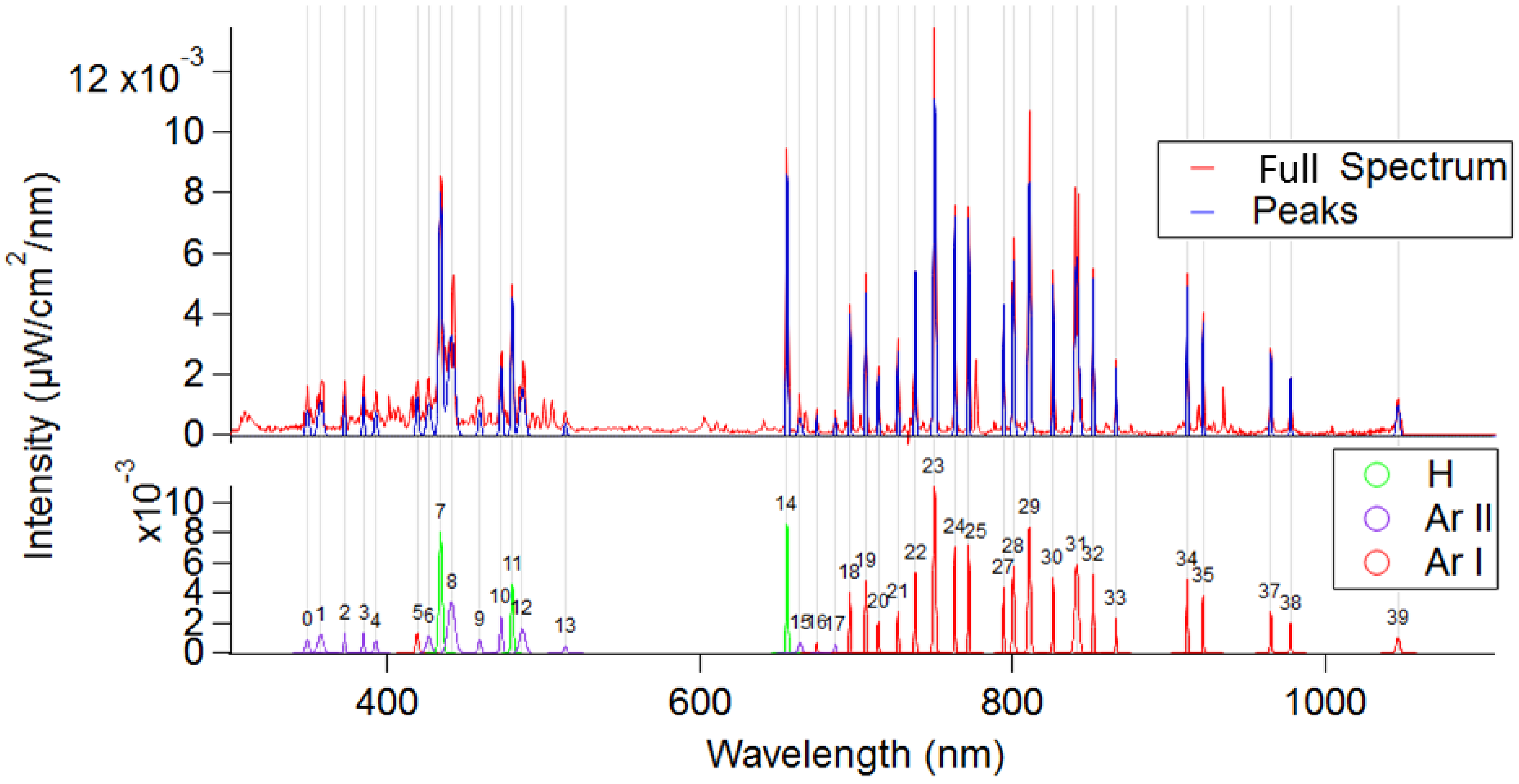

Figure 6.10: Spectrum of the RF plasma (red) with peaks identified in blue. Identified peaks of hydrogen (green), argon II (purple) and argon I (red).The lower plot shows spectral lines only after software removal of the continuum emission.

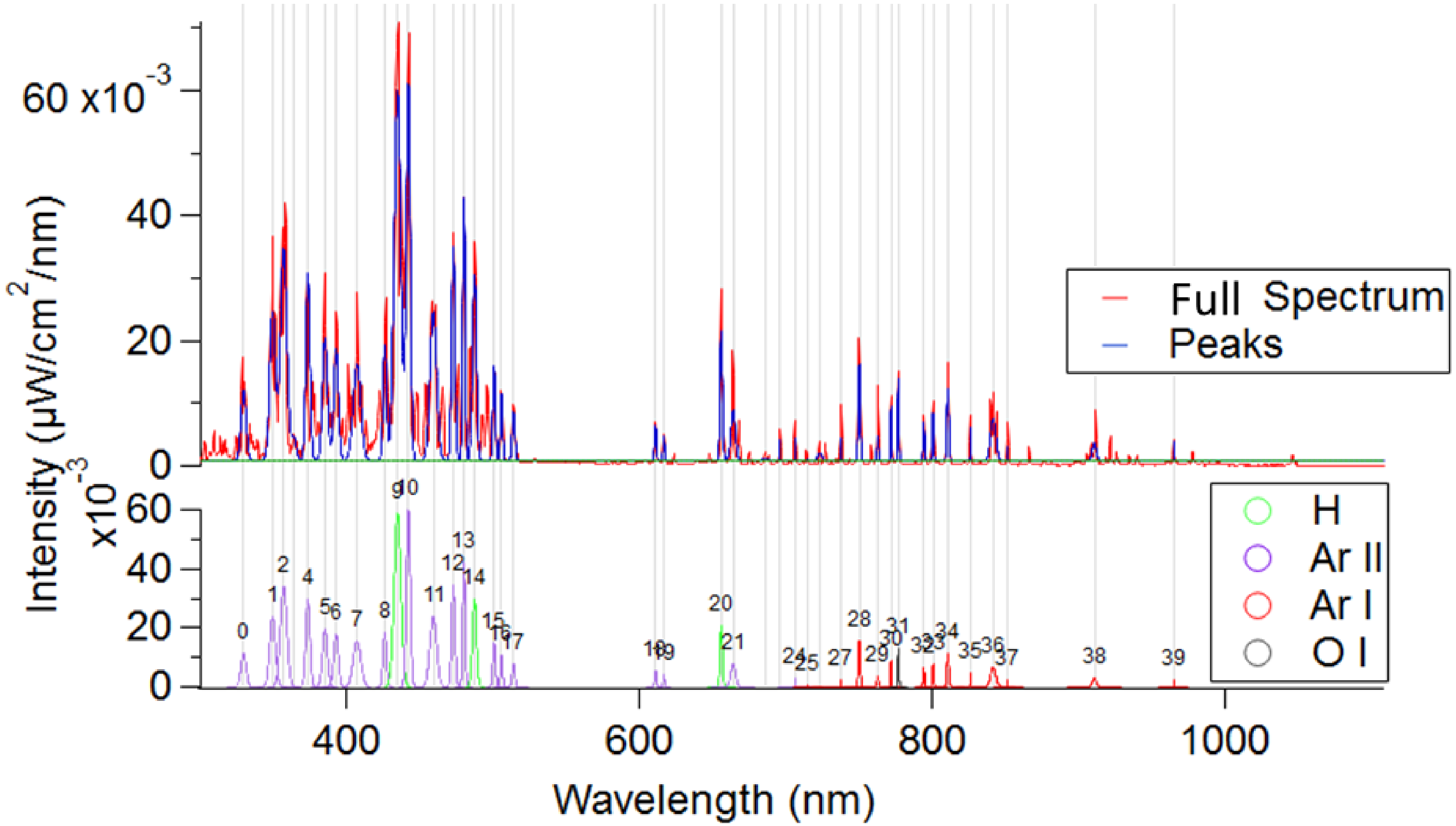

Figure 6.11: Spectrum of the pre-ionisation plasma (red) with peaks identifies in blue. Identified peaks of hydrogen (green), argon II (purple), argon I (red) and oxygen I (black) after software removal of continiuum and quasi-continuum emission (lower plot).

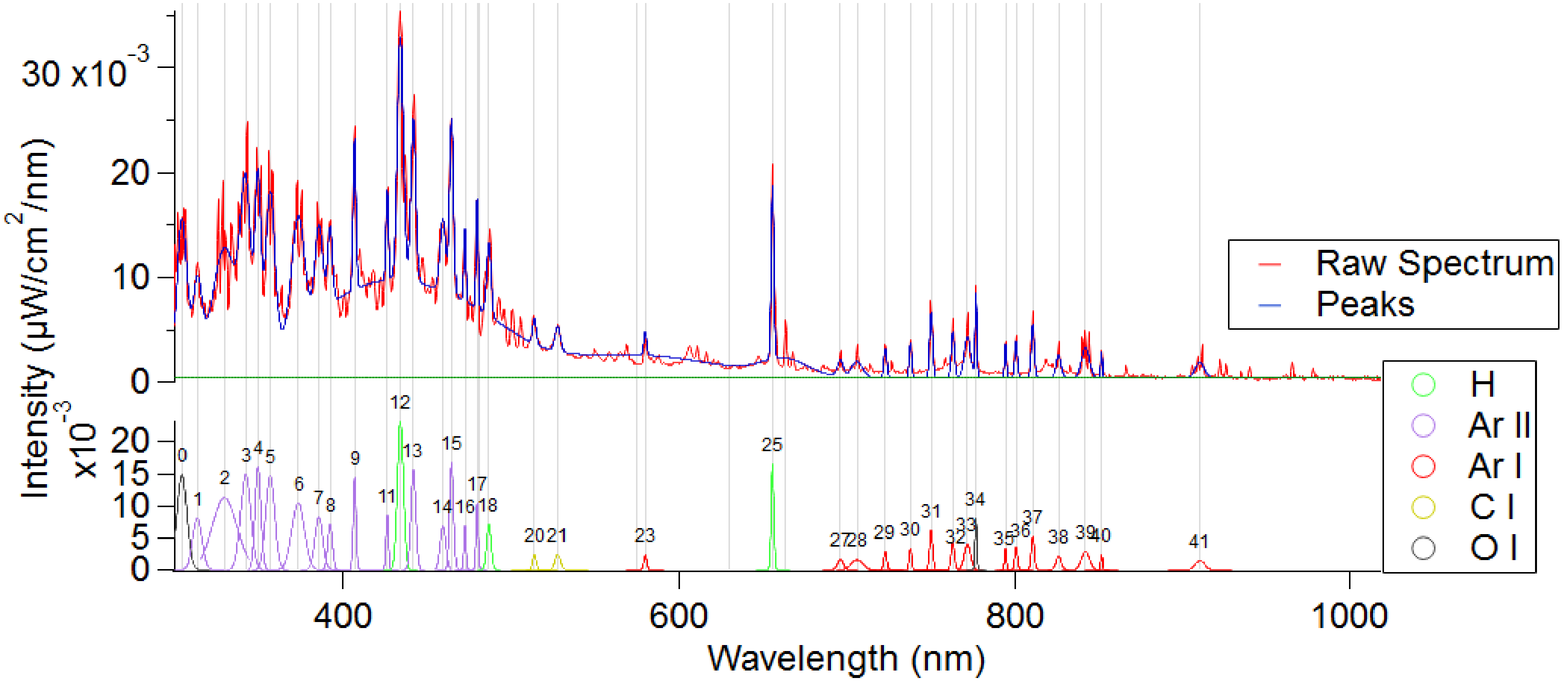

Figure 6.12: Spectrum of the high voltage plasma (red) with peaks idenified in blue. Identified peaks of hydrogen (green), argon II (purple), argon I (red), carbon I (yellow) and oxygen I (black) after software removal of continiuum and quasi-continuum emission (lower plot).

nate the radiative transitions between all states. This can be tested using the McWhirter condition,

$$n_e > 1.7 \times 10^{14}\sqrt{T_e}\Delta E^3 \tag{6.22}$$

where n_e is the electron density in cm-3, T_e is the temperature of the plasma and ΔE is the photon energy corresponding to a given transition. To apply LTE the electron density must be above a give value, which is determined by the temperature. The electron density can be determined using the Stark effect,

$$\Delta\lambda = 2w\frac{n_e}{10^{16}} \tag{6.23}$$

where $\Delta\lambda$ is the full width half maxima of a peak and w is the half width of the peak. The Stark effect is a broadening of spectral lines, occurring due to the ion energy levels being perturbed by an electric field created by free electrons in the plasma, hence is proportional to the electron density.

Using Equations (6.22) and (6.23) it was found that The pre-ionisation and high voltage plasmas satisfied conditions for LTE, where from Section 6.1.1.1 the radio frequency plasma has an electron density of $7 \times 10^{18}\text{m}^{-3}$ ($7 \times 10^{12}\text{cm}^{-3}$) and has not satisfied the McWhirter criterion by $1 \times 10^{15}\text{cm}^{-3}$. The pre-ionisation and high voltage plasmas have satisfied the requirements for LTE with an electron density of $8 \times 10^{15}\text{cm}^{-3}$ and McWhirter criterion of $5 \times 10^{15}\text{cm}^{-3}$.

For spectral lines terminating on the same lower quantum state, the line intensities I vary as

$$I \propto E_p g_k A_{ik} e^{-E_k/kT_e}, \tag{6.24}$$

if a Boltzmann distribution is assumed. Here E_p is the photon energy, g_i is the degeneracy of the upper state, A_{ik} is the transition probability and E_k is the energy of the upper state. We plot $ln(I/E_p g_k A_{ik})$ as a function of photon energy and take the gradient to find the electron temperature (Figure 6.13).

It is clear that there are significant errors in the determination of the electron temperature using Equation (6.24) associated with the small spread of photon energies. A novel technique was developed to determine the plasma temperature by analysing optically thick lines and modelling the plasma as a black-body [85]. It is well known that the maximum intensity from an optically thick plasma approaches the black-body intensity [37]. This means that

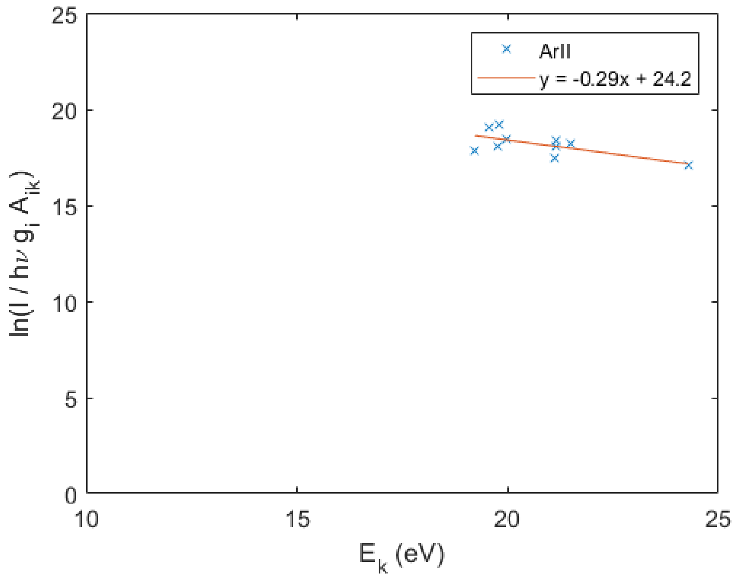

Figure 6.13: The logarithm of the intensity I of ArII spectral lines from the high voltage plasma divided by the photon energy, upper state degeneracy and transition probability as a function of the upper state energy. The fitted slope implies an electron temperature of 3.5eV.

optically thick emission lines will approach a black-body distribution. Using the most intense central lines the electron temperature can be determined using the Rayleigh-Jeans limit of black-body emission. A black-body distribution is given by Planck's law which describes the spectral density of electromagnetic radiation emitted by a black-body in thermal equilibrium at temperature T,

$$I = \frac{2hc^2}{\lambda}\frac{1}{e^{h\nu/k_BT\lambda}-1}. \tag{6.25}$$

At high temperatures the Rayleigh-Jeans law applies with,

$$I = \frac{2ck_BT}{\lambda^4}. \tag{6.26}$$

The most optically thick lines will appear as the highest intensities. Fitting to only the highest intensity lines and modelling these as black bodies by plotting $1/\lambda^4$ against intensity and taking a linear fit of the maximum intensities gives an estimate for the black-body value.

Plots of Rayleigh-Jeans method for the three ionisation stages for any Ar II lines are shown in Figure 6.14. Using the high voltage spectra a number of calculated temperatures given

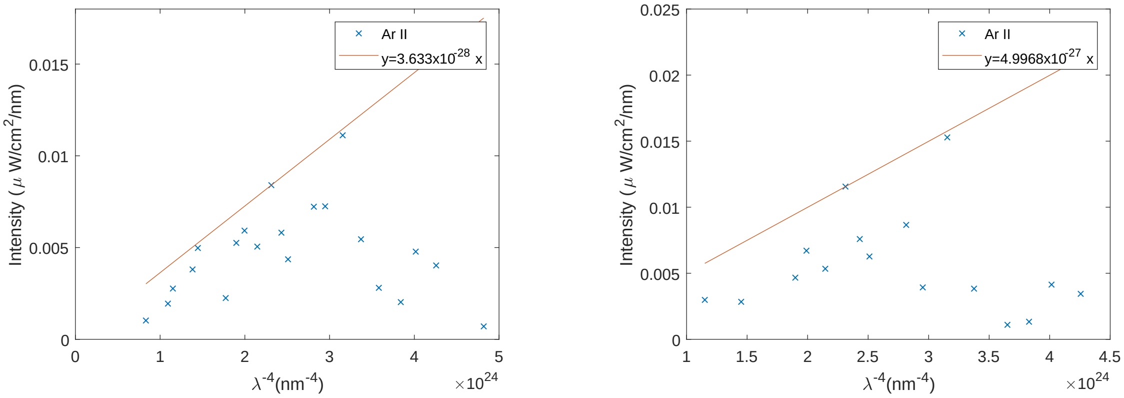

(a) Radio Frequency

(b) DC Preionisation

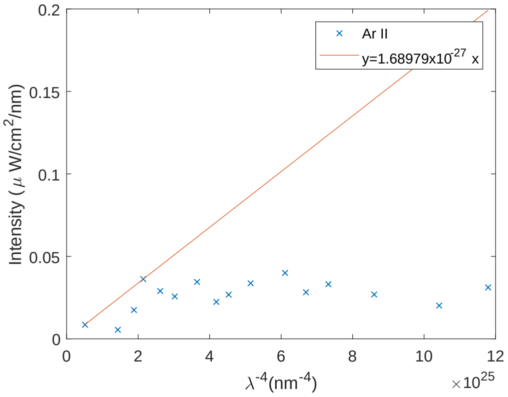

(c) High Voltage

Figure 6.14: Spectral intensities for ArII lines emitted from the capillary plasma at the three different ionisation stages as a function of the inverse fourth power of the spectral line wavelength.

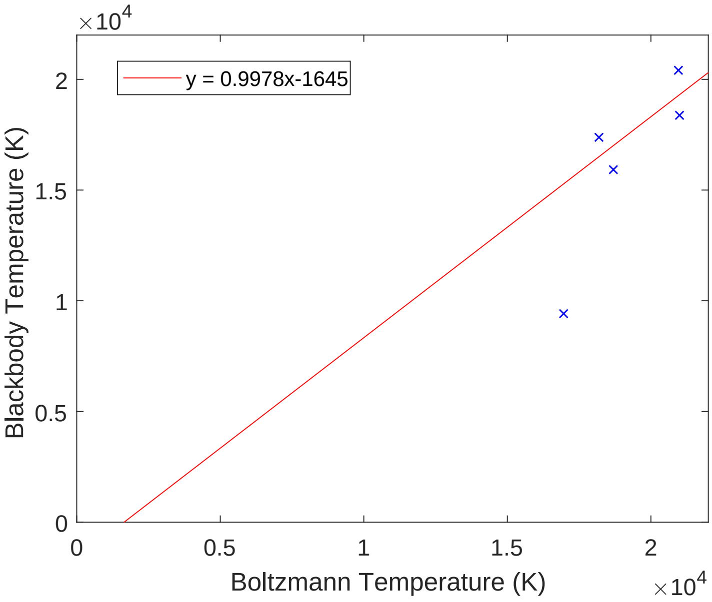

Figure 6.15: Comparison of temperstures determined using the Boltzmann and Rayleigh-Jeans methods.

by this method are compared to the temperatures given by the Boltzmann approximation (Figure 6.15). This gives a gradient of approximately 1 confirming the Rayleigh-Jeans as a valid method of determining plasma temperatures.

6.5 Laser Issues

Throughout the laser commissioning process a number of problems with the laser system were identified. This section details some of these problems, how they arose, and the solutions.

6.5.1 RF and Pre-ionisation Pulse Timings

The timings of these two pulses must be optimised to achieve the best possible laser output. The optimisation shows that the timings of the pre-ionisation pulse should be during the burst phase of the RF pulse (Figure 6.16). Although this gives the optimum laser output the extra power from the pre-ionisation pulse being deposited in the plasma is reflected into the dual-directional coupler and then the RF power supply. This increase in current has caused damage to the MOSFET component in the RF power supply. This causes the RF

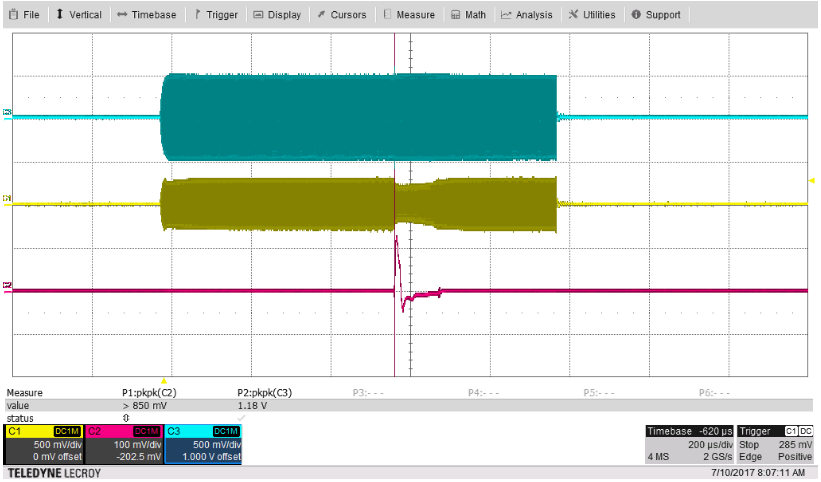

Measure	P1:pkpk(C2)	P2:pkpk(C3)	P3:- - -	P4:- - -	P5:- - -	P6:- - -
value	> 850 mV	1.18 V				
status		✓				

C1 DC1M 500 mV/div 0 mV offset
C2 DC1M 100 mV/div -202.5 mV
C3 DC1M 500 mV/div 1.000 V offset
Timebase -620 µs 200 µs/div 4 MS 2 GS/s
Trigger C1 DC Stop 285 mV Edge Positive
7/10/2017 8:07:11 AM

Figure 6.16: Pre-ionisation current (pink) measured using the Rogowski coil is shown at the the optimised timing concurrent with the burst phase of the RF pulse shown here with the forward RF power in blue and reflected RF power in yellow.

power supply to switch off and leave the pre-ionisation pulse still firing. This may cause the capillary to crack along the surface.

The MOSFET or metal-oxide-semiconductor field-effect-transistor acts as an insulated gate, the voltage of this determines the conductivity of the system. It is used to amplify or switch the signals from the RF power supply. The reason why they are used for this application is that they require a very low input current to control the load current. Therefore when the extra current from the pre-ionisation pulse is reflected back into the MOSFET it can be damaged [86].

To prevent this from happening, a protection circuit was built into the power supply and the pulse timings were altered in order to prevent the current from the pre-ionisation pulse being reflected into the power supply. The pulse timings have to be very carefully controlled in order to achieve this. They must be long enough after the burst phase of the RF pulse so as not to cause damage, but the RF plasma must still be ignited in order for the laser system to work . This leaves a window of 1μs to 4μs after the RF pulse for the pre-ionisation pulse to ignite (Figure 6.17).

The pulse again has to be optimised in order to achieve optimum lasing conditions for the laser. It was found that highest pulse energies occurred at 2μs after the RF pulse.

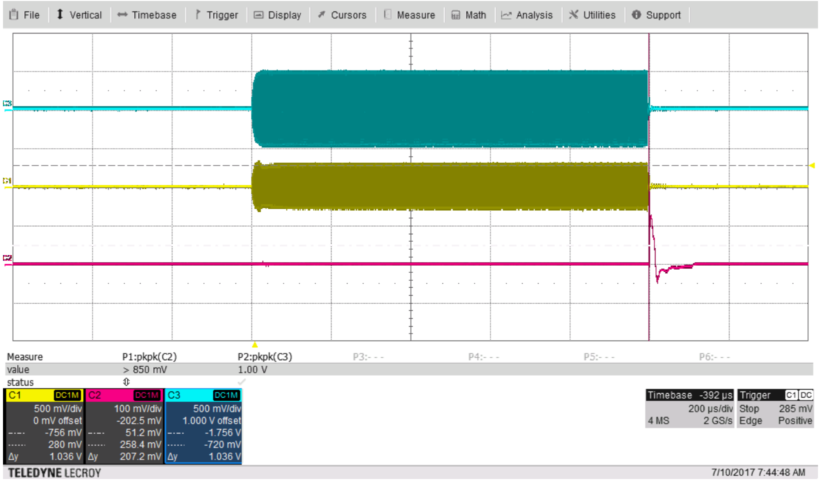

Measure	P1:pkpk(C2)	P2:pkpk(C3)	P3:- - -	P4:- - -	P5:- - -	P6:- - -
value	> 850 mV	1.00 V				
status	⇳	✓				

C1 DC1M		C2 DC1M		C3 DC1M	
	500 mV/div		100 mV/div		500 mV/div
	0 mV offset		-202.5 mV		1.000 V offset
-·-·-	-756 mV	-·-·-	51.2 mV	-·-·-	-1.756 V
······	280 mV	······	258.4 mV	······	-720 mV
Δy	1.036 V	Δy	207.2 mV	Δy	1.036 V

Timebase	-392 µs	Trigger	C1 DC
	200 µs/div	Stop	285 mV
4 MS	2 GS/s	Edge	Positive

7/10/2017 7:44:48 AM

Figure 6.17: Pre-ionisation current (pink) measured using the Rogowski coil is shown at the the optimised timing occuring 2μs after the burst phase of the RF pulse shown here with the forward RF power in blue and reflected RF power in yellow.

6.5.2 Transmission line breakdown

In Section 6.2 the formation of the electrical pulse along a Blumlein transmission line is discussed. It is important to avoid breakdowns in the transmission line as this can cause arcing and damage components. To avoid arcing in the high voltage components they are all submerged in transformer oil (MIDEL 7131) with a dielectric constant of 3.2 [87]. As with most other dielectrics the dielectric breakdown may be higher with the electric field in short pulses.

The electric field can be evaluated through Gauss's law,

$$\oint \vec{E}.d\vec{A} = \frac{Q}{\epsilon_0}, \tag{6.27}$$

where the electric field of a conducting cylinder of radius, r, and length, L, is given by

$$E = \frac{Q}{2\pi\epsilon_0\epsilon_r rL}, \tag{6.28}$$

ϵ_0 is the dielectric constant in a vacuum. Usually it is assumed that in a vacuum $\epsilon_r = 1$, however here the interface is to the transformer oil, therefore ϵ_r will be much higher than in vacuum.

In the capillary discharge laser the transmission line is fed through a cylinder which is part of the step-up transformer network. Here we can assume the transmission line (inner) rod has a radius of a and the outer cylinder has radius b. The potential between these is given as

$$V = \int_a^b E(r)dr = \frac{Q}{2\pi\epsilon_0\epsilon_r L}\int_a^b \frac{1}{r}dr = \frac{Q}{2\pi\epsilon_0\epsilon_r L}\ln\left(\frac{b}{a}\right) \tag{6.29}$$

Using this and Equation (6.28), the electric field can now be found in terms of the inner diameter, a,

$$E(a) = \frac{V}{a\ln(b/a)}. \tag{6.30}$$

We want to find the maximum ratio of the inner (a) and outer (b) cylinder ratio, letting $u = \frac{b}{a}$ we find the electric field of,

$$E_m = \frac{V}{b}\frac{u}{\ln(u)}, \tag{6.31}$$

where $E(a) = E_m$ if we assume the maximum electric field occurs in the inner rod. Differentiating this,

$$\frac{dE_m}{du} = \frac{V}{b\ln(u)}\left(1 - \frac{1}{\ln(u)}\right). \tag{6.32}$$

Equating this to zero gives the minimum possible value for E_m, which occurs at $u = \exp(1) = 2.7$.

The inner and outer cylinders of the capillary discharge laser have been manufactured to be, $a = 12.85$mm and $b = 39.94$mm, giving a value of $u = 3.11$. Using Equation (6.30), and assuming a voltage of 0.3MV, we find that the electric field in the inner cylinder is $E(a) = 2.059 \times 10^7$V/m. If the inner rod had been manufactured to the optimum radius the value for E_m would be $E_m = 2.042 \times 10^7$V/m. Both of these values for the maximum electric field are lower than the dielectric breakdown for the transformer oil, yet upon inspection arc points were found on the transmission line rod and outer cylinder (Figure 6.18). All of the

Figure 6.18: Arc points on inner rod of final transmission line in the Blumlein transmission line, caused by arcs through air bubbles trapped in the laser tank.

arc points were on the upper side of the rod, which indicates that there are air bubbles trapped in the transmission line. The dielectric breakdown value of air is approximately 3×10^6V/m so the electric field between the two rods would arc across this. It can never be confirmed that all air bubbles in the tank have been removed either by allowing the oil to rest for a few days before firing or by pumping the air bubbles out using an old vacuum pump, therefore an alternative solution to the problem is required.

The dielectric breakdown value of the material between the rod and the outer cylinder needs to be increased. This has been done by wrapping Kapton tape around the transmission line rod. Kapton tape has a minimum dielectric breakdown value of 1.2×10^8V/m [88], much higher than the transformer oil and higher than the required minimum value. The 17cm long rod was wrapped in 20cm wide Kapton tape to ensure even coverage (ends of the tape were trimmed to match the length of the rod). Three layers were applied ensuring no air bubbles were trapped in the tape to avoid arcing points forming.

6.5.3 High Voltage Rod Breakdowns

The stainless steel electrode which supplies the pulses to the plasma contained within the capillary is connected to the main laser tank via a rod which transmits the high voltage pulse.

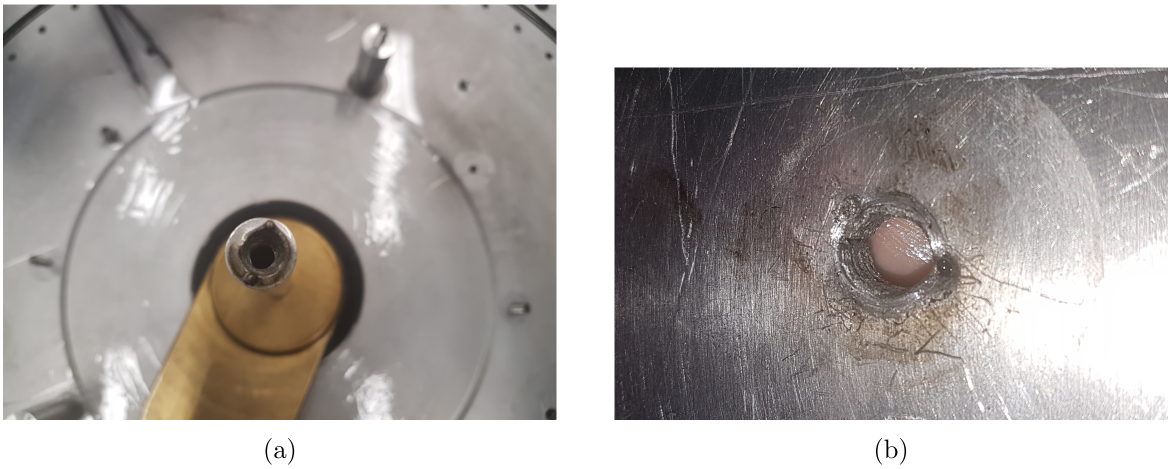
(a) (b)

Figure 6.19: Damage caused by arcing through the high voltage rod (a) High voltage rod with major arc damage to pins and surrounding area (b) Major arc damage to plate showing arc points at the pin inserts and to the thread where the rod is screwed in

This rod was designed with two pins inserted into a metal plate at the far end to prevent it from spinning when the electrode is screwed in and out during cleaning and capillary replacements.

Unfortunately these pins have acted as arc points for the high voltage pulse. The pulse has arced from the pins to the metal plate causing major structural damage. This was noticed when the electrode could not be removed from the rod as it has completely come away from the plate and was spinning in place

To prevent this from occurring again, the rod and plate were re-machined this time using two Teflon pins and a Teflon screw to hold the rod in place and to prevent it from spinning.

6.5.4 Capillary Blowouts

During the running of the capillary discharge laser on a number of occasions the ceramic capillaries have cracked, or arc points have been formed along the surface (Figure 6.20). When this happens the plasma column is no longer confined and because the capillary is the interface between oil and vacuum, the system becomes contaminated.

These capillary blow-outs occur due to contamination in the capillary. This is most likely caused by a loose fitting o-rings or damage to o-rings which are forming the seal between the vacuum system and transformer oil. Having a small oil leak into the capillary will prevent the

(a) (b)

Figure 6.20: Photographs of two different forms of capillary damage, (a) shows a capillary with arc point which has formed a small hole at one end and (b) shows a capillary which has had major arc damage broken into multiple peices. Arc points can be seen on some fractures.

RF plasma from igniting as the oil will cause impurities in the argon gas, if the RF plasma is already running when the leak occurs then the plasma will go out. This causes major problems as the high voltage pulses no longer have a conducting plasma column to pass through, therefore, they arc to the nearest conducting medium, which has suddenly become the oil which is contaminating the capillary. The damage is dependant on the voltage of the pulse which arcs, the damage seen in Figure 6.20a was caused by the pre-ionisation pulse, which has a voltage of approximately 8kV creating a small hole at the single arc point. The damage shown in Figure 6.20b is from the high voltage pulse (0.3MV) which has caused multiple arc points and fractured the capillary in multiple places.

There are two main methods of oil leaks like this happening. The o-rings forming the seal around the capillary are damaged or ill fitting, or the o-ring grove in the electrode is damaged. In the case of Figure 6.20b there was major damage to the electrode (Figure 6.21) where there were deep scratches in the sealing surface. An arc point on the electrode itself can also be seen, although this will have occurred after the leak due to the high voltage pulse arcing to the electrode.

6.5.5 Dielectric Constant of Transformer Oil

Transformer oil is used in the main tank and capillary nose sections of the laser in order to provide cooling and insulation to components. The oil used in the design and development of the laser was Opticool-A fluid, which is only available in the US. The dielectric constant

Figure 6.21: Photo of the scratches on the brass electrode which allowed for an arc point to form.

of the Opticool-A fluid is 2.09 at 25°C. This is important in the matching of the RF plasma as the transformer oil fills gaps between the capillary and the induction coil (Figure 6.1). the dielectric constant of the oil will affect the impedance matching to the plasma. The oil available in Europe is MIDEL 7131 transformer oil. The relative dielectric constant of this oil is 3.25 at 25°C. This means there is a signifigant difference in the fluid surrounding the capillary. The change in dielectric constant is enough to alter the RF matching significantly. This has caused issues in the ignition and stability of the plasma using the MIDEL oil, but this should be overcome by altering the RF matching network. The shunt capacitor can be changed in order to change the matching range. This can be done by replacing the capacitor depending on the oil, or by also making this a variable capacitor. Having a variable capacitor as the shunt capacitor allows a better match to be found as there are now two degrees of freedom available for the RF matching.

6.6 Conclusions

This chapter has reviewed how a capillary discharge laser can be run in the lab. The different ionisation stages have been discussed to show how to optimise the laser pulse. Diagnostics have been used to optimise the electrical pulses used to form the plasma and the lasing pulse. From this optical spectroscopy on the plasma column has been performed at each of the ionisation stages following the development of a novel technique of modelling the plasma as a black body in order to calculate the plasma temperature. Along with running the laser some of the most common issues with the laser maintenance and running have been presented along with solutions to these problems.

Now that the laser has been optimised and the methods for running it have been established experiments can now be performed according to preparations in Chapter 3 and Chapter 4.

Chapter 7

Laser Focusing and Ablation Experiments

This chapter presents details of experiments where matter is ablated from different target materials by the EUV laser pulse with focusing using on-axis spherical mirrors as described in Section 4.3. Both the scandium silicon multilayer mirrors and gold coated mirrors described in Chapter 3 are used.

The width and depth of the craters ablated by the focused EUV laser are dependant on the target material and the properties of the incident laser pulse. For large attenuation length, the target material attenuation length determines the depth of penetration of the laser radiation. However, it is shown that for target materials with a short attenuation length for the laser radiation that a travelling wave of ablation occurs as simulated by Rossall *et. al.* [55].

As discussed in Chapter 4 work by Aslanyan [54], and Rossall [55] have used off-axis spherical mirrors to focus, this will cause major spherical aberrations and coma leading to irregularities in the shape of the ablation craters. Artyukov [56] has also used an on-axis spherical mirror, however results in this case were measured using a scanning electron microscope (SEM). This gives a very good surface view of the ablation craters but the crater depths cannot be accurately measured using this method. This experiment will use an atomic force microscope to give a full 3D profile of the ablation crater allowing depths and widths of carters to be measured in more detail than previously.

7.1 Experimental Set-up

We have used spherical mirrors which focus the laser backwards (towards the laser) onto small targets. With small targets only a small fraction of the incoming laser beam is blocked by the target. The laser needs to be directed normally onto the spherical mirror and the mirror target positioning optimised. In the extreme ultra-violet, these alignment procedures are significantly more difficult than is applicable with visible lasers.

We explored two different procedures for focusing the EUV laser onto targets. Using a CCD camera two cross wires, one '×' and one '+', were placed in an estimated beam path. The laser is then fired onto the camera producing shadows of the two cross wires. When the centres of the two cross-wires overlap with the centre of the beam on the CCD, we know the laser is aligned (Figure 5.4).

Alternatively, two glass slides are spin-coated with PMMA and placed in the beam path. The laser is fired onto the first slide, which is then removed and the laser is fired onto the second slide. The two slides are then developed in a solution of 4-Methyl-2-Pentanone to show the beam position and replaced in their 'V' shaped holders, with a target taped onto the back of the slide marking the centre. A HeNe laser is then aligned through the centre of the targets .

The laser is aligned so that the beam passes through the in-line detector, which enables measurement of the beam energy throughout the experiment, using the calibrations given in Section 5.4. In order to calculate the energy incident onto the target the reflectivity of the mirror must also be taken into account. In Chapter 3, it was calculated that the reflectivity of the scandium/silicon mirrors is approximately 50% and the gold mirrors is approximate 10%. Allowing for manufacturing tolerances on the mirror surface roughness, these can be estimated as 45% and 8% respectively for a roughness of approximately 3nm. The laser energy is also reduced by the section of the target that is blocking the beam. Using the information from Figure 5.5, it has been calculated that the target blocks approximately 10% of the incident beam. Using these assumptions it is possible to have reasonably accurate measurements of the laser energy incident on the target.

Once the laser has been aligned the experiment can be set up as shown in Figure 4.5. The target is placed at an estimated focus point and a z-scan can be performed in order to find

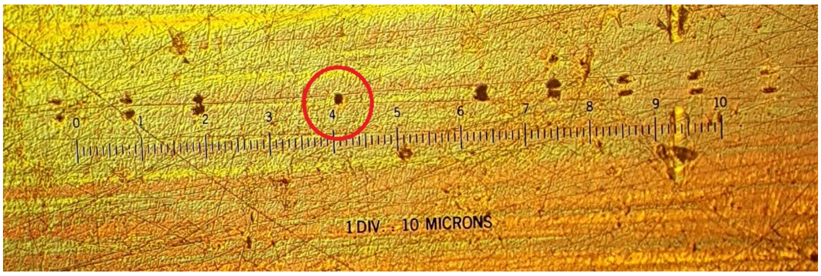

Figure 7.1: Gold target with ablation from z-scan firing 50 shots at each position moving the target in 100μm steps in the y-direction. The best focus is highlighed in red. The target was moved in z by 100μm between each ablation crater.

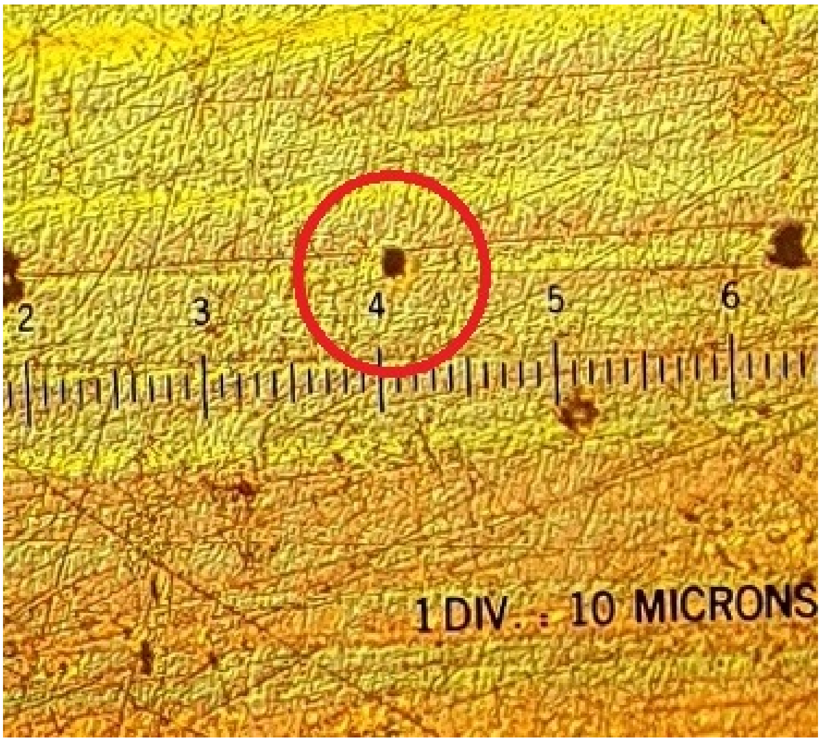

Figure 7.2: Magnified image of ablation crater at focus highlighted in red in Figure 7.1.

the exact point where the focal spot size is minimised.

An estimate of the focal point of the mirror can be determined, for example from Figure 7.1 where the laser is focused onto a gold target and coarsely scanned through the focus in steps of 100μm with 50 shots fired at each position. The image shows when out of focus there is destructive interference from diffraction around the target producing two ablation craters. However, at focus the focal spot becomes circular as marked in red on Figure 7.1. The change from near-field to far-field can also be seen from a 'mirror' of the diffraction pattern.

The target materials investigated are, aluminium, gold, copper and Poly-methyl methacry-

Target Material	l_a (μm)	ρ (g/cm^3)	H_a (J/cm^3)	F_a (J/cm^2)
Aluminium	0.41	2.7	29508	1.209
Copper	1.05×10^{-2}	8.9	44235	0.0464
Gold	5.98×10^{-3}	19.25	31704	0.0186
PMMA	2.4×10^{-2}	1.18	1061	0.00255

Table 7.1: Attenuation length (l_a), density (ρ), latent heat of ablation (H_a) and fluence required to ablate potential target materials (F_a)

late (PMMA). These have been chosen to give a range of material properties which can affect the ablation at EUV wavelengths. Combining the latent heat of fusion (L_f) and the latent head of vaporisation (L_v) gives the energy per unit volume (H_a) required to ablate a material from a solid state to a gas using $H_a = L_f + L_v$. The value of H_a then determines the minimum radiation fluence (F_a) required to ablate the target. We can estimate the fluence required to ablate the target by,

$$F_a \approx H_a \times l_a \tag{7.1}$$

Using the calculations from Section 4.3.2 we know the fluence provided by the Sc/Si multilayers is 4600J/cm^2 and for gold 740J/cm^2. Assuming a pulse duration of 1.2ns we can calculate the maximum focused intensities on the target surface of the Sc/Si multilayers and gold mirrors as 3×10^{12}W/cm^2 and 5×10^{11}W/cm^2 respectively assuming a minimum diameter of 1μm as calculated in Section 4.3. These maximum fluences meet the requirements to ablate all of the materials given in Table 7.1.

The surface profiles for each ablation crater can be measured using an atomic force microscope (AFM). An AFM does not make use of focusing light onto a surface like traditional microscopes, however an AFM uses a cantilever which interacts with the Van der Waals forces produced by the atoms on the target surface. In the measurement of the ablation targets the AFM is operated in tapping or oscillating mode. In this mode the cantilever is oscillated at its resonant frequency, when the probe approaches the sample surface, the oscillation changes due to the interaction between the probe and the Van der Waals forces from the sample. This causes a damping effect of the oscillation leading to a reduction in frequency and amplitude. The oscillations are measured by a force transducer and the scanner adjusts the z-height to maintain the probe at a fixed distance from the sample. This gives a detailed topographic scan of the sample surface and is the post appropriate surface measuring device for ablation targets as it will measure the full crater profile [89]. An AFM

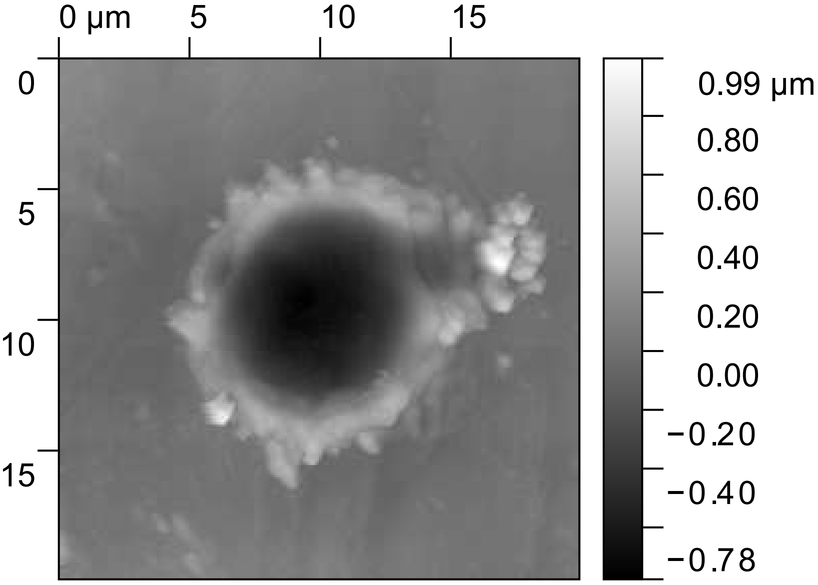

Figure 7.3: AFM surface image of the ablation crater produced from a single laser shot on a gold target

surface image of an ablation crater produced from a single laser shot on a gold target is shown in Figure 7.3. The 1D profile of the crater produced from this shot can be seen in Figure 7.5. Typical resolution of the AFM will provide images to within 150pm accuracy in the XY plane and to 35pm in height measurements.

7.2 Ablation Profiles

A scandium silicon multilayer mirror of radius of curvature 100mm was used to focus the radiation produced by the capillary discharge laser to an irradiance of approximately 2×10^{11}W/cm^2. A z-scan can be preformed, where one laser shot was fired in each position and the target is moved in step sizes of 1μm in the z-direction. The confocal length for the focusing geometry is approximately 3μm. A plot of the z-scans of aluminium, PMMA, copper and gold are shown in Figure 7.4. The focal point has been identified as the position with the deepest ablation crater, with the exception of copper where at the expected focal point there is a decrease in depth which may be caused by melting effects. The profiles for the ablation crater produced at the focus position using the scandium silicon multilayer mirror for each of the materials are shown in Figure 7.5.

The deepest ablation crater is seen in aluminium, and the shallowest in PMMA. This cor-

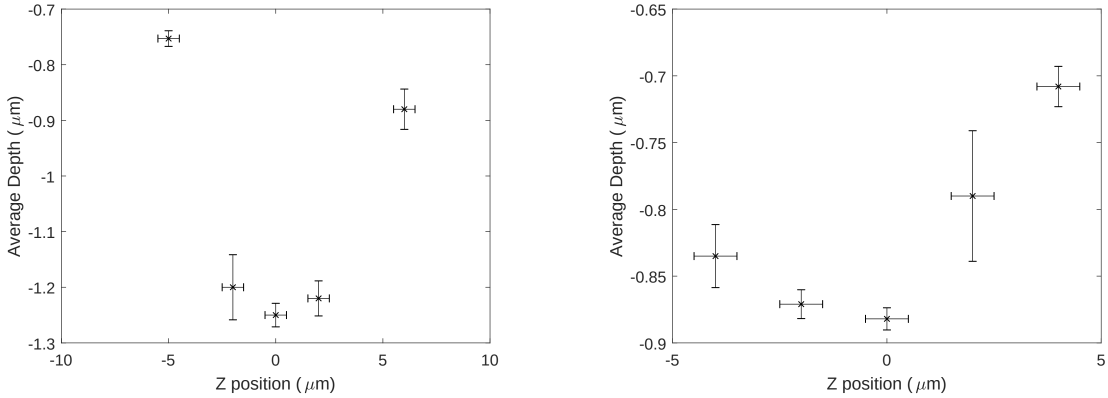

(a) Al

(b) Au

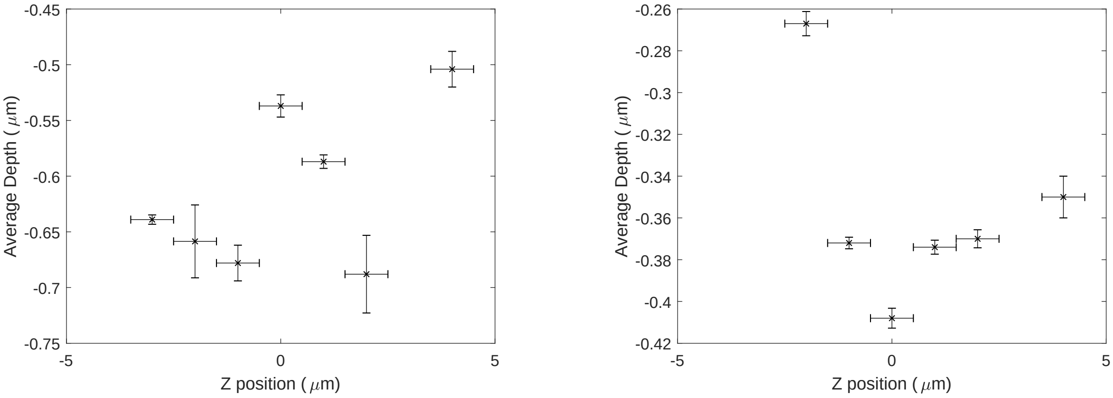

(c) Cu

(d) PMMA

Figure 7.4: Ablation crater depth as a function of focal position for single laser shots focused using a scandium silicon multilayer mirror onto targets of (a) aluminium, (b) gold, (c) Copper and (d)PMMA.

responds with the latent heat of ablation of the materials, where the higher latent heat of ablation gives a lower crater depth (Figure 7.6a). The attenuation length is also important (Figure 7.6b). A longer attenuation length allows radiation to penetrate to greater depths and to ablate grater depths of target.

The latent heat of ablation and the attenuation length affect the shape of the crater with the crater depth having a super Gaussian depth profile, $D(x)$

$$D(x) = A \exp\Big[-\Big(\frac{x^2}{w^2}\Big)^n\Big] \tag{7.2}$$

where w represents the width of the crater and n varies depending of the degree of departure from a simple Gaussian. We found that for aluminium $n = 3$, gold $n = 2$, and for copper

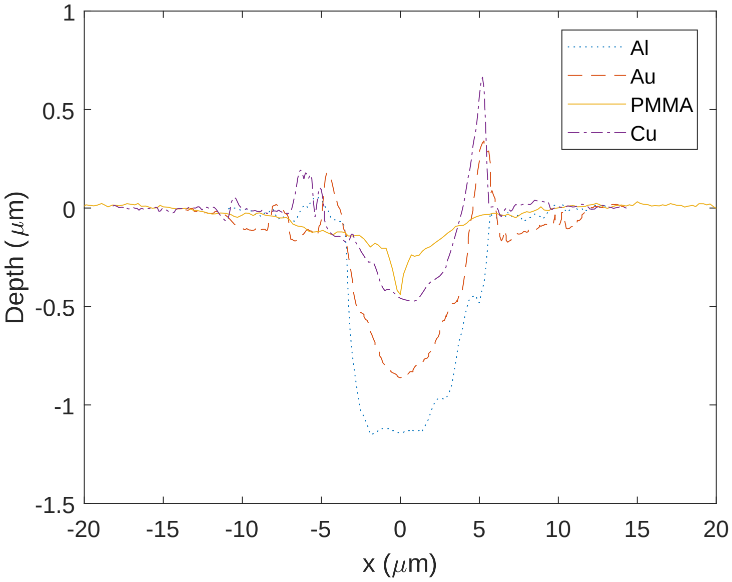

Figure 7.5: 1D Profiles of ablation craters from single shots in aluminium (blue), gold (red), PMMA (yellow) and copper (purple) focused using radius of curvature 100mm scandium silicon multilayer mirror at optimum focus.

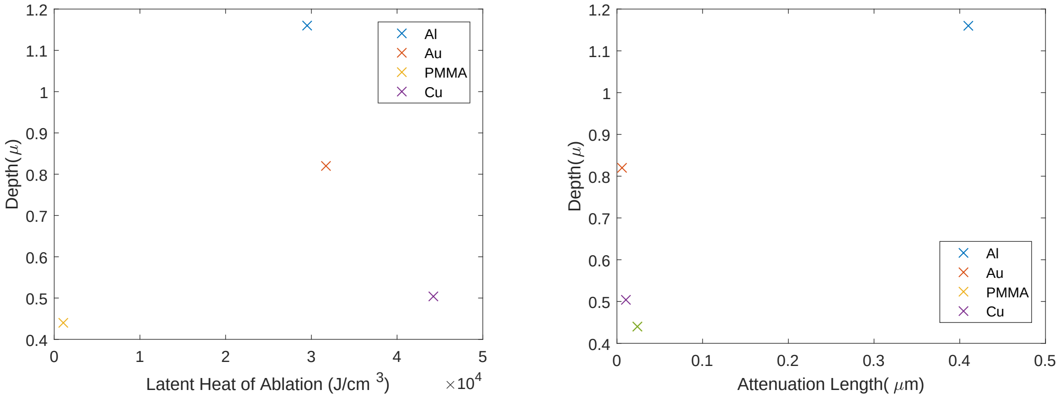

(a)

(b)

Figure 7.6: (a) Depth as a function of latent heat of ablation and (b) depth as a function of attenuation length for Al, Au, PMMA and Cu

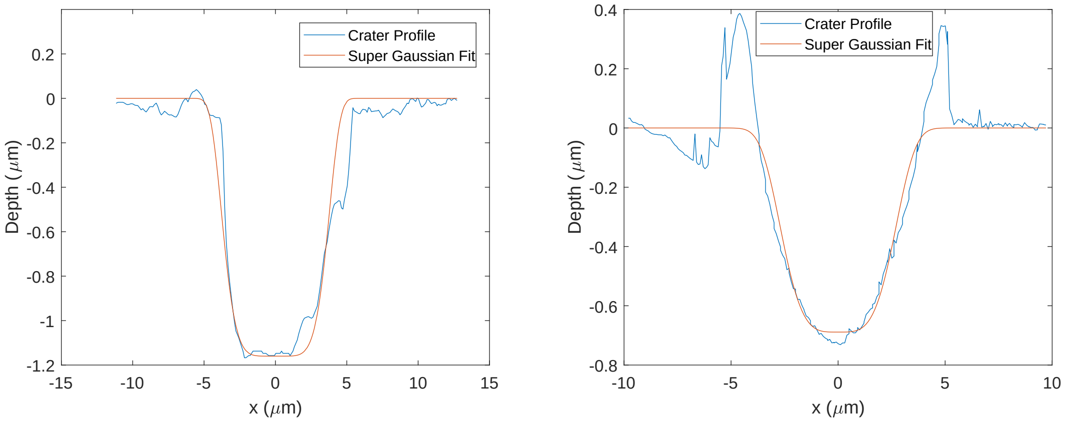

(a) Al (b) Au

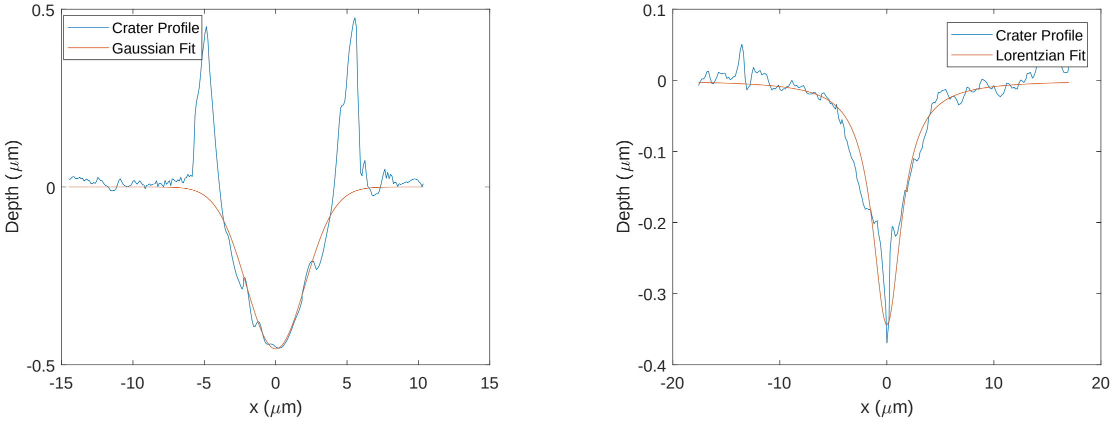

(c) Cu (d) PMMA

Figure 7.7: Ablation crater profiles for (a) aluminium with a super Gaussian fit where n=3, (b) gold with a super Gaussian it where n=2, (c) Copper with a Gaussian fit and (d)PMMA with a Lorentzian fit, focused using a scandium silicon multilayer mirror.

$n = 1$ after fitting Equation (7.2) to the profiles of Figure 7.5 (see Figure 7.7). The ablation depth for the PMMA targets were found to be best fitted with a Lorentzian spatial profile (Figure 7.7d).

The ablated widths correspond to w values of approximately 3μm. Such widths are significantly greater than the diffraction width with the focusing spherical mirrors at the EUV wavelength of 46.9nm. We can expect a diffraction width w_{diff} given by

$$w_{diff} \approx f_{no}\lambda \tag{7.3}$$

where f_{no} is the f number of the mirror. We estimate the diameter of the EUV beam at the

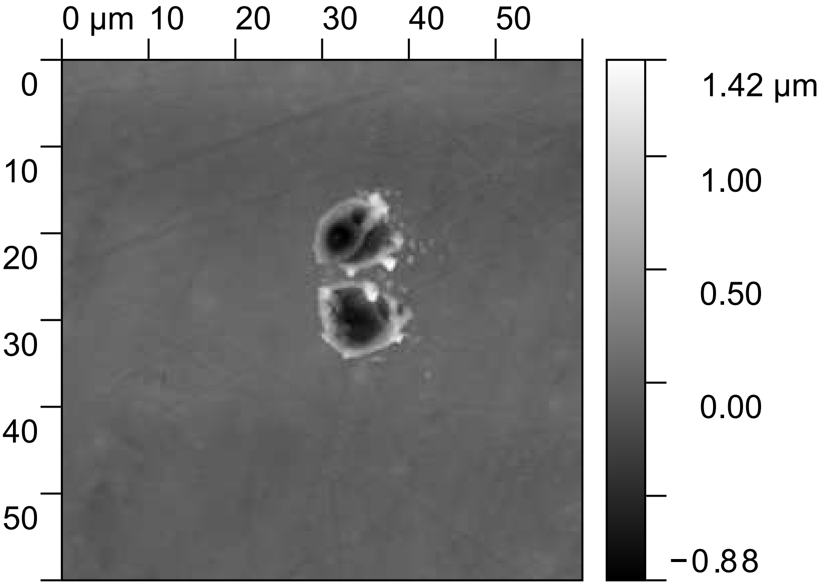

Figure 7.8: AFM surface image of ablation craters in Aluminium at approximately 100μm out of focus, showing a double spot caused by diffraction around the target before focusing using a 100mm radius of curvature scandium silicon multilayer mirror.

focusing mirror as 5mm, which with the focal length 50mm gives f_{no}=10 and a diffraction limited focal spot $w_{diff} \approx 0.2\mu$m.

Shots which were out of focus show evidence for destructive interference of the laser light due to diffraction of the incoming laser beam around the target (Figure 7.8). The distance of separation for the two ablation craters when out of focus is related to diffraction expected around the target width (d_{targ}) using [40]

$$\theta = \frac{\lambda}{d_{targ}} \tag{7.4}$$

where θ is the angle of diffraction of the beam. Using basic trigonometry the separation, Δl of the focus due to the diffraction is given by

$$\Delta l = 2L\theta \tag{7.5}$$

where L is the distance from the back of the target to the mirror and back to the target, which is twice the focal length of the mirror. Using λ=46.9nm, d=1mm and L=100.2mm the focal separation due to diffraction around the target for the incoming laser beam is Δl = 9.4μm. The full distance between the centre of the two ablation craters was measured as

9.4μm (Figure 7.8).

Gold mirrors with a radius of curvature of 100mm were also used to focus the capillary discharge laser, using the same methods as for the scandium silicon mirrors. However, due to the lower reflectivity of the gold mirrors there are some slight differences. Figure 7.9 shows the profiles of ablation craters in each of the four materials caused by 1 shot focused using the gold mirror. The most obvious difference is the difference in depth caused by the lower irradiance at approximately 5×10^{10}W/cm^2, resulting in shallower and narrower ablation craters. As with the scandium silicon mirrors the deepest craters can be seen in aluminium and the shallowest in PMMA. The craters produced in Figure 7.9 using the gold mirror to focus are slightly narrower than those produced by the scandium silicon multilayer mirrors (Figure 7.5). Assuming the focused laser profile incident on the target is Gaussian, the intensity is highest in the centre, so that the centre of the beam is easily over the ablation threshold. However, the Gaussian profile means intensity is reduced at the edges meaning the ablation threshold has not been met and the material here has not been ablated producing a narrower ablation crater.

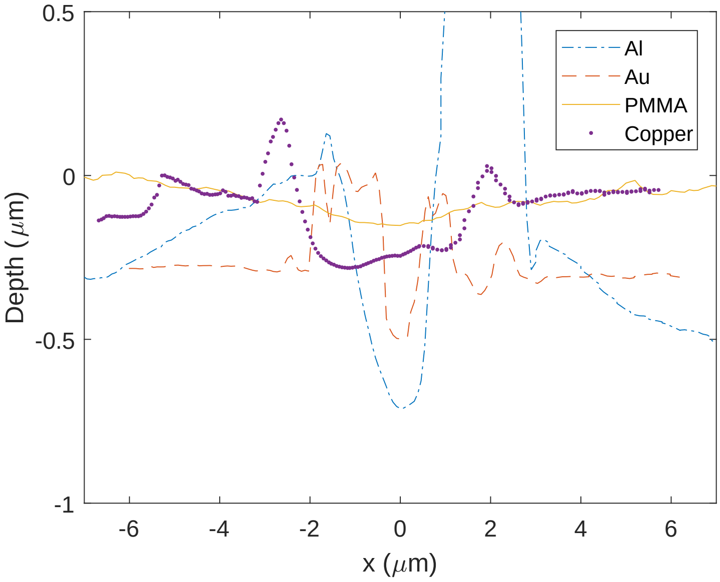

Figure 7.9: 1D Profiles of ablation craters in aluminium (blue), gold (red) PMMA (yellow) and Copper (purple) focused using gold mirror.

Due to the very shallow ablation craters with the gold mirror, measuring the craters for a single shot z-scan has proven difficult and so a z-scan has been performed where 20 shots were fired in each position (Figure 7.10). This allowed the focus position to be identified for this mirror to within 1μm.

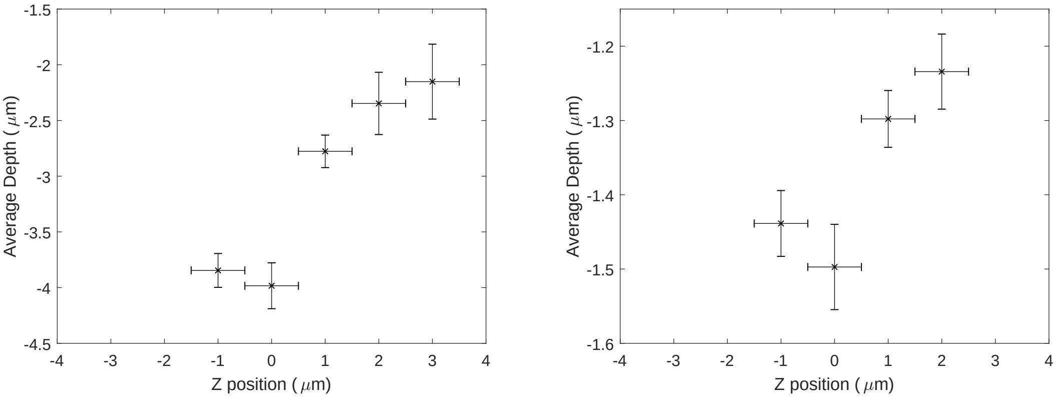

(a) Al (b) Au

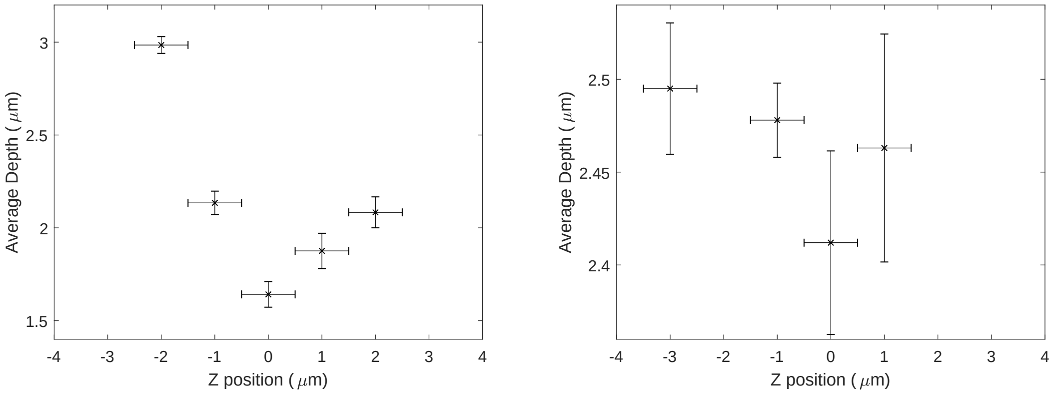

(c) Cu (d) PMMA

Figure 7.10: Ablation crater depth as a function of z-position for 20 laser shots focused using the gold mirror onto targets of (a) aluminium, (b) gold, (c) copper and (d) PMMA.

7.3 Ablation Rates

An expression for the depth of ablation for femtosecond optical laser pulses as a function of laser fluence has been developed by Gamaly *et al.* [90]. Gamaly *et al.* wrote that

$$D = \frac{l_s}{2} \ln\left(\frac{F}{F_a}\right) \tag{7.6}$$

where D is the depth of the ablation crater, l_s is the skin depth of the radiation, F is the laser fluence and F_a is the ablation threshold (see Table 7.1 for values). The factor 2 arises because optical radiation penetrates to approximately half the skin depth l_s [37]. Gamaly presents a method of using the material properties such as attenuation length and ablation threshold to estimate the depth of the ablation crater. Gamalys method has been developed for optical femtosecond lasers and so must be modified to apply to EUV laser systems. The expression has been modified to apply to EUV laser systems to give crater depth as,

$$D = l_a \ln\left(\frac{F}{F_a}\right) \tag{7.7}$$

where l_a is the attenuation length for EUV radiation in the solid target material and we initially assume that $F_a = l_a H_a$ with H_a as listed in Table 7.1. Figure 7.11 shows a comparison between the experimental values measured for the crater depth as a function of fluence with superimposed solid curves calculated using Equation (7.7). In the case of aluminium (Figure 7.11a), the results produced using Equation (7.7) give a crater depth higher than the experimentally measured depths. With short attenuation lengths as found for gold, copper and PMMA, it seems that there is sufficient energy in the laser pulse to ablate material over the skin depth during a shot duration of time less than the pulse duration and Equation (7.7) predicts ablation depths much less than measured (Figures 7.11b and 7.11c).

Aluminium has a large attenuation length (0.41μm) so that even with the 1.2ns EUV laser pulse, all heating and ablation largely occurs only in a target thickness corresponding to the attenuation length. In a sense, the interaction is similar to a short optical pulse interaction with a solid target where only half the skin depth of the laser in the target is ablated. However, for aluminium the experimental depths are shallower than those produced using Equation (7.7). This occurs because the ablated material absorbs much more energy than the values listed in Table 7.1. If the aluminium target is ionised by the incident radiation

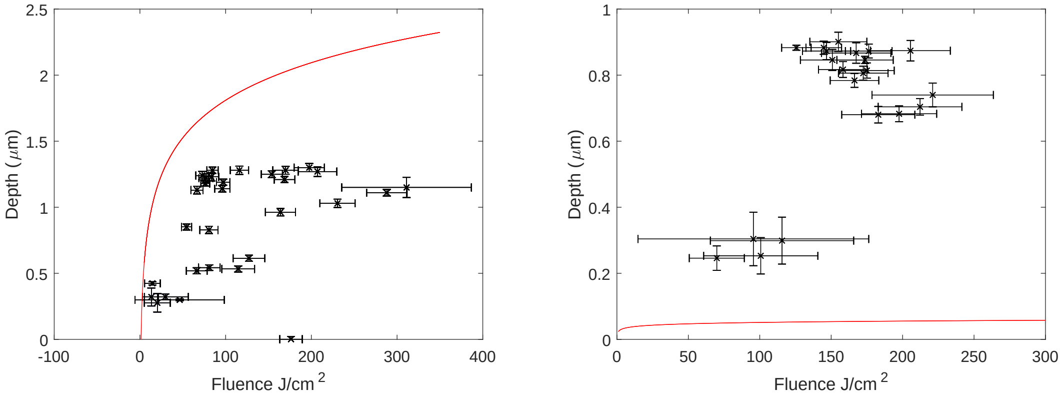

(a) Al (b) Au

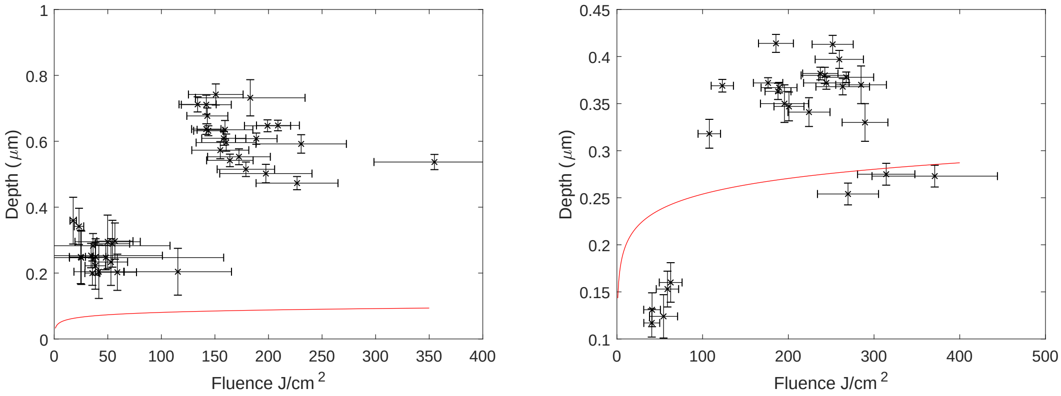

(c) Cu (d) PMMA

Figure 7.11: Experimental values for ablation crater depth as a function of laser fluence (black) and the ablation crater depth calculated using Gamalys theory (red) assuming F_a is determined by the latent heat of fusion and vapourisation, for (a)Aluminium, (b)Gold, (c)Copper, (d)PMMA. Focused using a scandium silicon multilayer mirror (high fluence) and a gold mirror (low fluence).

then the thermal energy of the ions, E_t and the ionisation energy, E_{ion} must be taken into account, this gives a total energy, $H_{ablation}$, associated with the energy content of the ablated plasma. We have

$$H_{ablation} = H_a + E_t + E_{ion}. \tag{7.8}$$

The thermal energy is given by

$$E_t = \frac{3}{2}\frac{(Z_i + 1)\rho}{Am_p}k_BT \tag{7.9}$$

where Z_i is the ion charge, ρ is the density, A is the atomic mass and m_p is the mass of a

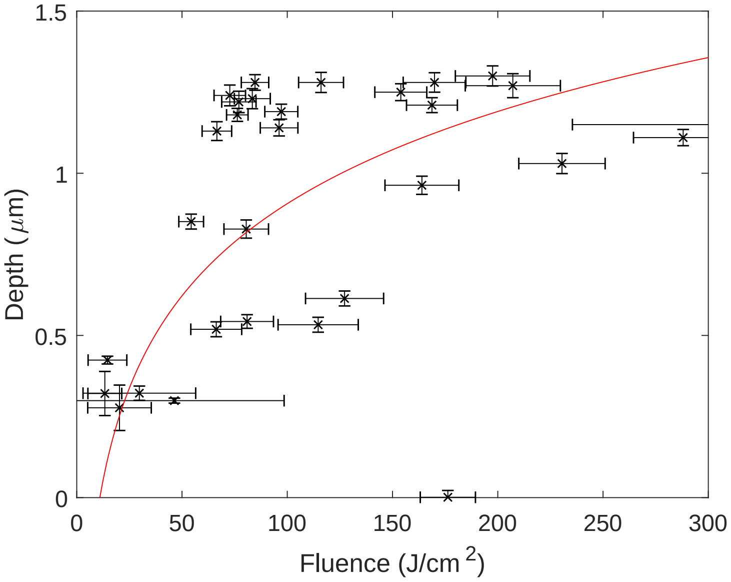

Figure 7.12: Depth of ablation crater as a function of laser fluence for an aluminium target using experimental values (black) and corrected Gamaly theory (red) assuming the ablating plasma is singly ionised.

proton. The temperature T for the evaluation of E_t and $H_{ablation}$ is assumed to be equal to the peak temperature associated with a determined ionisation as predicted by the FLYCHK code [91]. The ionisation energy is given by

$$E_{ion} = \Sigma E_i \Big(\frac{\rho}{Am_p}\Big) \tag{7.10}$$

where E_i is the ionisation energy for each degree of ionisation.

Using Equation (7.8) the degree of ionisation of aluminium can then be found by plotting Equation (7.7) using

$$F_a = H_{ablation} \times l_a \tag{7.11}$$

Figure 7.12 shows that Gamaly's theory of ablation applies to aluminium assuming a singly ionised plasma is formed by ablation with temperature T =2eV.

Using Equation (7.8) the depths of ablation, D, for the gold,and copper can be calculated using a method developed by Tallents *et. al.* [92]. This method is based on ablation caused by hard x-rays produced by a free electron laser. Although it is based on shorter wavelength radiation it does account for the pulse duration while also being based on the material properties. It is assumed that a small thickness Δx of the target is ablated in a time Δt by

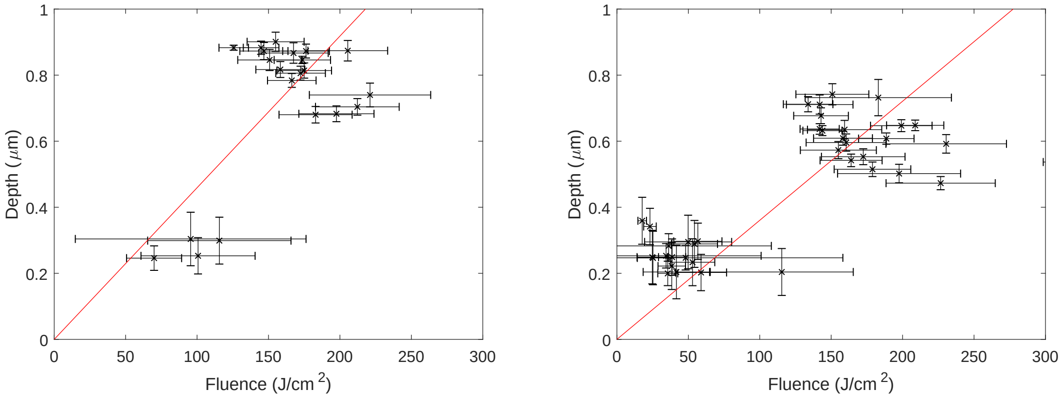

(a) Au 5th degree of ionisation

(b) Cu 4th degree of ionisation

Figure 7.13: Experimental values for depth of ablation craters (black) as a function of fluence with a fitted line corresponding to the ablation velocity model (red) assuming ionisation to Au^{5+} for gold (a) and Cu^{4+} for copper (b)

the focused laser intensity I so that

$$I\Delta t = H_{ablation}\Delta x \tag{7.12}$$

which gives a velocity of ablation in the target of

$$v = \frac{\Delta x}{\Delta t} = \frac{I}{H_{ablation}} \tag{7.13}$$

The depth D of ablation is obtained by the integration of the intensity in time. Using $F = \int I dt$ and $D = \int v dt$, we obtain

$$D = \frac{\int I dt}{H_{ablation}} = \frac{F}{H_{ablation}} \tag{7.14}$$

where F is the fluence. The velocity model can be used to plot the depth of ablation for gold and copper (Figure 7.13). The degree of ionisation of the ablated plasma can be found by adjusting the values of $H_{ablation}$ given by the FLYCHK code until the the velocity model fits the experimental data. We found that gold is ionised to Au^{5+} with T =23eV and copper to Cu^{4+} with T=10eV in order for Equation (7.14) to fit the measured depths shown in Figure 7.13.

The temperatures which have been evaluated from the experimental data using the FLYCHK code [91] for all materials are relatively low. These correspond to the warm dense matter

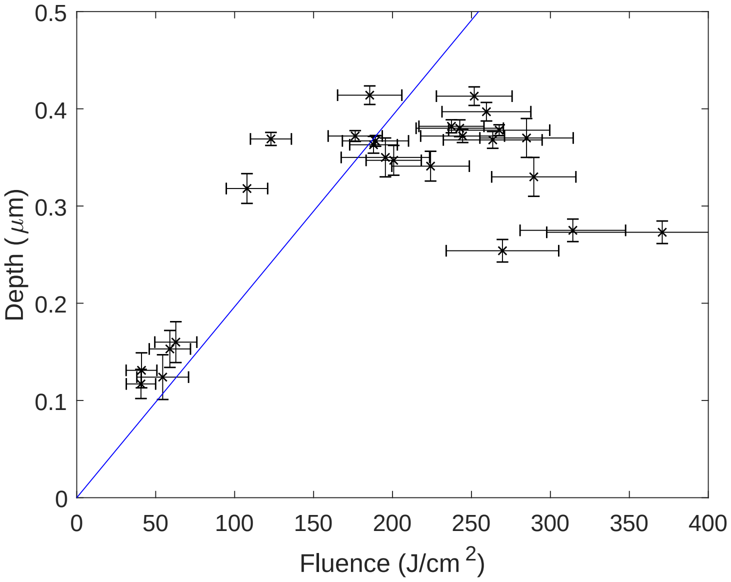

Figure 7.14: Experimental values for depth of ablation craters as a function of fluence (black) and a fitted line as a prediction of the ablation velocity model assuming C^{4+} (blue).

section of Figure 2.1, where solid densities in the range of 1 - 20 g/cm^3 and temperatures in the range of 2-50eV fall into the warm dense matter range.

7.3.1 Number of Shots

So far we have considered single shot ablation of the targets. Figure 7.15 shows a plot of depth of ablation craters in PMMA, Au, Cu and Al as s function of a number of shots fired at that position. The depth as a function of the number of shots is affected by the change in the surface of the target after the first shot when the laser is firing into the crater formed by the previous shot. Each shot ablates deeper into the pre-formed crater and ablates the crater walls to form a more square crater profile (Figure 7.16). This will also give an indication of the depth of field for the focus.

Figure 7.16 shows that for multiple shots the shape of the crater produced is very consistent. This indicates that the beam pointing does not vary on a shot-to-shot basis.

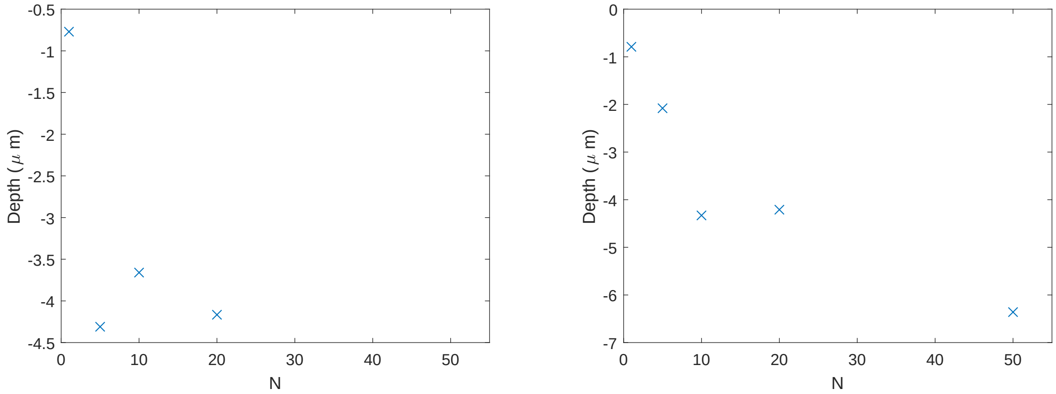

(a) Al

(b) Au

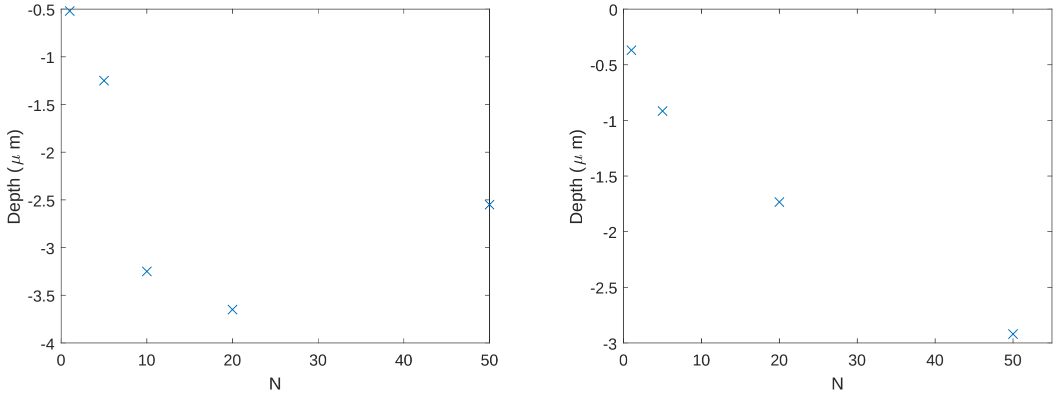

(c) Cu

(d) PMMA

Figure 7.15: Depth of ablation crater in (a)Aluminium, (b)Gold, (c)Copper, (d)PMMA, as a function of number of shots (N), focused using scandium silicon multilayer mirror.

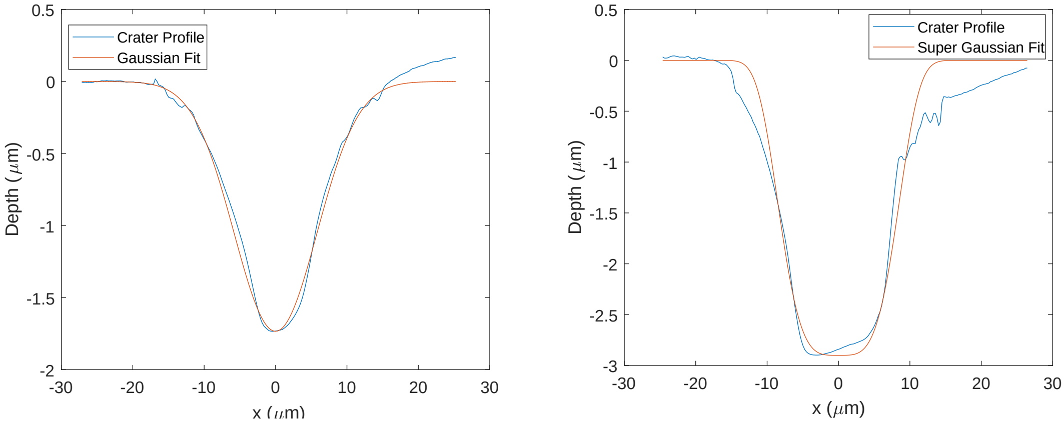

(a)

(b)

Figure 7.16: Ablation crater profiles in PMMA for (a)20 shots with a Gaussian fit and (b) 50 shots with a super Gaussian fit, focused using a scandium silicon multilayer mirror.

Chapter 8

Conclusions

This thesis presents a review of extreme ultraviolet radiation, including production methods, optical properties and focusing methods, and the set-up and initial experiments from an EUV capillary discharge laser. Initial experiments illustrate that capillary discharge lasers produce ablation from solid targets. A table-top sized capillary discharge laser was used which produces lasing output energies of approximately 50μJ in a 1.2ns duration laser pulse at a wavelength of 46.9nm. The laser is capable of operating at rates of up to 10Hz.

The optical properties of EUV radiation are well known at a wavelength of 13.5nm as this wavelength is now used in EUV lithography for the manufacture of semiconductor wafers. At 46.9nm new challenges are presented, particularly the absorption and reflectivity of focusing optics. Two possible materials are presented to use in focusing 46.9nm radiation. A scandium silicon multi-layer mirror can be optimised to give reflectivity of over 50%. Alternatively unprotected gold mirrors can give a reflectivity of approximately 10%.

These two mirror coatings can be used in a number of different ways to focus the EUV radiation. Previously tested methods such as Fresnel zone plates and off-axis spherical mirrors are compared to alternative focusing methods. The most promising focusing techniques used either a single spherical mirror on-axis or a Schwarzschild objective. Focusing has been modelled for both methods using the scandium silicon coating and the gold mirror coatings and found to enable irradiances ranging up to approximately 5×10^{11}W/cm^2 for gold mirrors to 5×10^{12}W/cm^2 for Scandium Silicon mirrors.

The EUV capillary discharge laser uses a neon-like argon plasma as the lasing medium produced through three pumping stages. The first stage creates a radio frequency (RF) plasma which is used to produce a lightly ionised plasma in a stable state. The parameters of the RF system have be used to estimate the electron density during the RF heating as $3 \times 10^{18}\text{cm}^{-3}$. The second pumping stage discharges a pre-ionisation pulse of approximately 40kV through the RF plasma. This ionises the argon ions to Ar^{8+} in preparation for the high voltage pulse. The high voltage pulse of 300kV is discharged through the plasma causing a radial z-pinch and lasing of the neon-like argon to produce radiation at 46.9nm. Various plasma parameters have been measured and inferred from this process such as the plasma current flow of approximately 40kA and an electron temperature of 50eV. A study of the optimisation of the laser output by varying input parameters and pulse timings has given an optimised pulse capable of producing energies of approximately 50μJ. Characterisation of each of the pumping stages has been performed by measuring optical spectra. The spectra produced have allowed the development of a novel technique for determining the plasma temperature by modelling the emission at the centre of optically thick spectral lines as a black-body. This technique gave an average electron temperature of 16000K to 21000K or 1.4eV to 1.8eV for the lasing medium plasma over all the pumping stages.

Experiments in the ablation of solid targets of aluminium, copper, gold and PMMA were carried out. The laser was focused using a single spherical mirror reflecting back onto a target. The ablation craters for each of the materials have been studied for both scandium silicon and gold coated mirrors. The craters were measured using an atomic force microscope (AFM) which interacts with the van der Waals force in the surface of the material to produce 3D images of the target surface. The ablation craters were used to determine the diameter of the laser focal spot and the effects of diffraction out of focus were also studied. It was found that the depth of ablation crater can be linked to the attenuation coefficient, where a higher attenuation coefficient gives deeper ablation. The calculation of the latent heat of ablation has been modified to include terms for the thermal energy of the ions and for the ionisation energy. Using the revised latent heat of ablation, it was found that aluminium which has the longest attenuation length can be modelled using a theory for femtosecond optical lasers developed by Gamaly *et. al.* [90]. The gold and copper have been modelled by an ablation velocity theory developed by Tallents *et. al.* [92], predicting the plasma ionisation to be Au^{5+} and Cu^{4+}. PMMA was modelled using the velocity method and POLLUX simulations. It was fund that the experimental depths as a function of laser fluence gives a reasonably good match to the results produced by the POLLUX simulations. The models have allowed an estimate of the electron temperature by assuming the achieved ionisation is equal to the peak temperature associated with a determined ionisation as predicted by the FLYCHK code [91]. The temperatures calculated (2-23eV) are within the range for warm dense matter.

The work has lead to a development in the understanding of the physics of an extreme ultraviolet capillary discharge laser and applied this to achieving ablation of solid targets. A novel technique of determining the plasma temperature by modelling the plasma as a black body has been described and compared to the well known Boltzmann temperature. Experiments have been performed to study the ablation of aluminium, gold, copper and PMMA targets. Results show that focusing can be readily achieved to give crater depths of approximately 1.2μm in aluminium and 0.4μm in PMMA in a single shot. The work has also shown how material properties effect the ablation of solid targets.

The work presented in this thesis may be developed further by using a Schwarzschild focusing objective to achieve a sub-micron focal spot diameter and irradiance of up to 5×10^{13}W/cm^2. Other materials for mirror coatings may also be investigated and it should be possible to extend the work to study emission waves in gas targets. Extending the range of target materials to include more non-metal materials and materials with higher attenuation lengths in order to confirm the theories presented. EUV spectroscopy can be carried out to characterise the different ionisation stages of the plasma column in the EUV wavelength range. This can be down using a gold coated flat field grating at grazing incidence. This can then be extended to investigate the spectra of the plasma produced on the target surface and further analysis can be done to characterise the warm dense plasma which is produced. The laser could be developed to have a longer capillary, this could increase the lasing energy, however it could also increase the divergence of the beam due to the increased refraction caused by the longer plasma column.

Appendix A

List of Publications

Papers

- G.J. Tallents, V. Aslanyan, A.K. Rossall, S. Wilson and M. Shahzad, *"The application of extreme ultra-violet lasers in plasma heating and diagnosis"*, SPIE Optical Engineering & Applications, 9589 (2015)
- A.K. Rossall, V. Aslanyan, S. Wilson, G.J. Tallents, *"Generation of strongly-coupled plasma using Argon-based capillary discharge lasers"*, SPIE Optical Engineering & Applications, 9589 (2015)
- G.J. Tallents, S.A. Wilson, A. West, V. Aslanyan, J. Lolley, A.K. Rossall, *"The creation of radiation dominated plasmas using laboratory extreme ultra-violet lasers"*, High Energy Density Physics, 23 (2017)
- T. Page, S.A. Wilson, J. Branson, E. Wagenaars, G.J. Tallents, *"Plasma temperature measurements using black-body radiation from spectral lines emitted by a capillary discharge"*, Journal of Quantitative Spectroscopy & Radiative Transfer, 220 (2018)
- S.A. Wilson, J. Lolley, E. Solis Meza, C. Beardall, H. Bravo, C.S. Menoni, J.J. Rocca, G.J. Tallents, *"Extreme ultra-violet interaction and ablation of solids"* (2018) prepublication

Oral Presentations

- S.A. Wilson, G.J. Tallents, " *Commissioning and Initial Experiments of an EUV Capillary Discharge Laser"*, OSA, High-brightness Sources and Light-driven Interactions, (2018)

Poster Presentations

- S.A. Wilson, G.J. Tallents, *"Focusing of an Extreme Ultraviolet laser using a Schwarzschild Objective"*, Central Laser Facility Christmas Meeting (2015)
- S.A. Wilson, A.West, J.Lolley, G.J. Tallents, *"Extreme Ultraviolet lasers"*, Central Laser Facility Christmas Meeting (2016)
- S.A. Wilson, A.West, J.Lolley, G.J. Tallents,*"Compact EUV Capillary Discharge lasers"*, CIM-Laser One Day Conference (2017)
- S.A. Wilson, A.West, G.J. Tallents, *"Capillary Discharge Laser set-up and initial results"*, European Physical Society Conference on Plasma Physics (2017)
- S.A. Wilson, G.J. Tallents, *"EUV ablation of Solid Targets"*, Central Laser Facility Christmas Meeting (2017)
- S.A. Wilson, G.J. Tallents, *"EUV ablation of Solid Targets"*, 45th IOP Plasma Physics Conference (2018)

List of References

[1] D. Attwood. *Soft x-rays and Extreme Ultraviolet Radiation.* Cambridge University Press, Cambridge, 1999.

[2] B. Henke, E. Gullikson, and J. Davis. X-ray interactions: Photoabsorption, scattering, transmission and reflection at E=50-30,000eV, Z=1-92. *Atomic data and nuclear data tables*, 54:181, 1993.

[3] R. Dendy. *Plasma Dynamics.* Oxford Science Publications. Clarendon Press, 1990.

[4] F. F. Chen. *Plasma Physics and Controlled Fusion.* Plenum Press, New York, second edi edition, 1984.

[5] J. Chalupský, et al. Characteristics of focused soft X-ray free-electron laser beam determined by ablation of organic molecular solids. *Optics Express*, 15(10):6036, 2007.

[6] A. Ng. Warm Dense Matter: The missing link between condensed matter and plasma. *IEEE*, (ii):11, 2012.

[7] D. Riley. Generation and characterisation of warm dense matter in the laboratory. *Plasma Physics and Controlled Fusion*, 60, 2018.

[8] R. W. Lee, et al. Plasma-based studies with intense X-ray and particle beam sources. *Laser and Particle Beams*, 20(3):527, 2002.

[9] David Salzmann. *Atomic Physics in Hot Plasmas.* Oxford University Press, New York, 9th edition, 1998.

[10] S. Ichimaru. Strongly coupled plasmas: High-density classical plasmas and degenerate electron liquids. *Reviews of Modern Physics*, 54(4):1017, 1982.

[11] Y. V. Arkhipov and A. E. Davletov. Screened pseudopotential and static structure factors of semiclassical two-component plasmas. *Physics Letters A*, 247(October):339, 1998.

[12] G. Gregori, S. H. Glenzer, and O. L. Landen. Strong coupling corrections in the analysis of x-ray Thomson scattering measurements. *J. Phys. A*, 36(22):5971, 2003.

[13] F. Perrot and M. W. C. Dharma-Wardana. Spin-polarized electron liquid at arbitrary temperatures: Exchange-correlation energies, electron-distribution functions, and the static response functions. *Physical Review B - Condensed Matter and Materials Physics*, 62(24):16536, 2000.

[14] S. Hooker and C. Webb. *Laser Phsysics*. Oxford University Press, 2010.

[15] C. Elton, Raymond. *X-ray Lasers*. Elsevier Inc., 1990.

[16] T. Hahn, et al. Broadband xuv polarimetry of high harmonics from plasma surfaces using multiple fresnel reflections. *Applied Physics B: Lasers and Optics*, 118(2):241, 2015.

[17] Z. Chang, A. Rundquist, H. Wang, M. M. Murnane, and H. C. Kapteyn. Generation of Coherent Soft X Rays at 2.7 nm Using High Harmonics. *Physical Review Letters*, 79(16):2967, 1997.

[18] P. Antoine, A. L'Huillier, and M. Lewenstein. Attosecond pulse trains using high-order harmonics Attosecond Pulse Trains Using High – Order Harmonics. *Physical Review Letters*, 77(7), 1996.

[19] A. A. Sokolov and I. M. Ternov. Synchrotron Radiation. *Journal of Chemical Information and Modeling*, 53(9):1689, 2013.

[20] B. W. J. McNeil and N. R. Thompson. X-ray free-electron lasers. *Nature Photonics*, 4(12):814, 2010.

[21] S. V. Milton, S. V. Milton, E. Gluskin, N. D. Arnold, C. Benson, W. Berg, S. G. Biedron, M. Borland, Y. Chae, and R. J. Dejus. Exponential Gain and Saturation of a Self-Amplified Spontaneous Emission Free-Electron Laser. 2037(2001):2037, 2012.

[22] W. Ackermann, et al. Operation of a free-electron laser from the extreme ultraviolet to the water window. *Nature Photonics*, 1(6):336, 2007.

[23] G. J. Tallents. The physics of soft x-ray lasers pumped by electron collisions in laser plasmas. *J. Phys. D*, 36(15):R259, 2003.

[24] J. Nilsen, B. J. MacGowan, B. Luiz, and J. Moreno. Prepulse technique for producing low-Z Ne-like x-ray lasers. *Physical Review A*, 48(6):2677, 1993.

[25] W. L. Kruer. *The Physics of Laser Plasma Interactions.* Westview Press, 2003.

[26] G. J. Pert. Optimizing the performance of nickel-like collisionally pumped x-ray lasers. II. Lasers for the wavelength range 50-100. *Physical Review A - Atomic, Molecular, and Optical Physics*, 75(2):1, 2007.

[27] B. A. Reagan, C. Baumgarten, E. Jankowska, H. Chi, H. Bravo, M. Pedicone, L. Yin, H. Wang, C. S. Menoni, and J. J. Rocca. Scaling diode-pumped , high energy picosecond lasers to kilowatt average powers. 6:1, 2018.

[28] T. W. L. Sanford. X-ray Emission from a High-Atomic- Number z-Pinch Plasma Created from Compact Wire Arrays. *Sandia Report*, (March), 1996.

[29] M. K. Matzen. Z pinches as intense x-ray sources for high-energy density physics applications. *Physics of Plasmas*, 4(5):1519, 1997.

[30] J. H. Brownell, R. L. Bowers, K. D. McLenithan, and D. L. Peterson. Radiation environments produced by plasma z-pinch stagnation on central targets. *Physics of Plasmas*, 5(5):2071, 1998.

[31] M. G. Haines. The wire array Z-pinch: An efficient x-ray source for ICF and a new ion heating mechanism. *AIP Conference Proceedings*, 1154:37, 2009.

[32] T. W. Sanford, et al. Wire array Z-pinch insights for enhanced x-ray production. *Physics of Plasmas*, 6(5):2030, 1999.

[33] H. Bravo, B. T. Szapiro, P. W. Wachulak, M. C. Marconi, W. Chao, E. H. Anderson, C. S. Menoni, and J. J. Rocca. Demonstration of nanomachining with focused extreme ultraviolet laser beams. *IEEE Journal on Selected Topics in Quantum Electronics*, 18(1):443, 2012.

[34] S. Barnwal, et al. Characterization of the 46.9-nm soft X-ray laser beam from a capillary discharge. *Applied Physics B*, 117(1):131, 2014.

[35] B. Kettle, et al. Experimental measurements of the collisional absorption of XUV radiation in warm dense aluminium. *Physical Review E - Statistical, Nonlinear, and Soft Matter Physics*, 94(2):1, 2016.

[36] G. J. Tallents. The physics of soft x-ray lasers pumped by electron collisions in laser plasmas. *Journal of Physics D: Applied Physics*, 36(15), 2003.

[37] G. Tallents. *An introduction to the Atomic and Radiation Physics of Plasmas.* Cambridge University Press, 2018.

[38] G. J. Tallents, S. Wilson, A. West, V. Aslanyan, J. Lolley, and A. K. Rossall. The creation of radiation dominated plasmas using laboratory extreme ultra-violet lasers. pages 1–13.

[39] V. G. Kohn. On the Theory of Reflectivity by an X-Ray Multilayer Mirror. *Physica Status Solidi (B)*, 187(1):61, 1995.

[40] E. Hecht. *Optics.* Addison Wesley, 4th edition, 2002.

[41] F. Tamburini, G. Anzolin, G. Umbriaco, A. Bianchini, and C. Barbieri. Overcoming the Rayleigh criterion limit with optical vortices. *Physical Review Letters*, 97(16):1, 2006.

[42] E. Wolf. *Progress in Optics.* Elsevier, 2007.

[43] Q. Wang, X. Ma, X. L. Zhu, and S. F. Zhang. Observation of atomic-size Fraunhofer-type diffraction for single electron capture in He 2+ +He collision. *Journal of Physics: Conference Series*, 388(8):082053, 2012.

[44] A.Chatak. *Optics.* Tata McGraw-Hill Education, 2009.

[45] F.A.Jenkins and H.E.White. *Fundamentals of Optics.* McGraw-Hill, 4th edition, 1976.

[46] D. G. Stearns, R. S. Rosen, and S. P. Vernon. Multilayer mirror technology for soft-x-ray projection lithography. *Applied Optics*, 32(34):6952, 1993.

[47] B. R. Benware, A. Ozols, J. J. Rocca, I. A. Artioukov, V. V. Kondratenko, and A. V. Vinogradov. Focusing of a tabletop soft-x-ray laser beam and laser ablation. *Optic Letters*, 24(23):1714, 1999.

[48] D. L. Windt. IMD - Software for modeling the optical properties of multilayer films. *Comput. Phys.*, 12(4):360, 1998.

[49] R. Alnaimi, H. Wang, Z. Zhang, X. Yang, and M. Wen. Design calculations and characterization of C/Cr multilayer mirrors in the 6 nm BEUV. *Optik*, 127(2):588, 2016.

[50] A. Prakash and K. Struik. Roughness measurement of highly polished, mirror-finished surfaces. *Precision Engineering*, 3(4):215, 1981.

[51] M. Grisham, et al. Damage to extreme-ultraviolet Sc/Si multilayer mirrors exposed to intense 46.9-nm laser pulses. *Optics letters*, 29(6):620, 2004.

[52] S. A. Yulin, F. Schaefers, T. Feigl, and N. Kaiser. Enhanced reflectivity and stability of Sc/Si multilayers. *Proc. SPIE 5193, Advances in Mirror Technology for X-Ray, EUV Lithography, Laser, and Other Applications*, 155, 2004.

[53] A. V. Baez. Fresnel Zone Plate for Optical Image Formation Using Extreme Ultraviolet and Soft X Radiation. *Journal of the Optical Society of America*, 51(4):405, 1961.

[54] V. Aslanyan, I. Kuznetsov, H. Bravo, M. R. Woolston, A. K. Rossall, C. S. Menoni, J. J. Rocca, and G. J. Tallents. Ablation and transmission of thin solid targets irradiated by intense extreme ultraviolet laser radiation. *APL Photonics*, 1(6):066101, 2016.

[55] A. K. Rossall, V. Aslanyan, G. J. Tallents, I. Kuznetsov, J. J. Rocca, and C. S. Menoni. Ablation of submicrometer holes using an extreme-ultraviolet laser. *Physical Review Applied*, 3(6):1, 2015.

[56] I. A. Artyukov, B. R. Benware, A. V. Vinogradov, Y. S. Kas'yanov, V. V. Kondratenko, C. Macchietto, A. Ozols, J. J. Rocca, and J. Chilla. Focusing the beam of a compact, repetitively pulsed x-ray laser to study the interaction of radiaiton with metallic targets and x-ray reflectrometry. *Quantum Electronics*, 30(4):328 , 2000.

[57] A. Drechsler, M. Lieb, C. Debus, A. Meixner, and G. Tarrach. Confocal microscopy with a high numerical aperture parabolic mirror. *Optics Express*, 9(12):637, 2001.

[58] K. H. Gil, M. H. Jung, H. Choi, J. Lim, and J. Huang. Analysis and design of a new Kirkpatrick mirror system for microbeams. *Proceedings of IPAC2014*, pages 2081–2083, 2014.

[59] B. Khaykovich, M. V. Gubarev, Y. Bagdasarova, B. D. Ramsey, and D. E. Moncton. From x-ray telescopes to neutron scattering: Using axisymmetric mirrors to focus a neutron beam. *Nuclear Instruments and Methods in Physics Research, Section A: Accelerators, Spectrometers, Detectors and Associated Equipment*, 631(1):98, 2011.

[60] M. Riedl. *Optical Design Fundamentals for Infrared Systems.* SPIE Press, 2nd edition, 2001.

[61] Edmund Optics. Introduction to reflective optics, 2016.

[62] V. Aslanyan. Control electronics for an extreme ultraviolet capillary discharge laser. *EPSRC CDT Collaboratory project report*, 2014.

[63] I. a. Artyukov. Schwarzschild objective and similar two-mirror systems. *Short-Wavelength Imaging and Spectroscopy Sources, Proc. of SPIE*, 8678(2):86780A, 2012.

[64] G. J. Pert. Two-dimensional hydrodynamic models of laser-produced plasmas. 41(1989):263, 2018.

[65] A. K. Rossall, V. Aslanyan, S. Wilson, and G. J. Tallents. Generation of strongly coupled plasma using Argon-based capillary discharge lasers. *SPIE Optical Engineering + Applications*, 9589, 2015.

[66] A. K. Rossall and G. J. Tallents. Generation of warm dense matter using an argon based capillary discharge laser. *High Energy Density Physics*, 15:67, 2015.

[67] M. Cornille, J. Dubau, and S. Jacquemot. Radiative and Collisional Atomic Data for Neon-like Ions. *Atomic data and Nuclear Data tables*, 58:1, 1991.

[68] J. J. Rocca, D. P. Clark, J. L. Chilla, and V. N. Shlyaptsev. Energy Extraction and Achievement of the Saturation Limit in a Discharge-Pumped Table-Top Soft X-Ray Amplifier. *Physical Review Letters*, 77(8):1476, 1996.

[69] A. Siegman. *Lasers.* University Science Books, Mill Valley, CA, 1986.

[70] J. J. Rocca. Table-top soft x-ray lasers. *Review of Scientific Instruments*, 70(10), 1999.

[71] J. Rocca, F. Tomasel, C. Moreno, V. Shlyaptsev, M. Marconi, B. Benware, J. Gonzalez, J. Chilla, and C. Macchietto. Progress in the development of Table-Top Discharge-Pumped Soft X-Ray Lasers. *J. Phys IV France*, 7, 1997.

[72] B. Burke and F. Graham-Smith. *Introduction to radio Astronomy.* Cambridge University Press, 1997.

[73] H. Hutchinson, I. *Principles of Plasama Diagnostics.* Cambridge University Press, New York, 2nd edition, 2002.

[74] F. Trintchouk, M. Yamada, H. Ji, R. M. Kulsrud, and T. A. Carter. Measurement of the transverse Spitzer resistivity during collisional magnetic reconnection. *Physics of Plasmas*, 10(1):319, 2003.

[75] J. J. Rocca, M. C. Marconi, and G. Giudice. Discharge-pumped soft-x-ray laser in neon-like argon*. 2(6):2547, 1995.

[76] A. MacPhee. *Development of CCD detectors for study and applications of XUV lasers.* Ph.D. thesis, Queens University Belfast, 1996.

[77] Andor Technology. iKon-M / L SO Series.

[78] P. Chabert and N. Braithwaite. *Physics of Radio-Frequency Plasmas.* Cambridge University Press, Cambridge, 2011.

[79] M. A. Lieberman and A. J. Lichtenberg. *Principles of Plasma Discharges and Materials Processing: Second Edition.* 1994.

[80] V. A. Godyak, R. B. Piejak, and B. M. Alexandrovich. *Effective electron collision frequency and electrical conductivity of radio frequency plasmas*, volume 85. 1999.

[81] M. Bandyopadhyay, D. Sudhir, and A. Chakraborty. Can we estimate plasma density in ICP driver through electrical parameters in RF circuit? *Nuclear Fusion*, 55(3):033017, 2015.

[82] W. A. Davis and K. Agarwal. *Radio frequency circuit design.* Wiley, 162nd edition, 2003.

[83] S. Goldberg and J. Rothstein. Hydrogen Thyratrons. *Advances in Electronics and Electron physics*, 14:207 , 1961.

[84] D. K. Gupta and P. I. John. Design and construction of double-Blumlein HV pulse power supply. *Sadhana*, 26(5):475, 2001.

[85] T. Page, S. Wilson, J. Branson, E. Wagenaars, and G. Tallents. Plasma temperature measurements using black-body radiation from spectral lines emitted by a capillary discharge. *Journal of Quantitative Spectroscopy and Radiative Transfer*, 220:1, 2018.

[86] D. Grant and J. Gowar. *Power MOSFETS: Theory and applications.* Wiley, 1989.

[87] Midel. MIDEL 7131 Synthetic Ester Transformer Fluid Specifications. 44(June):1, 2013.

[88] Du Point. General Specifications Polyimide Film, 2018.

[89] P. Easton and P. West. *Atomic Force Microscopy.* Oxford University Press, 2010.

[90] E. G. Gamaly, A. V. Rode, B. Luther-Davies, and V. T. Tikhonchuk. Ablation of solids by femtosecond lasers: Ablation mechanism and ablation thresholds for metals and dielectrics. *Physics of Plasmas*, 9(3):949, 2002.

[91] H. Chung, M. H. Chen, W. L. Morgan, Y. Ralchenko, and R. W. Lee. FLYCHK : Generalized population kinetics and spectral model for rapid spectroscopic analysis for all elements. 1:3, 2005.

[92] G. J. Tallents, D. S. Whittaker, L. A. Wilson, and E. Wagenaars. Heating of high energy density plasmas using EUV and x-ray lasers. *Proc.SPIE*, 8140:8140 , 2011.